AN INTERFEROMETRIC STUDY OF MOLECULAR EMISSION AROUND NGC 7538 AT MILLIMETER WAVELENGTHS

BY

PREETHI PRATAP

B.Sc., Gujarat University, 1982
M.Sc., Indian Institute of Technology, 1983
M.S., University of Illinois, 1985

THESIS

Submitted in partial fulfillment of the requirements
for the degree of Doctor of Philosophy in Astronomy
in the Graduate College of the
University of Illinois at Urbana-Champaign, 1990

Urbana, Illinois

UNIVERSITY OF ILLINOIS AT URBANA-CHAMPAIGN

THE GRADUATE COLLEGE

APRIL 1990

WE HEREBY RECOMMEND THAT THE THESIS BY

PREETHI PRATAP

ENTITLED AN INTERFEROMETRIC STUDY OF MOLECULAR EMISSION AROUND NGC 7538 AT MILLIMETER WAVELENGTHS

BE ACCEPTED IN PARTIAL FULFILLMENT OF THE REQUIREMENTS FOR THE DEGREE OF DOCTOR OF PHILOSOPHY

Lewis E. Snyder
Director of Thesis Research

Ronald F. Webbink
Head of Department

Committee on Final Examination†

Lewis E. Snyder
Chairman

R.M. Crutcher

Helene R. Dickel

James B. Kaler

James M. Lusig

†Required for doctor's degree but not for master's.

O-517

UNIVERSITY OF ILLINOIS AT URBANA-CHAMPAIGN

GRADUATE COLLEGE DEPARTMENTAL FORMAT APPROVAL

THIS IS TO CERTIFY THAT THE FORMAT AND QUALITY OF PRESENTATION OF THE THESIS SUBMITTED BY Preethi Pratap AS ONE OF THE REQUIREMENTS FOR THE DEGREE OF Doctor of Philosophy IS ACCEPTABLE TO THE Department of Astronomy.

Full Name of Department, Division or Unit

24 April 1990
Date of Approval

Ronald F. Wilkinson
Departmental Representative

DEDICATION

To my parents - with all my love

ACKNOWLEDGMENTS

The time has come to acknowledge the help and support of all the people without whom this thesis would never have been completed. First, I would like to thank my advisor, Lew Snyder, who taught me many things and supported and encouraged me throughout my graduate career. I would also like to thank Dick Crutcher, Lanie Dickel and Jim Kaler for their helpful comments on this thesis. The astronomers at the Radio Astronomy Laboratory at Berkeley helped me unravel the intricacies of millimeter-wave interferometry.

I would like to acknowledge the support of a research assistantship from the Laboratory for Astronomical Imaging with funds provided for by the Berkeley-Illinois-Maryland-Array project by the University of Illinois. I would also like to acknowledge the help of the staff at the Hat Creek Observatory for their help and patience during my observing stints.

I am deeply indebted to my parents, Ramavarma Pratap and Ammini Pratap, for a lifetime of love, encouragement and for their undying belief in my ability to achieve my dreams. I am grateful for the friendship and support I have received from Susan John, which helped me survive the good times and the bad. I would like to thank Mark Schenewerk who introduced me to the wonders of Radio Astronomy, and Dean, Doc, Mike and Rick who introduced me to the wonders of American culture! And as always - "Thanks are due to the Basement Crew.

TABLE OF CONTENTS

I. THEORETICAL BACKGROUND

§1.1 Introduction

Maser action in the interstellar medium is associated with early and late stages of star formation. The strongest masers are OH, H_2O, and SiO. OH and H_2O are masers that have been found in regions of active star formation as well as in circumstellar shells around evolved stars. SiO was discovered in maser emission by Snyder and Buhl (1974) toward an active star forming region in the Orion nebula but it is typically associated with evolved stars. Table 1 lists the molecular species and their transitions which have been observed in maser emission.

Interstellar masers provide a potential tool for probing conditions around regions of star formation. Most masers require gas densities that are in the range of 10^5 - 10^{11} cm^{-3}. They also require a highly luminous source to provide the energy for population inversion. For masers around star forming regions, a newly formed O or B star could supply the pump energy. However, to use any of these masers as probes of the physical conditions, one must first understand the pumping mechanisms that provide the degree of population inversion that is seen. There are several maser models that are detailed enough to predict the properties of strong masers. Some of these have been successfully verified by observations. In the case of the weaker

Table 1.1

Observed Maser Transitions in Circumstellar Shells and Star Forming Regions

Molecule	Transition	Frequency (MHz)	Reference
OH	$^2\Pi_{3/2}$, J=3/2, F=1-2	1612.231	1
	$^2\Pi_{3/2}$, J=3/2, F=1-1	1665.402	1,2,3,4
	$^2\Pi_{3/2}$, J=3/2, F=2-2	1667.359	1,3
	$^2\Pi_{3/2}$, J=3/2, F=2-1	1720.530	1,6
	$^2\Pi_{1/2}$, J=1/2, F=0-1	4660.42	1
	$^2\Pi_{1/2}$, J=1/2, F=1-0	4765.562	1,7
	$^2\Pi_{3/2}$, J=5/2, F=2-2	6030.747	1
	$^2\Pi_{3/2}$, J=5/2, F=3-3	6035.092	1,8
	$^2\Pi_{3/2}$, J=7/2, F=4-4	13441.417	1
H_2O	6_{16} - 5_{23}	22235.1	9
SiO	v=2, J-1-0	42820.54	1
	v=1, J-1-0	43122.03	1
	v=1, J-2-1	86243.35	10
	v=1, J-3-2	129363.26	1
CH_3OH	2_0 - 3_{-1} E	12178.593	11
	2_1 - 3_0 E	19967.30	12
	9_2 - 10_1 A^+	23121.01	13
	3_2 - 3_1 E	24928.70	14
	4_2 - 4_1 E	24933.468	14
	2_2 - 2_1 E	24934.382	14
	5_2 - 5_1 E	24959.080	14
	6_2 - 6_1 E	25018.123	14
	7_2 - 7_1 E	25124.87	15
	9_2 - 9_1 E	25541.43	14
	4_{-1} - 3_0 E	36169.24	16
	7_0 - 6_1 A^+	44069.49	16
	5_{-1} - 4_0 E	84521.21	17
H_2CO	1_{10} - 1_{11}	4829.664	18
CH	$^2\Pi_{3/2}$, J=1/2	3349.185	19
HC_5N	J=1-0	2664.87	20
NH_3	9(6) - 9(6)	18499.4	21
	6(3) - 6(3)	19757.575	21
	3(3) - 3(3)	23870.1296	22,23
$^{15}NH_3$	3(3) - 3(3)	22979.4	24

(1) Reid and Moran (1981); (2) Reid et al. (1980);
(3) Mader et al. (1978); (4) Haschick et al. (1981);
(5) Harvey et al. (1974); (6) Lo et al. (1975);
(7) Palmer et al. (1984); (8) Moran et al. (1978);
(9) Genzel et al. (1979); (10) Snyder and Buhl (1974);
(11) Batrla et al. (1987); (12) Wilson et al. (1985);
(13) Wilson et al. (1984); (14) Menten et al. (1986);
(15) Matsakis et al. (1980); (16) Morimoto et al. (1985);
(17) Batrla and Menten (1988); (18) Downes and Wilson (1974);
(19) Turner and Zuckerman (1974); (20) Broten et al. (1976);
(21) Madden et al. (1986); (22) Wilson et al. (1982);
(23) Guilloteau et al. (1983); (24) Mauersberger et al. (1986).

masers, the theory is less advanced.

This chapter will attempt to outline the models that have been proposed to explain the maser excitation in star forming regions and the various parameters that can be calculated from observations and used as inputs to the maser models. The two strongest masers, OH and H_2O, will be discussed first, but the ultimate motivation for this project has been to study the conditions necessary for the excitation of the H_2CO maser. The H_2CO maser excitation is being studied with reference to the star forming region NGC 7538 IRS 1, which is the only galactic source besides Sgr B2 (Whiteoak and Gardner, 1983; Gardner et al. 1986) where formaldehyde maser emission has been observed. The only model that has been proposed to explain the H_2CO emission in NGC 7538 (Boland and de Jong, 1981) imposes stringent conditions on the nature of the source. The goal here is to examine these conditions and their feasibilty. Formaldehyde maser emission has also been observed toward the OH megamaser galaxy IC 4553 and possibly toward NGC 3079 (Baan et al. 1986). The maser emission toward IC 4553 is about 7 orders of magnitude more powerful than are the galactic masers. An understanding of the galactic H_2CO masers should provide an understanding of the mechanisms causing the H_2CO maser emission in the extragalactic source.

A basic premise of this thesis is to use the techniques of millimeter interferometry to probe the high density regions around newly formed stars. The technique is invaluable since the spatial resolution of an interferometer allows the study of small scale

density enhancements in the molecular cloud that could provide the conditions for maser excitation. In addition to the detailed density structure, the millimeter continuum observations provide a tool for modeling the H II region and for calculating parameters such as electron density, electron temperature, and emission measure, which are useful in determining the excitation mechanism for the maser emission.

§1.2 Maser Theory

In order to understand the physical conditions in masers it is necessary to model the molecular excitation and radiative transfer. Radiative transfer in masers can be complicated since the stimulated emission rates could be greater than the rates of population inversion. This causes the maser to be saturated since the photons produced by the stimulated emission affect the level population and cause the inversion to decrease. The basic questions that maser theory addresses are those related to the source of the radiation that is amplified, the processes that produce population inversion, and the degree of saturation in astronomical masers. The theory should also allow for the derivation of the observable parameters like apparent brightness, size, line width, and polarization from the physical parameters of the source. Once a good model is available, the masers can then be used as a probe of the conditions that exist in the vicinity of the maser.

The first step in understanding maser emission is to understand radiative transfer in masing sources. This discussion follows the approach taken by Reid and Moran (1981).

The standard radiative transfer equation,

$$\frac{dI}{dl} = - \kappa I + \epsilon, \qquad (1.1)$$

describes the change in intensity, I, at the line center with the distance, l, in the masing region. Here κ is the volume absorption coefficient given by

$$\kappa = \frac{h\nu}{4\pi\Delta\nu} (n_1 - n_2) B, \qquad (1.2)$$

and ϵ is the volume emission coefficient given by

$$\epsilon = \frac{h\nu}{4\pi\Delta\nu} n_2 A, \qquad (1.3)$$

where n_1 and n_2 are the population densities of the lower and upper maser levels, A and B are the Einstein coefficients for spontaneous emission and stimulated emission respectively, ν is the frequency of the line center, and $\Delta\nu$ is the Doppler line width.

In order to calculate the population inversion, one can start from the steady state rate equations. For a two level system with a lower

level population n_1 and an upper level population n_2, the rate equations are

$$\frac{dn_1}{dt} = P_1 - \Gamma_1 n_1 + An_1 + BJ(n_2 - n_1) + C[n_2 - n_1 \exp(-h\nu/kT)] \tag{1.4}$$

and

$$\frac{dn_2}{dt} = P_2 - \Gamma_2 n_2 - An_2 - BJ(n_2 - n_1) - C[n_2 - n_1 \exp(-h\nu/kT)].$$

Here P_i is the pump rate per sublevel. The ratio g_1/g_2 (the ratio of statistical weights) has been assumed to be unity, which results in an error of a few percent. Γ_1 and Γ_2 are the rates at which population can be redistributed throughout the pump cycle. Here, $\Gamma_1 = \Gamma_2 = \Gamma$. Neglecting the spontaneous emission and collision terms, one gets (in steady state)

$$\Delta n = n_2 - n_1 = (n_2 + n_1) \frac{\Delta R}{R} \frac{\Gamma}{\Gamma + 2BJ}, \tag{1.5}$$

where $J \sim I\,\Omega/4\pi$ (Ω = beam solid angle); $\Delta R = P_1 + P_2$; $R = P_2 - P_1$. The solution of the radiative transfer equation for the one-dimensional case is given by

$$I(1) = I(0)e^{-\kappa l} + \frac{\epsilon}{\kappa}(1 - e^{-\kappa l}). \tag{1.6}$$

Here κ and ϵ have been assumed to be constant; κ can be rewritten as

$$\kappa = \frac{\kappa_0}{1 + 2BI(\Omega/4\pi)/\Gamma}, \tag{1.7}$$

where $\kappa_0 = \Delta n_0 [Bh\nu/4\pi\Delta\nu]$. Here Δn_0 is the unsaturated population difference.

So κ is constant when $\Gamma >> 2BI(\Omega/4\pi)$. For a maser, $n_2 > n_1$ and $\kappa < 0$. Since the optical depth (κl) is negative, exponential amplification occurs. Converting the intensity into a brightness temperature, T_B, of an equivalent blackbody, and using the Rayleigh-Jeans approximation, one can rewrite equation (1.6) as

$$T_B(l) = [T_B(0) - T_x]e^{-\kappa l} + T_x, \tag{1.8}$$

where the excitation temperature, T_x, is defined by

$$n_2/n_1 = \exp(-h\nu/kT_x). \tag{1.9}$$

Under the condition of population inversion, $T_x < 0$. The magnitudes of $T_B(0)$ and T_x dictate the relative importance of background emission and spontaneous emission from the maser itself as sources of input signals to the maser. Equation (1.5) shows that the population inversion is reduced by stimulated emission when $2BI(\Omega/4\pi)$ is greater than Γ. This implies that the maser is saturated. The brightness temperature, where the maser is saturated, is given by (using the

Rayleigh-Jeans approximation)

$$T_s = \frac{h\nu}{2k} \frac{\Gamma}{A} \frac{4\pi}{\Omega}, \qquad (1.10)$$

where $A = (2h\nu^3 B/c^2)$. In the case of saturated growth the population inversion decreases inversely proportional to the stimulated emission rate.

§1.3 H II Region Spectra

In order to arrive at reasonable pump models for masers, one has to know the relevant parameters associated with the pump source which provide the conditions necessary for population inversion. So, before studying specific maser models, one has to be able to determine observationally the conditions that form the input to these models. For collisional pumps one of the inputs is the H_2 density, which involves a knowledge of collision cross sections. The H_2 density can be probed by using several molecules for which these cross sections are known. This problem will be studied in the next section.

Radiative pumps are, in general, more complicated since one has to know the nature of the source providing the photons which involves a knowledge of the source at various wavelengths and the parameters that provide the observed flux densities. For masers associated with star forming regions, the pump source is either the newly formed star or

the H II region. The spectra of the H II region can be obtained from continuum observations at several wavelengths. The observed infrared flux densities can be fit by assuming models for the dust distribution around the H II region. The radio spectrum can be fit by assuming a certain geometry for the H II region and by calculating the resulting flux densities. The radiation process is assumed to be thermal bremsstrahlung. The model for the H II region has certain free parameters which can be chosen to fit the observed flux densities.

Such spectra for compact H II regions have been calculated by Olnon (1975). The models assumed for the source have circular symmetry along the line of sight, with ionized hydrogen as the only constituent of the H II region. The distance to the object is D, the depth along the line of sight (measured from the center of the object) is z, and the radius perpendicular to the line of sight is p. In the Rayleigh-Jeans regime, the flux S_ν, the continuum optical depth τ_c, and the emission measure E can be written as

$$S_\nu = \frac{4\pi k T_e \nu^2}{c^2 D^2} \int_0^\infty p \, [1 - \exp(-\tau_c(\nu,p)] \, dp, \qquad (1.11)$$

$$\tau_c(\nu,p) = f(\nu,T_e) \, E(p), \qquad (1.12)$$

and

$$E(p) = 2 \int_0^\infty n_e^2(r) \, dz, \qquad r^2 = p^2 + z^2. \qquad (1.13)$$

The function $f(\nu,T_e)$ depends on the details of the bremsstrahlung process and can be written as

$$f(\nu,T_e) = 8.235 \times 10^{-2} \ (T_e/\ K)^{-1.35} \ (\nu/GHz)^{-2.1} \ cm^6 \ pc^{-1}. \tag{1.14}$$

For a spherical H II region with $n_e = n_0$ = constant inside a radius R, and $n_e = 0$ outside the sphere,

$$\begin{aligned} E(p) &= 2n_0^2 \ (R^2 - p^2)^{1/2} && p < R \\ &= 0 && p \geq R \end{aligned} \tag{1.15}$$

and

$$S_\nu = \frac{2\pi k T_e R^2 \nu^2}{c^2 D^2} \left[1 - \frac{2}{\tau^2} \ \{1 - (\tau+1)e^{-\tau}\}\right], \tag{1.16}$$

where $\tau = 2n_0^2 Rf$.

The critical turnover frequency ν_0 can be defined by the condition $\tau(\nu_0) = 1$. Hence,

$$\begin{aligned} S_\nu &\simeq \frac{8\pi k T_e R^2 \nu^2}{3c^2 D^2} \ f n_0^2 && \nu \gg \nu_0 \\ S_\nu &\simeq \frac{2\pi k T_e R^2 \nu^2}{c^2 D^2} && \nu \ll \nu_0 . \end{aligned} \tag{1.17}$$

The flux calculated from this model depends on four free parameters, namely, n_0, T_e, R and D. For a compact H II region,

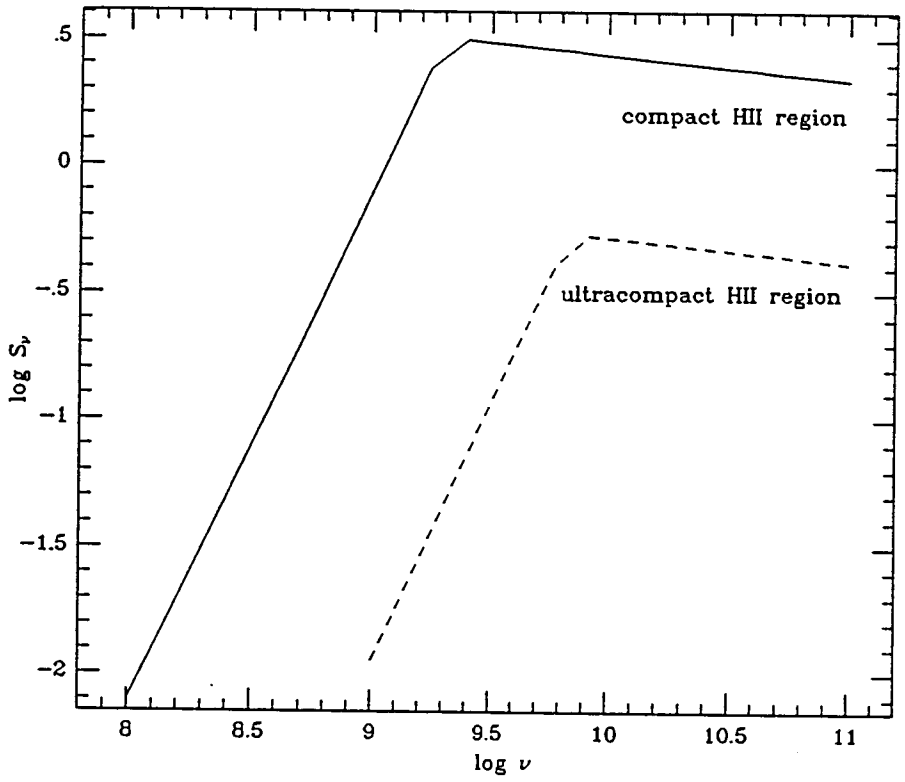

Figure 1.1 - Log ν - log S_ν plots for model H II regions. The solid line is the spectrum for a compact H II region with $T_e = 10^4$ K, $n_0 = 10^4$ cm^{-3}, and R = 0.1 pc. The dashed line is the spectrum for an ultracompact H II region with $T_e = 2 \times 10^4$ K, $n_e = 2 \times 10^5$ cm^{-3}, and R = 0.0085 pc.

typically, 10^4 cm^{-3} > n_0 > 10^3 cm^{-3}, and 0.1 pc < R < 1 pc. An ultracompact H II region has $n_0 > 10^4$ cm^{-3} and R < 0.1 pc. Figure 1.1 shows two H II region spectra calculated from the above equations. The solid line indicates the spectrum for a compact H II region with $T_e = 10^4$ K, $n_0 = 10^4$ cm^{-3} and R = 0.1pc. The dashed line shows the spectrum for an ultracompact H II region. The values used here were found for NGC 7538 IRS 1 by Henkel et al. (1984). They are $n_0 = 2 \times 10^5$ cm^{-3}, $T_e = 2 \times 10^4$ K and $R = 8.5 \times 10^{-3}$ pc. The source distance, D, has been taken to be 3.5 kpc for both the models. This is the distance to NGC 7538 IRS 1 found by Israel et al. (1973). The spectrum at the lower frequencies defines the region where the H II region is optically thick ($S_\nu \propto \nu^2$) while the spectrum at the higher frequencies defines the optically thin region ($S_\nu \propto \nu^{-0.1}$). Thus, in models where the masers are radiatively pumped, one can determine the wavelength regimes that provide the pump photons by examining the optically thin regions of the spectrum.

§1.4 Collisional Cross Sections

Collisional pumps require a knowledge of the collisional cross sections of the various molecules colliding with H_2. This knowledge is also necessary in interpreting microwave spectra in molecular clouds. In order to use the molecular emission as an effective density probe, one needs to know the H_2 densities at which the particular molecule thermalizes. If the emission is optically thin, one can easily arrive

at the required density by neglecting stimulated emission and absorption. This results in an equilibrium equation of $n_{H_2} \langle \sigma v \rangle = A_{ij}$ for a transition from level i to level j. Here $\langle \sigma v \rangle$ is the collisional rate coefficient which is a function of the kinetic temperature of the cloud. A_{ij} is the Einstein coefficient for spontaneous emission, which is given by (Townes and Schawlow, 1956) as

$$A_{J+1,J} = \frac{64\pi^4}{3hc^3} \nu^3 \ |\mu_{J+1,J}|^2, \qquad (1.18)$$

where $\mu_{J+1,J}$ is the dipole moment matrix element; for a linear molecule it is given by $\mu_{J+1,J} = (J+1)\mu^2/(2J+3)$ (Townes and Schawlow, 1956).

There are very few molecules for which detailed calculations of these collisional cross sections have been made. Most of the rate coefficients have been the result of quantum mechanical scattering calculations. The basic method has been described in detail in a paper by Green and Thaddeus (1976). The results have been applied to calculate the constants for the rotational excitation of CO with He, H, and H_2. The same techniques have been applied to calculate the rate coefficients for collisions of HCN (Green and Thaddeus, 1974), HD (Green, 1974), N_2H^+ (Green, 1975), HCl (Green and Monchick, 1975), and H_2CO (Garrison et al. 1975). The calculations also predict collision-induced pressure broadening constants, which have been compared with experimental data for CO, HCN, HD and HCl. The agreement was found to

be quite good.

In the case of HCN, the calculations have only been done for the HCN-He collisions, since they are much simpler to treat theoretically. For CO the excitation by collision with H_2 is quite similar to excitation by collision with He. At low temperatures of the interstellar clouds, H_2 molecules are expected to be in their lowest J=0 rotational level and they can be treated as spherical particles. The temperatures required for an equal population of the J=1 level is about 120 K and that for the J=2 level is about 350 K. In fact the H_2 (J=0) state is quite similar to He except for the smaller reduced mass, so the rates for excitation by H_2 are expected to be about 50 percent larger than the corresponding rates for He. This argument may be less true for HCN due to long range HCN-H_2 dipole-quadrupole interactions, but the difference between the He and H_2 projectiles is expected to be no larger than the uncertainties produced by other approximations.

Green and Chapman (1978) have used the quantum mechanical scattering technique to include more rotational levels in the excitation scheme. To overcome the computational problem, they have proposed several approximate scattering methods and have tested these against the accurate quantum results available for CO, CS, OCS and HC_3N. The paper presents calculations of the CO-He rate coefficients which include more levels than previously considered. It also presents calculations of the coefficients for the CS-H_2(J=0), the OCS-H_2, and the HC_3N-He collisions.

In the case of molecular ions, a study was first made by Green (1975) to calculate rate constants for the rotational excitation of N_2H^+ by collisions with He. At the low temperatures relevant for interstellar clouds, it was found that the rates are only slightly larger than those for similar neutral species. More recent calculations have been done (Monteiro 1984) to compare the rate coefficients of the three interstellar ions HCO^+, HCS^+, and N_2H^+. The calculations were also extended to study collisions between HCO^+ and H_2 (Monteiro 1985). The two calculations used different methods to evaluate the potential surfaces of the interacting systems. The rate coefficients for collisions with para-H_2 are found to be larger by 50 to 100 percent than those for collisions with He.

A knowledge of the rate coefficients enables one to calculate density regimes where a particular molecular transition would be a useful probe. Using the rate coefficients from Green and Thaddeus (1976) at a temperature of 20 K, the critical density for the J=1-0 transition of CO (μ = 0.112 debye, Spitzer 1978) is found to be ~ 2 x 10^3 cm^{-3}. In the interstellar medium the emission from this transition of CO is generally found to be optically thick. In such a situation, one can use the emission from the J=1-0 transition of ^{13}CO which is a probe of similar densities. For the J=1-0 transition of HCN (μ = 2.98 debye, Spitzer, 1978), the cross sections from Green and Thaddeus (1974) results in a thermalization density n_{H_2} ~ 2 x 10^6 cm^{-3}. The calculation takes into account the reduced mass of hydrogen since the cross sections were evaluated for the HCN-He collisions. For HCO^+ (μ =

3.91 debye, Botschwina, 1989), the cross sections from Monteiro (1985) result in a critical density of ~ 2 x 10^5 cm^{-3}. Thus the emission from the three molecules can be used to probe different density regimes.

The above discussion assumes that the emission is optically thin. The effect of large optical depths on H_2 densities probed by the molecular transitions can be studied by expanding the equation of radiative transfer (equation 1.6) to first order in τ. In equation 1.6, the optical depth, τ, is κl. For a simple 2-level system, the ratio ϵ/κ can be written as

$$\frac{\epsilon}{\kappa} = \frac{2\nu^2 kT_x}{c^2} \left[\frac{n_{H_2}\langle\sigma v\rangle/A_{21} + kT_B(0)/h\nu\ (1+h\nu/kT_x)\ T_x}{kT_x/h\nu + n_{H_2}\langle\sigma v\rangle/A_{21} + T_B(0)/T_x}\right], \tag{1.19}$$

(Spitzer 1978). The equation was obtained by starting from the detailed balance equation for a 2-level system and taking the Rayleigh-Jeans approximation. The geometrical dilution factor is assumed to be 1. Equation 1.6 can be rewritten as

$$I(1) = I(0) + \tau(\epsilon/\kappa - I(0)). \tag{1.20}$$

This equation just consists of the first order terms in τ. Taking the Rayleigh-Jeans approximation and substituting equation 1.19 for ϵ/κ, equation 1.20 can be rewritten as

$$T_B(1) - T_B(0) = \tau \left[\frac{(T_x - T_B(0))\ \{1 + (T_B(0)/T_x)\ (A_{21}/n_{H_2}\langle\sigma v\rangle)\}}{1+(kT_x/h\nu)(A_{21}/n_{H_2}\langle\sigma v\rangle)+(T_B(0)/T_x)(A_{21}/n_{H_2}\langle\sigma v\rangle)}\right]. \quad (1.21)$$

The ratio $A_{21}/\langle\sigma v\rangle$ can be written as the critical density, $n_{H_2}(c)$, which is the density at which the spontaneous radiative transition rates and the collisional rates are equal. Equation 1.21 can be rewritten as

$$T_B(1) - T_B(0) = \tau \left[\frac{(T_x - T_B(0))\ \{1 + (T_B(0)/T_x)\ (n_{H_2}(c)/n_{H_2})\}}{1+(n_{H_2}(c)/n_{H_2})(kT_x/h\nu)+(T_B(0)/T_x)(n_{H_2}(c)/n_{H_2}}\right]. \quad (1.22)$$

This equation can be used to determine the effect of large optical depths on the critical densities probed by the various molecular transitions. This will be examined in Chapter 4.

§1.5 Masers Around H II Regions

The next few sections will examine the models that have been proposed to explain maser excitation around H II regions, in particular the OH masers, the H_2O masers and the rare H_2CO maser. Perhaps because the H_2CO maser is not a strong maser, it has been observed in only two galactic sources, namely, Sgr B2 and NGC 7538. Observational results will be presented in later chapters that examine the specific conditions required by the model to excite this maser.

§1.5.1 OH masers

The main line OH masers (1665 MHz and 1667 MHz - see Figure 1.2) are among the strongest masers that have been found around H II regions. These maser spots always appear to be located at the surfaces of H II regions - a fact that has been confirmed by several interferometric observations (Dickel et al. 1982; Norris et al. 1982; Palmer et al. 1984). Various observations (Habing et al. 1974) have suggested that the maser sources are always associated with compact H II regions with dimensions $\leq 5 \times 10^{17}$ cm. The bright young stars (O and B type) ionize the surrounding medium. The energy released in this process heats the H II region to temperatures of about 10^4 K. Since the pressure in the ionized H II region is higher than that of the surrounding medium, the H II region expands with a velocity of the order of 10 km s^{-1}. It takes about 10^4 yr for the region to expand to dimensions of $\sim 10^{17}$ cm which means that the OH maser is short lived and appears in the early phase in the evolution of an H II region.

The description of the H II region development from Spitzer (1978) shows that the expansion leads to the formation of a shock front at the edge of the ionized material. By following the chemical development of the material behind the shock front, Elitzur and de Jong (1978) showed that there was an enhancement of OH abundance in the high density post-shock region. This was suggested to be the location of the OH masers. The shock slows down with the expansion of the H II region and the maser turns off. The OH masers are thus

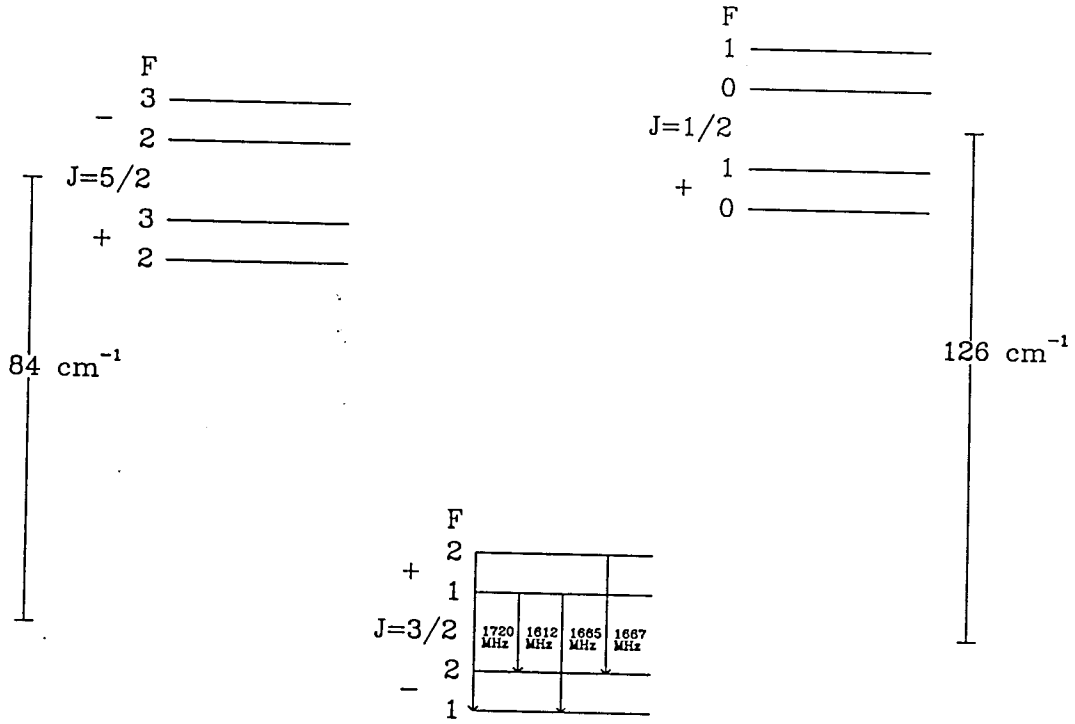

Rotation Levels of OH

Figure 1.2 - Energy level diagram of the three lowest rotation levels of OH. The maser transitions are shown with downward arrows. The maser frequencies are also indicated.

probing the high density shells around the H II region. The structure of these regions is quite complex since the H II region expands into a clumpy molecular cloud and results in an expansion which is not spherically symmetric. High resolution observations of the surrounding molecular cloud can be used along with observations of the masers to probe this interface between the H II region and the molecular cloud.

In order to use the OH masers as probes of the high density material surrounding H II regions, one needs a good understanding of the pump mechanisms and excitation conditions. OH masers around H II regions appear to be highly saturated. Studies of the W3(OH) region have shown that OH masers that are not projected against the H II region are as strong as the ones that are (Norris and Booth, 1981). The high power output from these masers implies a higher pump rate, which means that these masers are more efficient in utilizing the luminosity from the H II region (~ 10^5 $L_\odot$) to produce maser action.

Radiative pumps based on electronic or vibrational excitations can be dismissed since the number of UV and near IR photons produced by the H II regions is much smaller than the number of maser photons. Observations in the far IR (Thronson and Harper, 1979) show that the spectrum rises until ~ 100 μ, indicating a lower dust temperature (~ 30 - 50 K). The rising spectrum implies that radiative pumping, based on rotational excitation, is a possibility, since the number of photons at wavelengths between 30 - 120 μ is larger than the number of maser photons. Such low dust temperatures, however, can only be found in regions far away from the stellar source, since if the OH maser is

indeed located close to the H II region, the radiation there would heat the dust to much higher temperatures. The OH masers would then have to be located in the far IR emitting region which means that the geometrical dilution would reduce the number of photons available to pump the maser. Since this explanation depends on the source structure, one cannot readily dismiss the far-IR photons as a viable pump for the OH maser.

In the case of collisional pumps, it appears that the only pump which stands a chance of explaining the large maser flux in the OH/HII region involves inversion resulting from the direct population exchange between maser levels. Such an inversion would not be possible in a two level system when the colliding particles obey the Maxwell-Boltzmann distribution, since the levels would thermalize when collisions dominate the downward transitions, which is when the densities are high. Non-isotropic velocity distributions, like a particle stream, could provide a deviation from thermal equilibrium, which could invert the level population. Electron and ion streams have been considered in several models (Johnston 1967; Elitzur 1979) but the lack of precise collision cross sections makes it difficult to come to any conclusions about the nature of these pumps. It seems that the best way is to search for observational evidence for the nature of the pump mechanism. A correlation between the OH output and the far-IR flux would argue in favor of radiative pumps, while a correlation between the maser output and the square of the density would provide a strong argument in favor of collisional pumps.

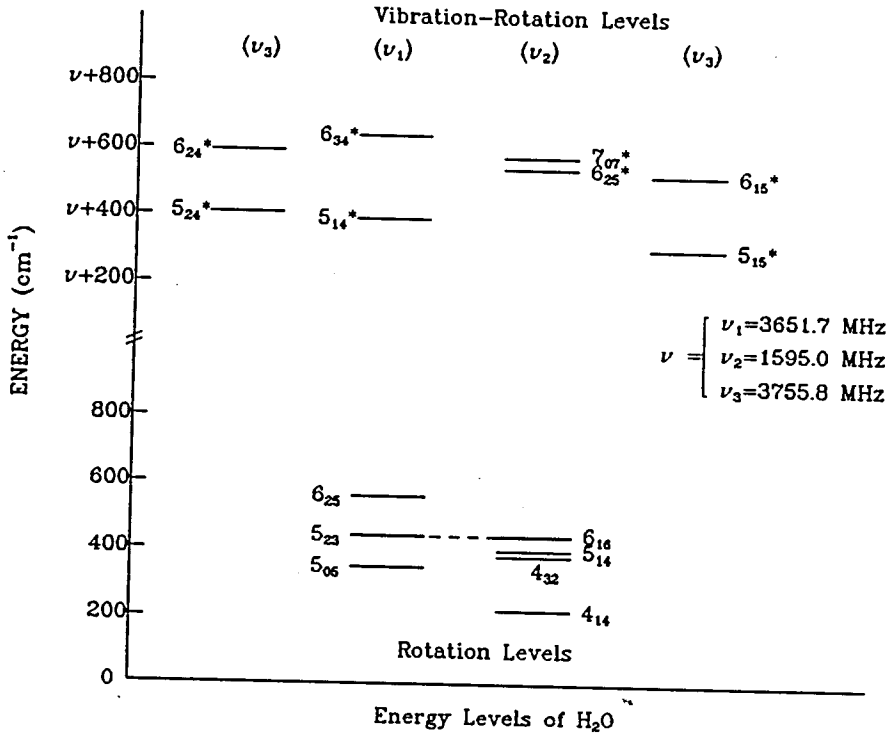

Figure 1.3 - Energy level diagram of some rotational levels and some vibration-rotation levels of H_2O. The energies for the vibrational levels are shown with offsets, ν. ν is either ν_1, ν_2, or ν_3 (the frequency equivalents are shown in the figure). ν_3 is associated with first and fourth sets of vibration-rotation levels, ν_1 with the second set of levels, and ν_2 with the third set of levels. The asterisks indicate that the levels are vibration levels. The maser transition, 6_{16}-5_{23}, is indicated by the dashed line.

§1.5.2 H_2O masers

Radio emission from the H_2O molecule provides the most intense maser emission of any source. Brightness temperatures have been seen in excess of 10^{14} K (Burke et al. 1970; Johnston et al. 1971). In the case of H II regions, H_2O masers do not seem to be clearly associated with the newly-formed star.

Very few detailed calculations have been performed on the excitation mechanism of the H_2O molecule, mainly because of the complexity of the spectrum (see Figure 1.3). The H_2O molecule is an asymmetric rotor and the levels are labeled $J_{K_{-1}K_1}$, where J is the total angular momentum, and K_{-1} and K_1 are its projections on the two molecular axes (Townes and Schawlow 1956). The strong maser transition is the 6_{16} - 5_{23} transition (marked by the dashed line in Figure 1.3). An inversion appears to be easily achieved irrespective of the excitation mechanism of the H_2O molecule. The H_2O masers in star forming regions are the least understood maser sources. The emission from the maser is so intense that it is not clear what type of mechanism could be producing them. The pump mechanisms proposed so far (de Jong 1973) lead to the production of IR fluxes that are much greater than observed values (Forster, Welch and Wright 1977).

Collisional pump models have also not been able to provide sufficient enhancement to provide brightness temperatures of ~ 10^{15} K. In these cases, if the source is assumed to be in approximate thermal equilibrium, the excitation rates for collisions and radiations would

be expected to be roughly similar. So the pump cycle must involve a situation that is inherently different from thermodynamic equilibrium. A possible model proposed by Goldreich and Kwan (1974) involves the presence of dust in the source at a temperature different from that of the gas. If the dust determined the optical depth of the entire system, it could be shielding some of the pump photons, and the thermodynamic constraints could be eased. This situation would be time variable, since in steady state the dust and gas temperatures would reach equilibrium. Tarter and Welch (1979) suggested surface collisions between a small dense cloud and another cloud or the H II region, which could provide local heating for a short time and thus give the conditions for the pump. Detailed calculations have yet to be presented. So it is clear that H_2O masers are among the least understood masers.

§1.5.3 Formaldehyde (H_2CO) masers

H_2CO masers have been observed only in two galactic sources, namely, Sgr B2 and NGC 7538 IRS 1 (Whiteoak and Gardner 1983, Downes and Wilson 1974, Rots et al. 1981). The only model to explain the observed 1_{10} - 1_{11} transition brightness temperature of 10^6 K in NGC 7538 was proposed by Boland and de Jong (1981). H_2CO has been observed in absorption against the 2.7 K cosmic background radiation (Palmer et al. 1969). This anomalous absorption was explained by Townes and Cheung (1969) by a collisional pump model, and later confirmed by numerical calculations of the H_2 - H_2CO cross sections by Garrison et

al. (1975). Since the conditions in the dark clouds are presumably not very different from those in the molecular cloud associated with NGC 7538 IRS 1, one cannot easily explain the H_2CO emission by collisional pumping. The model proposes that the H_2CO maser is pumped by the free-free continuum radiation of the H II region.

The model considers formaldehyde molecules in a molecular hydrogen cloud in the presence of a strong radio continuum field. The equations of radiative transfer are solved by assuming that the thermal velocities of the molecules are much smaller than the large scale velocities in the gas. The general expression for the free-free continuum optical depth can be written as

$$\tau_c(\nu) = 3.014 \times 10^{-2} \, (T_e/K)^{-1.5} \, (\nu/GHz)^{-2} \, \{\ln[4.955\times10^{-2}(\nu/GHz)^{-1}] + 1.5 \ln(T_e/K)\} \, (E/pc.cm^{-6}) \qquad (1.23)$$

(Oster 1961; Mezger and Henderson 1967).

Here E is the emission measure of the H II region which is defined as $\int_0^L n_e^2 dS$.

In this expression, the square of the electron temperature is integrated along the line of sight of length L. The value of the integral usually depends on the geometry assumed for the H II region (Olnon 1975).

In order to arrive at the expression used by Boland and de Jong for the free-free continuum optical depth, first convert $\tau_c(\nu)$ to

$\tau_c(\lambda)$:

$$\tau_c(\lambda) = 7.7233\times10^{-5}\ (T_e/K)^{-1.5}\ (\lambda/cm)^2\ \{\log[1.6662\times10^{-3}(\lambda/cm)] + 1.5\ \log(T_e/K)\}\ (E/pc.cm^{-6}). \tag{1.24}$$

The emission measure, E, can be written as a function of the turnover wavelength of the H II region, λ_0; λ_0 is defined as the wavelength at which $\tau_c(\lambda) = 1$. For an electron temperature $T_e = 10^4$ K,

$$\tau_c(\lambda) = 7.7233\times10^{-11}\ \lambda_0^2\ \{\log(1.6528\times10^{-3}\lambda_0) + 6\}\ (E/pc.cm^{-6}) = 1. \tag{1.25}$$

Solving this for E gives

$$E = \frac{1.2948\times10^{10}}{\lambda_0^2\ \{\log(1.6528\times10^{-3}) + \log\ \lambda_0 + 6\}}\ . \tag{1.26}$$

Neglecting the log λ_0 term,

$$E = \frac{4.0233\times10^{9}}{\lambda_0^2}\ , \tag{1.27}$$

or

$$\lambda_0 = 6.343\times10^{4}\ E^{-0.5}\ . \tag{1.28}$$

Thus,

$$\tau_c(\lambda) = (\lambda/\lambda_0)^2 \{1 + 0.311 \log(\lambda)\} , \qquad (1.29)$$

where λ and λ_0 are expressed in cm. This is the expression used by Boland and de Jong.

The equations of detailed balance in statistical equilibrium can be written as

$$\Sigma_j P_{jk}\, n_j = n_k\, \Sigma_j P_{kj} . \qquad (1.30)$$

The transition rates P_{ij} are defined by

$$\begin{aligned} P_{jk} &= A_{jk}[\beta_{jk}(1 + H_{jk}) + D_{jk}] \qquad (j>k) \\ &= A_{jk}[\beta_{jk}H_{jk} + D_{jk}]g_k/g_j + C_{jk} \qquad (j<k) . \end{aligned} \qquad (1.31)$$

Here, A_{jk} - spontaneous radiative transition probability,

C_{jk} - collision induced transition probabilty,

β_{jk} - escape probabilty (de Jong et al. 1975),

$\beta_{jk}H_{jk}$ - photon occupation numbers of the jk line of the blackbody background radiation field (Elitzur et al. 1976),

D_{jk} - photon occupation number of the jk line of the free free continuum field

$$= \frac{1 - \exp\{\tau_c(\lambda_{jk})\}}{\exp(hc/\lambda_{jk}T_e) - 1}\, W(r),$$

$W(r)$ - factor by which the radiation field gets diluted at a

distance r from the H II region

$$= 1/2 \int_{1/2(1-(R_{II}/r)^2)^{1/2}}^{1} \beta_{jk}(r)dr.$$

Here, R_{II} is the radius of the H II region and r is the distance at which the masing gas is situated. The escape probabilty, β_{jk}, is defined as the probability that a photon emitted in a transition from level j to level k, at a radial distance r from the center of the cloud, will escape. The expression for β_{jk} is

$$\beta_{jk}(r) = 1/2 \int_{-1}^{+1} \frac{1 - \exp\{-\tau_{jk}(r,\mu)\}}{\tau_{jk}(r,\mu)} d\mu. \qquad (1.32)$$

The expression in the integral can be simply calculated by considering a slab geometry. If the optical depth normal to the face of the slab is τ and if the radiation enters with an intensity I, then it emerges with an intensity $I\exp(-\tau)$. The probability for the radiation to escape from the slab is $\exp(-\tau)$. Since for radiation generated inside the source, the precise point of production is not known, one needs to perform an average over optical depths, which gives a mean escape probability

$$\beta = \langle\exp(-\tau)\rangle = (1/\tau) \int_0^{\tau} \exp(-\tau')\, d\tau' = [1-\exp(-\tau)]/\tau. \qquad (1.33)$$

One then takes into consideration that the radiation can enter the slab at any angle. This angle dependence can be included in the optical depth; $\tau_{jk}(r,\mu)$ is then the optical depth defined along a direction which makes an angle arccos(μ) with the radius vector. The escape probability is then this $\beta_{jk}(r,\mu)$ averaged over all angles, which results in equation 1.32 (de Jong et al. 1975). The optical depth is given by

$$\tau_{jk}(r,\mu) = \frac{hcr}{4\pi v} g_j B_{jk} (N_k - N_j) [1 - \mu^2 (1-\xi)]^{-1}. \quad (1.34)$$

This can be taken either as the optical depth of the entire cloud with a line width given by the full expansion velocity or as the optical depth of the radiatively connected region with a thermal linewidth. In this expression, $1 - \xi = 1 - (d\ln v/d\ln r) = 1 - (r/v)(dv/dr) = \alpha$ (in Boland and de Jong). N_k and N_j are the populations per sub level and can be written in terms of the level populations as $N_k = n_k/g_k$ where g_k is the statistical weight of the k level (= 2J+1). Expressing the Einstein B in terms of the Einstein A (A_{jk}), the optical depth can be rewritten as

$$\tau_{jk}(r,\mu) = \frac{\lambda_{jk}^3 A_{jk}}{8\pi} \frac{r}{v(r) [1 - \mu^2\alpha]} (n_k \frac{g_j}{g_k} - n_j), \quad (1.35)$$

where $\beta_{jk}H_{jk}$ and $D_{jk}(r)$ are the photon occupation numbers of the jk line of the blackbody field and the free-free continuum radiation field respectively. In order to define the photon occupation number, consider the radiation field as a gas of (massless) photons, each with energy $h\nu$ and momentum $h\nu/c$. The statistical weight of a given photon configuration is the number of cells in phase space (the $\underline{r}$ - $\underline{p}$ space) available to photons of frequency ν. If this number is ρ_ν then $\rho_\nu d\Omega_p d\nu d\underline{r}$ is the number of phase space cells that can be occupied at the volume element $d\underline{r}$ by photons in the interval $[\nu, \nu+d\nu]$ propagating in a direction subtended by the solid angle $d\Omega_p$. For a structureless particle of any mass,

$$n(p)dpd\Omega_p d\underline{r} = (1/h^3)d\underline{p}d\underline{r}, \qquad (1.36)$$

where n(p) is the number of phase space cells available for a particle with momentum p. Since $d\underline{p} = p^2 dpd\Omega$, $n(p) = p^2/h^3$. For photons the internal degeneracy corresponds to two polarization states that a photon can occupy at any given kinematic state. So $\rho_\nu = 2n(p)dp/dr = 2\nu^2/c^3$. Then the intensity I_ν is given by $c\rho_\nu E_\nu$, where E_ν is the energy of all the photons in a given phase space cell. Since all the photons have the same frequency, ν, $E_\nu = n_\nu h\nu$ where n_ν is the photon occupation number (or the number of photons in the cell). Thus,

$$I_\nu = 2\ (h\nu^3/c^2)\ n_\nu. \qquad (1.37)$$

So the mean intensity in the ij line or in the field multiplied by $c^2/2h\nu^3$ is the photon occupation number. Using this definition, the photon occupation number of the blackbody radiation is the Planck distribution, I_{BB}, multiplied by $c^2/2h\nu^3$ or $H_{jk} = 1/[\exp(h\nu/kT_B) - 1]$. For the free-free continuum field, the intensity is

$$I_{FF} = \frac{2h\nu^3}{c^3} \quad \frac{1}{\exp(h\nu/kT_e) - 1} [1 - \exp(-\tau_c)], \qquad (1.38)$$

where τ_c is the free-free continuum optical depth and the $[1 - \exp(-\tau_c)]$ term is the attenuation that the radiation generated inside the sphere of the H II region undergoes before it reaches the surface. So the photon occupation number of the free-free radiation field is

$$D_{jk} = \frac{[1 - \exp(-\tau_c)]}{\exp(h\nu/kT_e) - 1} W(r). \qquad (1.39)$$

The equations have been solved by approximating ortho H_2CO by its four lowest rotational levels (see figure 1.4 - levels with K = 1). The ratio of the populations for the lowest levels is given by

$$\frac{n_2}{n_1} = \frac{pP_{12} + P_{13}P_{34}P_{42}}{pP_{21} + P_{24}P_{43}P_{31}}, \qquad (1.40)$$

where $p = P_{31}(P_{42} + P_{43}) + P_{42}P_{34}$.

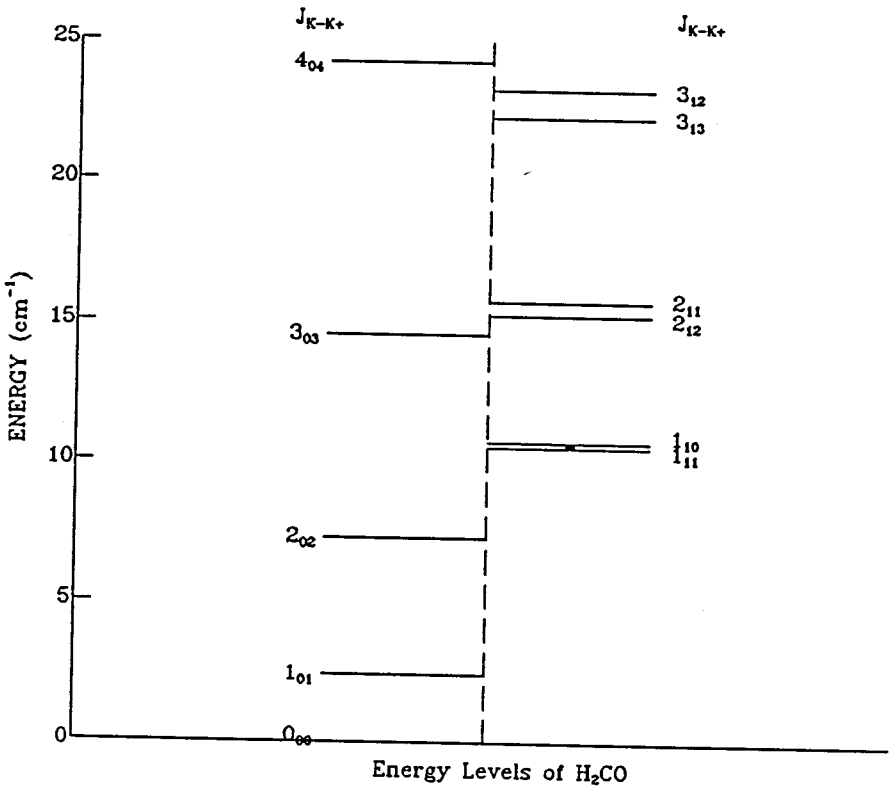

Figure 1.4 - Energy level diagram of H_2CO. The levels on the left of the dashed line are the para-H_2CO levels and those on the right are the ortho-H_2CO levels. The 6 cm maser transition (1_{10} - 1_{11}) is indicated by the black line.

For the conditions of population inversion in the ground state doublet one has

$$\frac{P_{34}P_{42}}{P_{43}P_{31}} \; \frac{P_{13} - q(1 + P_{31}/P_{34})}{P_{24} + q} > 1, \qquad (1.41)$$

where $q = P_{21} - P_{12} = \beta_{21}A_{21}$.

Assuming all the lines are optically thin ($\beta_{ij} = 1$), and neglecting the background radiation field ($H_{ij} = 0$), one gets

$$\begin{aligned} P_{jk} &= A_{jk}\ (1 + D_{jk}) \qquad (j>k) \\ &= A_{jk}\ D_{jk}\ g_k/g_j \qquad (j<k). \end{aligned} \qquad (1.42)$$

The only free parameters in the above equations are contained in D_{jk} and are the wavelength λ_0 where the H II region becomes optically thick, and W, the geometrical dilution factor, which depends on the distance of the masing gas to the H II region. Boland and de Jong also demonstrate the result of a more realistic calculation by including 14 levels of ortho-H_2CO and taking into account the effects of collisions with H_2 molecules and the effects of radiation trapping. The effect of including more levels is to increase the population inversion of the ground state, the effect of including collisions is to narrow the range of λ_0 where the inversion occurs and the effect of including radiation trapping is to reduce somewhat the inversion.

For $T_e = 10^4$ K, $E_m = 6 \times 10^8$ cm^{-6} pc (Harris and Scott, 1976), d = 3.5 kpc (Israel et al. 1973), $R_{II} = 2.4 \times 10^{16}$ cm, $n_e = 2 \times 10^5$ cm^{-3},

and λ_0 = 2.7 cm in NGC 7538 IRS 1, Boland and de Jong (1981) conclude that the J=1 H_2CO doublet can be inverted by free-free continuum radiation if the H II region is very compact with emission measures in the range 10^8 - 10^{10} cm^{-6} pc. Also assuming a geometrical dilution factor of 0.5, a density $n(H_2)$ of $3x10^4$ cm^{-3}, a gas kinetic temperature T_k of 20K, a formaldehyde abundance $x(H_2CO)$ = $n(H_2CO)/n(H_2)$ = 4 x 10^{-7}, and a velocity gradient dv/dr of 1280 km s^{-1} pc^{-1}, they conclude from their model that if λ_0 < 3 cm, both the 1_{10} - 1_{11} transition and the 2_{11} - 2_{12} transition are inverted while for 3 cm < λ_0 < 10 cm only the 1_{10} - 1_{11} transition is inverted.

The model for NGC 7538 IRS 1 requires that the masing gas be in front of the H II region so that it amplifies the radio continuum radiation. The millimeter line photons must be able to escape from the cloud to allow for sufficiently rapid radiative pumping, and this requires a large velocity gradient. Also, the molecules must be lined up in velocity over long pathlengths to create sufficient amplification. Boland and de Jong assume that the H II region moves through the molecular cloud at a velocity of 10 km s^{-1} and that the molecular gas in front of it gets pushed sideways, creating velocity gradients of ~ V/R_{II} perpendicular to the line of sight and coherent pathlengths of ~ R_{II} along the line of sight. With these assumptions they derive a hydrogen density of $n(H_2)$ ~ 3 x 10^4 cm^{-3}, T_K ~ 20 K and $x(H_2CO)$ = $n(H_2CO)/n(H_2)$ ~ 8 x 10^{-7}, to obtain an amplification factor of ~ 100.

The main aim of this project has been to test the conditions

required by the Boland and de Jong (1981) model for the H_2CO emission. The parameters which have been used in the model, like n_e, T_e, E_m, and λ_0 need to be tested with high resolution observations. A model for the H II region, as the one described in the above section, would require continuum observations at the millimeter and centimeter wavelengths which are of high enough resolution to resolve IRS 1 and IRS 2 and, if possible, resolve the small structure of IRS 1. One could then obtain the turnover frequency and the emission measure that would provide a direct test of the maser model. Such observations do exist at centimeter wavelengths (Campbell 1984; Dickel et al. 1981). However, the millimeter fluxes have not been obtained with such high accuracy. With present interferometric techniques one can obtain high resolution observations at millimeter wavelengths where the H II region is assumed to be optically thin. In addition to the continuum flux densities, one can use millimeter spectral lines as density probes of the molecular cloud. The molecules with the best known collision cross sections are HCN and CO. HCN thermalizes at densities $> 10^6$ cm^{-3} and can be used as a probe of the high density material. CO and its isotope ^{13}CO can be used to probe the lower density material ($> 10^4$ cm^{-3}). For this purpose, ^{13}CO would be a better choice since CO is, in most cases, highly saturated. With the Hat Creek Millimeter Array, one has a powerful tool to probe the small-scale structure at various H_2 densities. HCO^+ is another molecule that can be used to probe higher densities, although the HCO^+ - H_2 collision cross sections are not as well known. But HCO^+ can be used to study the high

density, high velocity material close to the source in order to map the velocity structure of the material close to the H II region.

Thus a detailed model of the H II region and its surrounding molecular cloud can be built which in turn can be used to examine conditions for maser excitation.

II. OBSERVATIONAL BACKGROUND

§2.1 NGC 7538 - Optical and Infrared Observations

NGC 7538 is an emission region of ~ 7′ diameter at l = 111°.5, b = +0°.8. Distance estimates to this complex range from 2.8 kpc (Campbell and Persson, 1988) to 3.5 kpc (Harris and Scott, 1976). The complex consists of an optical nebula with a central O7V star and an extended molecular cloud to the south of the nebula. Wynn-Williams et al. (1974) and Werner et al. (1979) discovered eleven infrared sources throughout the complex. All but two of the sources have optical counterparts (Lynds and O'Neil, 1986). The most extensively studied of these sources are IRS 1, IRS 2, and IRS 3, which are strong radio sources as well (Martin, 1973). Lynds and O'Neil (1986) have made an optical study of this region. They calculate continuum fluxes for IRS 1 and IRS 2 at several wavelengths in the visible region (λ = 4693 Å to λ = 8290 Å). They detected H_α, [NII], and [SII] lines in the northern part of the nebulosity associated with IRS 2 and calculated the emission line intensities for these transitions. IRS 1 appears brighter than IRS 2 on a V plate (Elsasser et al. 1982) and is still seen on a B plate. This phenomenon was interpreted in terms of an anomalous extinction for IRS 1 that points to the presence of large-sized dust grains. The anomalous extinction can be represented as a

wavelength independent term in the extinction law. This extra term was found to be largest for IRS 1 which also has the strongest 10 μm absorption (Willner 1976) and the highest electron density (4.5×10^4 cm^{-3} - Martin 1973). IRS 1 and IRS 2 are thought to be late O type stars while IRS 3 is thought to be a B1 ZAMS star on the basis of its luminosity and radio flux. The evidence of the high extinction toward IRS 1 indicates that it may be one of the youngest O stars identified on a blue plate.

Willner (1976) finds a deep silicate absorption feature toward IRS 1 and a 12.8 μ Ne II emission line toward IRS 2. The data imply a gas to dust ratio of 75 and a visual extinction A(V) of ~ 90 mag. for IRS 1. For IRS 2 the calculated gas to dust ratio is ~ 3×10^4 (which is an upper limit) and an A(V) of ~ 20 mag. The visual extinction for IRS 3 is found to be about 34 mag. These values of A(V) are crude estimates based on the depth of the silicate absorption feature. Werner et al. (1979) derive a lower limit for the extinction toward IRS 1 of ~ 30 mag. from spectrophotometry at 2.2 μm.

Several detailed IR studies of this region have been done. Hackwell et al. (1982) observed NGC 7538 IRS 1, IRS 2 and IRS 3 at 5 μm, 10 μm and 20 μm with a spatial resolution of 3".5 to study the spatial morphology and the energetics of the region. These observers resolved the three sources and calculated their IR luminosities. The luminosities were adjusted for the effects of silicate absorption, assuming that the 20 μm extinction was 30% of that at 9.7 μm (Willner 1976). Hackwell et al. (1982) found excellent agreement between the

TABLE 2.1

Infrared Observations of NGC 7538 IRS 1

Wavelength (μm)	Beam (")	Flux (Jy)	Reference
2.2	15	0.19 ± 0.02	1
4.8	9	41.0 ± 6	1
5.0	3.5	60.0 ± 6	2
8.7	9	67.0 ± 9	1
10.	3.5	100. ± 10	2
11.2	9	47.0 ± 7	1
12.5	9	149. ± 21	1
20	3.5	160. ± 16	2
25	6	640. ± 130	1
30	40	2300. ± 690	1
50	40	6700. ± 2010	1
85	30	8000. ± 730	3
100	55	11000. ± 3300	1
149	50	7000. ± 410	3
350	30	249. ± 7	4
1365.8	3.5	2.0 ± 0.3	5

1) Werner et al. (1979); 2) Hackwell et al. (1982);
3) Thronson and Harper (1979); 4) Chini et al. (1986);
5) Woody et al. (1989).

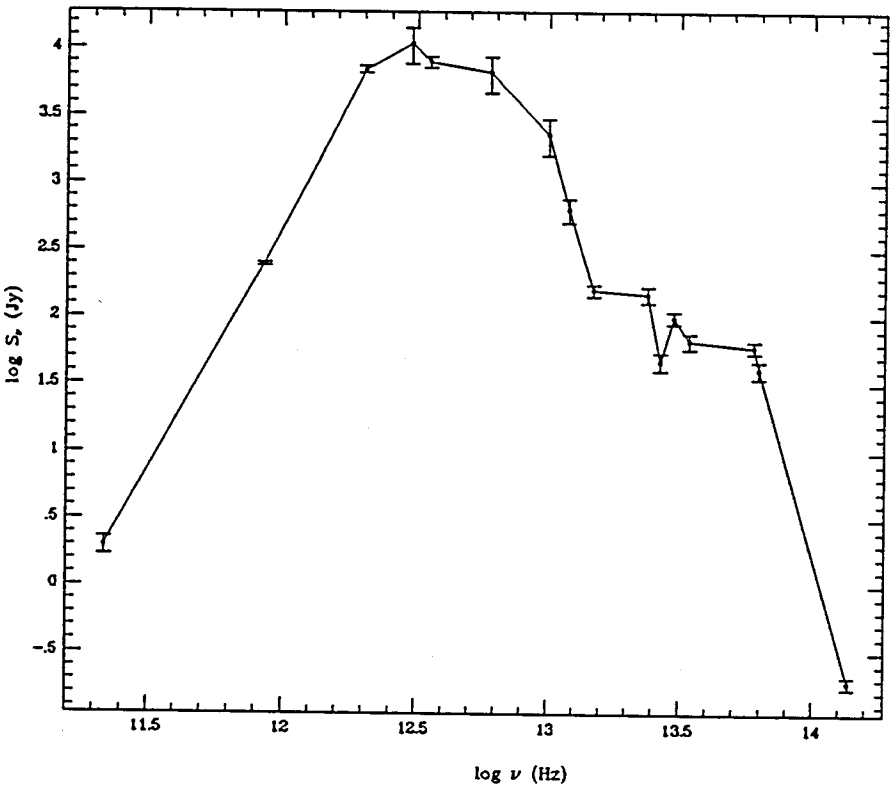

Figure 2.1 - Infrared spectrum of IRS 1. The plot shows the silicate absorption feature. The points between 50 μm and 350 μm also include the flux contribution from IRS 2.

extrapolated near-IR and measured far-IR luminosities, which suggested that the 10, 20, and 100 μm radiation all emanate from the same dust. This agreement also suggested that the dust emission occured primarily at the boundary between the ionized and the neutral regions. They also found a remarkable coincidence between the infrared and radio continuum sources, and found that the radio and 20 μm contours are remarkably similar to one another. In Table 2.1, column 1 lists the infrared wavelengths, column 2 lists the spatial resolution of the observations, column 3 lists the observed flux and column 4 gives the references. The fluxes of IRS 1 are given for wavelengths from 2.2 μm to 1 mm and Figure 2.1 shows a log S_ν - log ν plot of the information in the table. The fluxes between 50 μm and 350 μm are measured with beam sizes that are too large to resolve the three IR sources. This implies that the measured fluxes have contributions from all three sources. However, between 4.8 μm and 25 μm the fluxes are closer to the actual contribution from IRS 1 and at 5, 10 and 20 μm the measured flux contribution is solely from IRS 1. The 1 mm continuum results (from Werner et al. 1979) show that IRS 1, 2, and 3 are located within a dense molecular cloud at the southern edge of the optical HII region. These observations result in a mass of $\sim 9 \times 10^3$ $M_\odot$ and a size of ~ 2 pc for the molecular cloud. Chini et al. (1986) observed the source at 350 μm and 1300 μm. They model the distribution for $\lambda < 20$ μm ($\log\nu > 13.18$) and predict a void inner region (radius $\sim 3 \times 10^{17}$ cm) surrounded by a thick dust envelope. The total visual extinction was found to be about 60 mag. Longward of 20 μm, IRS 1 contributes an

unknown fraction to the far IR emission since it is not resolved. The total luminosity was found to be 3.7×10^5 $L_\odot$.

§2.2 Radio Continuum Observations

Radio continuum observations resolving IRS 1-3 into individual components were first made by Martin (1973) at 2.7 GHz with a resolution of 11" and at 5 GHz with a resolution of 2", and later at 5 GHz, by Israel (1977) with a resolution of 7". Harris and Scott (1976) resolved IRS 1 to a size of 1".2x0".7 at 15 GHz. IRS 1 was found to be an ultracompact H II region while IRS 2 was found to be a compact H II region[1]. Campbell (1984a) mapped IRS 1 at 5 GHz with a 0".3 resolution (Figure 2.2a) and at 15 GHz with a resolution of 0".1 (Figure 2.2b). The 5 GHz map showed IRS 1 to consist of two components - a circular component and a northern extension. The peak of the emission is at the center of the circular southern component. The structure of the source at 15 GHz was found to be similar to the 5 GHz continuum structure with a circular southern component and a northern extension. The peak of the extension was, however, shifted northward by about 0".5 from the peak of the 5 GHz emission. IRS 1 appeared to have a peanut-shaped core, which was consistent with the predictions of Harris and Scott (1976). Campbell (1984a) explains the double lobed structure of the

---

[1] Ultracompact HII regions, as defined by Israel et al. 1973, have $d < 0.1$ pc (3×10^{17} cm) and $n_e > 10^4$ cm^{-3} whereas compact HII regions have 0.1 pc $< d <$ 1 pc and 10^4 cm^{-3} $> n_e > 10^3$ cm^{-3}.

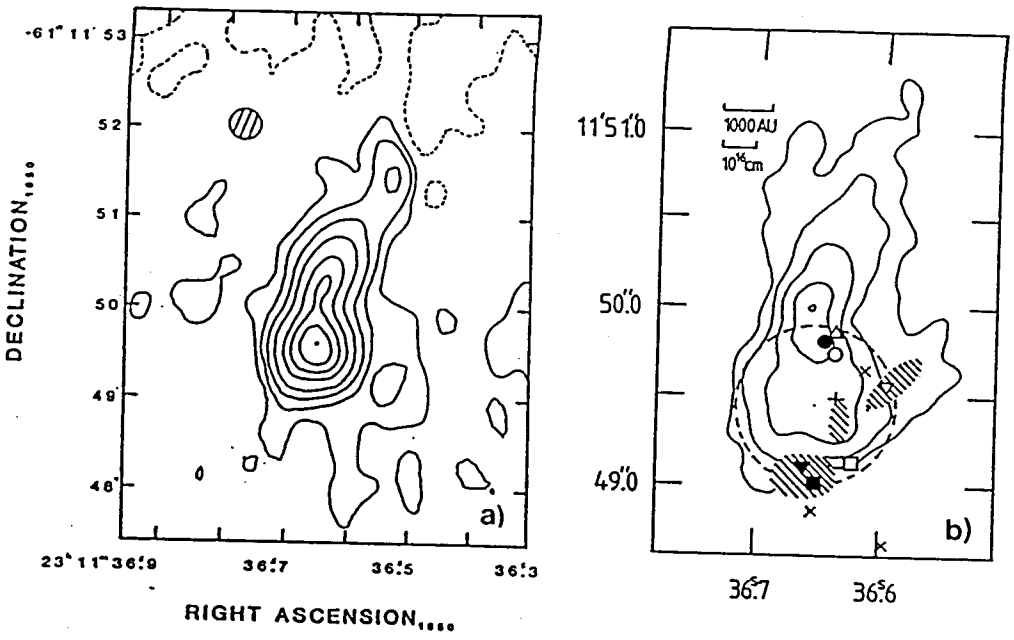

Figure 2.2 - a) 5 GHz continuum map of IRS 1 from Campbell (1984a). The hatched circle in the top left hand corner shows the beamsize of the observation. b) 15 GHz continuum map of IRS 1 from Campbell (1984a). The dashed circle indicates the extent and position of the peak of the 5 GHz continuum map. The symbols in the map are the various masers observed toward IRS 1. A full explanation of the symbols can be found in Table 2.4 along with a discussion of the masers (§2.4).

TABLE 2.2

Radio Continuum Observations of NGC 7538 IRS 1

Frequency (GHz)	Beam (")	Flux (Jy)	Reference
2.7	7.5x5.1	$0.03\ ^{+0.01}_{-0.015}$	2
4.83	0.49x0.41	0.111 ± 0.009	1
8.1	2.5x1.7	0.104 ± 0.01	2
15.0	0.36x0.34	0.418 ± 0.01	3
23.87	2.5x2.2	0.6 ± 0.1	4
110.2	7x7	2.55 ± 0.025	5
219.5	3x3	2.0 ± 0.3	6

(1) Rots et al. (1981); (2) Wink and Altenhoff (1975);
(3) Campbell (1984a); (4) Henkel et al. (1984);
(5) Scoville et al. (1986); (6) Woody et al. (1989)

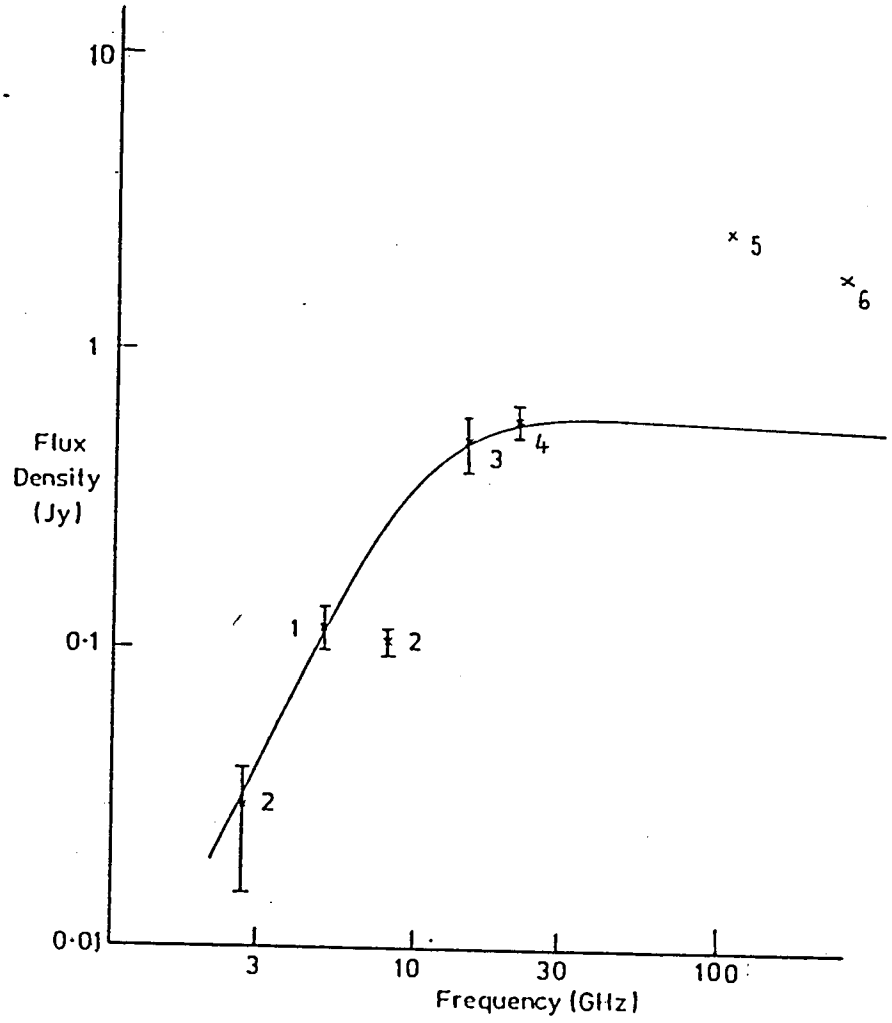

Figure 2.3 - H II region spectrum for IRS 1. The solid line is the spectrum calculated by Harris and Scott (1976) assuming a T_e of 10^4 K and an electron density of 2×10^5 cm^{-3}. The references to the observed points are - (1) Rots et al. (1981); (2) Wink and Altenhoff (1975); (3) Campbell (1984a); (4) Henkel et al. (1984); (5) Scoville et al. (1986); and (6) Woody et al. (1989). The exact frequencies and fluxes are indicated in Table 2.2.

emission as being caused by a collimating disk with an associated outflow of ionized gas. Added evidence for the presence of such a disk was seen in the 5 μm map of Hackwell et al. (1982). The emission appeared to have an east-west elongation which could be interpreted as a dusty disk. The northern extension of the continuum emission could be a collimated outflow of ionized gas. The circular southern component could be due to the ionized outflow running into higher density material south of the H II region.

In Table 2.2, column 1 gives the radio frequencies for the continuum observations of IRS 1; column 2 gives the spatial resolution; column 3 gives the flux densities; and column 4 gives the references for the observations. The H II region spectrum for IRS 1 is plotted in Figure 2.3. This spectrum was obtained by Harris and Scott (1976), assuming an electron temperature of 10^4 K and an electron density of 2×10^5 cm^{-3}. The fluxes above 15 GHz have been added to the plot to check the fit. At higher frequencies the calculated spectrum does not fit the observed data points. Scoville et al. (1986) have found that the 2.7 mm (110.2 GHz - point 5 on Figure 2.3) continuum flux is a factor of 6-9 greater than the centimeter wave continuum fluxes. The spectrum appears to rise continuously from 6 cm to 2.7 mm. If this excess is due to dust emission, the amount of dust required would be on the order of 5300 $M_\odot$. They conclude that the excess continuum emission seen at 2.7 mm is best modeled as free-free emission from an ionized outflow wind. The mass loss rates required to account for the free-free flux is ~ 10^{-3} $M_\odot$ yr^{-1} for IRS 1. The 2.7 mm

continuum flux appears to be higher than the flux at 1 mm (219.5 GHz - Woody et al. 1989 - point 6 on Figure 2.3), which does not fit in with the continuously rising spectrum. At 1 mm one expects emission from the dust to start contributing. The fact that the flux density at 1 mm is lower than the 2.7 mm flux does not fit in with the model proposed by Scoville et al.

One of the objectives of this project was to examine the millimeter continuum fluxes at 86 GHz and 110 GHz and propose a detailed model for the H II spectrum.

§2.3 Molecular Observations

Table 2.3 gives a summary of low resolution molecular observations that have been made toward NGC 7538 IRS 1 (Churchwell and Bieging 1982). Column 1 gives the molecule; column 2 gives the spatial resolution of the observations; column 3 gives the measured V_{LSR} of the molecular line toward the source; and column 4 gives the journal reference. These observations establish the existence of an extended molecular cloud situated to the south of the visible H II region NGC 7538. The cluster of IR sources, IRS 1, 2, and 3 are situated in this cloud near the interface between the high density gas and the optical nebula. Dickel, Dickel, and Wilson (1982) mapped the extent of the ^{13}CO emission from this region. Their maps showed that the molecular cloud extends for about 10′ south of the visible H II region and has an east-west extent of about 3^m. The ^{13}CO emission shows the presence

TABLE 2.3

Molecular Observations Toward NGC 7538 IRS 1

Molecule	HPBW (′)	V_{LSR} (km s^{-1})	Reference
CN	1.1	-57.2	1
CS (J=1-0)	2.6	-56.8	2
CS (J=2-1)	1.5	-57.1	2
CO	1.0	-57.0	3
SO	1.2	-57.2	4
CH	15	-56	5
	15	-52	5
HCO^+	1.2	-56.8	6
	1.2	-57.5	7
	1.3	-58.2	8
HCN	1.3	-57.7	7,9
	1.3	-58.0	1
HNC	3	-56.5	10
NH_3	2.1	-58	11
C_2H	1.3	-56.8	12
H_2S	0.75	-57.2	13
N_2H^+	1.2	-57.1	7
CH_3OH	1.2	-56.3	14

(1) Churchwell and Bieging (1982); (2) Ho, Martin and Barrett (1981); (3) Campbell and Thompson (1984); (4) Gottlieb et al. (1978); (5) Rydbeck et al. (1976); (6) Snyder et al. (1976); (7) Turner and Thaddeus (1977); (8) Hollis et al. (1975); (9) Morris et al. (1976); (10) Snell and Wootten (1979); (11) Schwartz et al. (1977); (12) Tucker, Kutner and Thaddeus (1974); (13) Thaddeus et al. (1972); (14) Gottlieb et al. (1979).

of a ridge of high column density extending east-west with local maxima at each end. The cold self-absorbed H I gas is south of this ridge. High excitation emission from CS, HCN, H_2CO, and H_2S was found in the region around and to the south of the cluster of IR sources (IRS 1, 2, and 3), which implies a region of high density in this region. The ^{13}CO ridge pointed to a density gradient across the interface between the molecular cloud and the visible H II region which was confirmed by Campbell and Thompson (1984). The compact high density region around IRS 1, 2, and 3 was also mapped by Ho et al. (1981). Their CS (J=1-0 and J=2-1) observations showed the peak of the emission to be at the IRS 1 position. However, their NH_3 [(J,K)=(1,1)] map showed the peak to be about 1.5′ south of IRS 1. Observations of H_2 S(1) line emission with a 34" resolution (Fischer et al. 1980) showed that the emission peak was at a position between the optically visible H II region and the IRS 1, 2, and 3 group. It was unclear whether the driving agent of this emission was associated with the visible H II region to the north or the IR cluster to the south.

Campbell and Thompson (1984) also detected a high velocity molecular outflow indicated by the extended line wings in the CO (J=1-0) emission. They reported that the outflow was large (r ~ 1.3 pc) and massive (M ~ 75 $M_\odot$). Their map of the outflow did not show a separation between the blue and red lobes of the emission. Fischer et al. (1985) mapped the region around IRS 1 in the same transition of ^{12}CO with a 44" beam. Their results differed from those of Campbell and Thompson (1984). Fischer et al. (1985) did find a separation

between the two velocity components of 0.6′ (~ 0.5 pc at a distance of 2.8 kpc) along a line at a position angle[2] of 145°. The observations of the outflow also led them to conclude that the H_2 emission was caused by the outflow running into the visible H II region. Kameya et al. (1989) have also mapped the entire NGC 7538 region in the CO transition. They detect high velocity wings around IRS 9 and IRS 11 in addition to the one around IRS 1.

High resolution maps of this outflow were made by Scoville et al. (1986) with a beamsize of 7". Their maps showed a clear separation between the blue and red lobes of the outflow oriented at a position angle that agrees with the low resolution results. The orientation of the outflow is a bit of a puzzle since the high resolution continuum map at 15 GHz shows evidence for an ionized outflow that is oriented in the north-south direction. This means that from scales of 0".1 to 7" the outflow undergoes a change in direction of 55°. Kameya et al. (1989) propose an explanation for this change by invoking a density enhancement to the northeast and southwest of IRS 1, which channels the outflow and changes its direction. Scoville et al. (1986) also map the emission in the J=1-0 transition of ^{13}CO and find an elongated structure extending about 22" across IRS 1. The ^{13}CO emission exhibits a velocity shift of 8 km s^{-1} over its spatial extent. They suggest that the ^{13}CO structure could play a significant role in the evolution of the IRS 1 H II region and the molecular outflow.

---

[2] Position angles are typically measured in degrees east of north.

TABLE 2.4

Masers Associated with IRS 1

Molecule	Frequency (MHz)	LSR Velocity (km s^{-1})	Position α(1950):23^{h}11^m	Position δ(1950):61°11′	Symbols
OH[a]	1665.4	−58.4 ± 0.1	36.653 ± 0.025	48.853 ± 0.249	×
		−58.9	36.597 ± 0.022	48.697 ± 0.229	×
		−59.2	36.615 ± 0.021	49.636 ± 0.240	×
		−59.6	36.60 ± 0.02	49.652 ± 0.150	▽
		−59.9	36.598 ± 0.021	49.652 ± 0.153	▽
		−60.1	36.597 ± 0.023	49.659 ± 0.167	▽
OH[a]	1667.4	−59.9 ± 0.1	36.60 ± 0.02	49.670 ± 0.150	▽
		−59.4	36.623 ± 0.022	49.495 ± 0.162	+
OH[b]	1720.5	−56.2 ± 0.1	36.659 ± 0.010	49.00 ± 0.10	■
		−56.6	36.658	49.00	■
		−57.1	36.649	49.05	■
		−57.6	36.655	49.05	■
		−57.8	36.661	49.11	▼
		−59.1	36.624	49.13	□
		−59.4	36.623	49.15	□
OH[c,d]	4765.6	−57.06 ± 0.05	36.65	49.0	▨
		−58.75	36.60	49.6	▨
		−59.19	36.65	49.0	▨
		−60.10	36.63	49.4	▨
H_2CO[e]	4829.7	−57.9 ± 0.4	36.645 ± 0.014	49.82 ± 0.10	●
		−60.1	36.637	49.74	○
CH_3OH[f]	12178.6	−56.39 ± 0.01	36.64 ± 0.25	49.9 ± 0.25	△
		−60.0	...	...	...
NH_3[g,h]	18499.4	−60.0 ± 0.01	36.5	46.0	...
H_2O[i,j]	22235.1	−60.8 ± 0.2	36.47 ± 0.05	49.4 ± 0.	...
		−70.7	36.6 ± 0.4	49 ± 3	...
		−84.4	...	...	...
		−89.4	...	...	...
$^{15}NH_3$[h,l]	22879.4	−55.6 ± 0.1	36.6	48.0	...
		−56.1 ± 0.2	...	...	...
		−58.5 ± 0.5	...	...	...
		−59.7 ± 0.2	...	...	...
		−60.1 ± 0.2	...	...	...
HCN clumps[m]	88631.8	−55.75 ± 0.25	35.4 ± 4.7	1′09.1 ± 4.5	...
		−57.75	37.7	50.0	...
		−58.25	40.1	40.0	...
			37.0	40.0	...
			33.2	55.9	...
		−59.0	37.3	45.0	...
		−60.0	35.8	44.5	...

[a] Norris *et al.* 1982.
[b] Forster *et al.* 1982.
[c] Velocities from Gardner and Martin-Pintado 1983.
[d] Palmer, Gardner, and Whiteoak 1984. The absolute positions of the masers were not given, but the positions of the three regions where groups of masers were found were indicated. Since the positions are of the areas of maser emission, no errors are given.
[e] Rots *et al.* 1981.
[f] Batrla *et al.* 1987.
[g] Madden *et al.* 1986.
[h] The observations were made with single-element radio telescopes so the maser positions could not be determined accurately.
[i] Genzel and Downes 1976.
[j] Forster *et al.* 1978.
[l] Mauersberger, Wilson, and Henkel 1986.
[m] This paper.

Subsequent sections of this thesis will present high resolution results in the J=1-0 transitions of HCN, HCO^+, and ^{13}CO. A detailed study of the high density gas around IRS 1 will be made from these results.

§2.4 Masers Associated With IRS 1

Figure 2.2b shows the 15 GHz continuum map (Campbell 1984a) with all the maser emission sources. The figure shows that all the masers are associated with the southern part of the ultracompact H II region NGC 7538 IRS 1, apparently at the interface between the density confined ionized gas and the neutral gas. The dashed circle indicates the position and extent of the 5 GHz continuum peak. Table 2.4 lists the molecules that have observed maser emission toward IRS 1 in column 1, the maser frequencies in column 2, the LSR velocities in column 3, and the maser positions in column 4. Column 5 gives a list of the symbols used to mark the various maser positions in Figure 2.2b and Figure 4.1b. The list of HCN clumps are from Pratap, Batrla, and Snyder (1989 - Appendix B). The OH masers all have velocities in the range from -56.2 km s^{-1} to -60.1 km s^{-1}. The 1720 MHz OH masers are generally found in two spatially separated velocity groups, one with velocities lower than -58.0 km s^{-1} and the other with higher velocities. The 1665 MHz and the 1667 MHz OH masers have velocities that are mostly lower than -58.0 km s^{-1}. The positions of the 1720 MHz and the 1665 MHz OH masers have been obtained from VLBI measurements

(Forster et al. 1982; Norris et al. 1982). The 4765 MHz OH maser has three main components which are at -57.06, -58.75 and -59.19 km s^{-1}. There is also a component of the 4765 MHz emission at -60.1 km s^{-1}, which is situated near the 5 GHz continuum peak. The description of the symbols corresponding to the various masers in Figure 2.2b is given in the last column of Table 2.4. The 1720 MHz, the 1665 MHz, and the 4765 MHz OH masers all appear to be associated with the southern component of the HII region. The masers are spatially grouped, but their different velocity components are not necessarily correlated. This may be due to masers that arise from different points along the line of sight that are affected by the velocity field around the expanding HII region. The components of the 1665 MHz OH maser that have velocities higher than -59.0 km s^{-1} appear to be offset to the south of the HII region. The H_2CO masers do not seem to be spatially coincident with any of the OH masers, even though the velocities of the two H_2CO masers are within the same range as that of the OH masers. In fact, Guilloteau and Lucas (1981) conclude that since the 1720 MHz OH spectrum is much more complex than the H_2CO spectrum, and since the two masers are not spatially coincident on small scales, they arise in regions with different excitation conditions. Similar conclusions have been drawn regarding the coincidence of the 4765 MHz OH masers (Palmer et al. 1984) and the main line OH masers (Norris et al. 1982) with the H_2CO maser spots. However, recent VLBI measurements of the CH_3OH maser position in this source (Menten et al. 1988) indicate that this maser is, within the errors, spatially coincident

with the H_2CO masers. In addition, the two velocity components that have been observed also coincide with the velocities of the H_2CO masers. The H_2O maser, which has a strong component at -60.1 km s^{-1} and several weaker components at much lower velocities, is situated just off the map to the west of IRS 1 in Figure 2.2b. The NH_3 and $^{15}NH_3$ masers are not shown in the figure since interferometric position measurements have not been made. The NH_3 emission is assumed to be maser emission from the narrow line widths and the high brightness temperatures (Madden et al. 1986). In the case of the $^{15}NH_3$ maser, the line was assumed to be a maser by a comparison with the (J,K) = (1,1) and (2,2) absorption lines and the limit for the (4,4) line (Mauersberger et al. 1986).

Since observations have, in general, ruled out radiative pumping mechanisms for the OH masers around HII regions (Elitzur 1985), collisional pumping schemes have to be considered. The typical H_2 densities required for inverting the OH maser lines with collisions are of the order of 10^7 cm^{-3}. Such densities can be achieved in dense shells around HII regions (Elitzur and de Jong 1978). In IRS 1 the OH masers appear to be situated around the edge of the ionized region, which is consistent with the above model. The H_2CO maser, however, requires a different model to explain the observed emission because H_2 densities $\geq 3 \times 10^5$ cm^{-3} quench the maser. According to the Boland and de Jong model, the H_2CO maser is inverted by free free emission from the HII region and requires densities of $\approx 3 \times 10^4$ cm^{-3} (§1.5.3).

The observations presented in this thesis will attempt to map a

detailed density structure for the molecular cloud around IRS 1. The high resolution will allow the study of the density conditions required for the excitation of the various masers. In particular, the condition for the H_2CO maser will examined in order to explain why this maser is not observed in more sources in the galaxy.

III. MOLECULAR OBSERVATIONS OF NGC 7538 IRS 1

§3.1 Interferometer Observations and Setup

The observations for this thesis were made with the 3-element Berkeley - Illinois - Maryland Array (BIMA) at Hat Creek, California and the 12-m NRAO telescope.

The Hat Creek system consists of three telescopes, each with a diameter of 6 m. The receivers are double sideband, double conversion with the first IF at 1300-1780 MHz and the second at 70-550 MHz (Urry et al 1985). The first local oscillator (LO) is a Gunn oscillator that can be tuned to any frequency in the range 8.5 - 11 GHz. It is locked to a harmonic of a ~730 MHz reference. The two oscillators are also phase switched by different Walsh function square wave patterns. The selection of proper switching intervals for the two local oscillators allows the signals arriving at the correlator outputs from the two sidebands of the first LO to have different patterns. By proper sequential storing of the correlator outputs the signals from the two sidebands are automatically separated. The correlator has 512 spectral channels for each baseline pair, half from each sideband. In addition, the input to each baseline correlator can be chosen to pass through one, two, or four analog filters. The center frequencies of each filter may be set to any frequency in the range 80-520 MHz of the IF band and the filter widths may be selected to be 80, 40, 20, 10, or 5 MHz. This setup allows simultaneous observations of several spectral

Figure 3.1 - a) Hat Creek correlator setup for the observation of the J=1-0 transition of HCN. b) Correlator setup for the observation of the J=1-0 transition of HCO^+. c) Correlator setup for the observation of the J=1-0 transition of ^{13}CO.

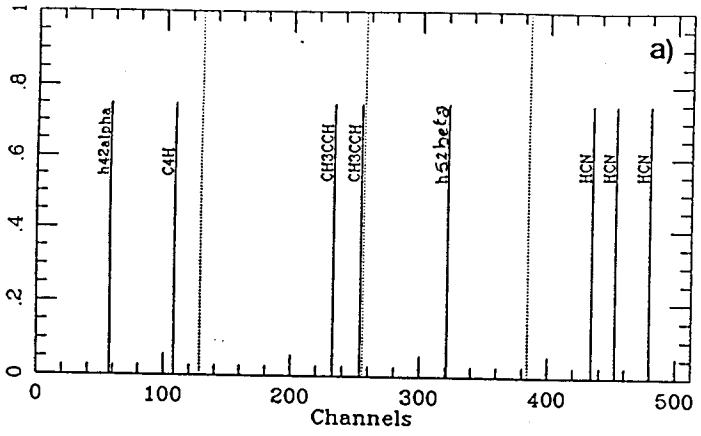
a)
h42alpha
C4H
CH3CCH
CH3CCH
h52beta
HCN
HCN
HCN
0
.2
.4
.6
.8
1
0
100
200
300
400
500
Channels

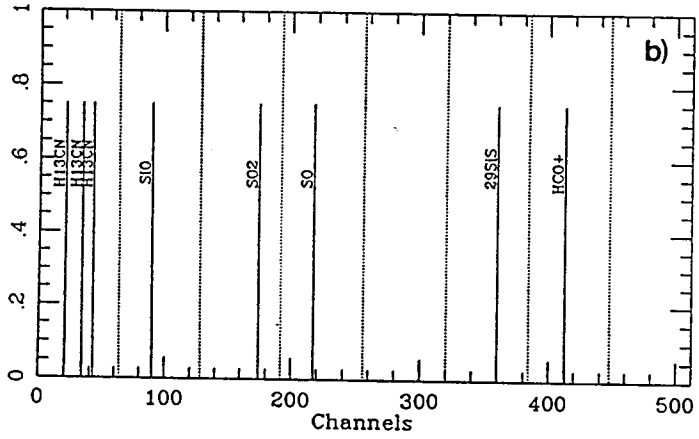
b)
H13CN
H13CN
H13CN
SiO
SO2
SO
29SiS
HCO+
0
.2
.4
.6
.8
1
0
100
200
300
400
500
Channels

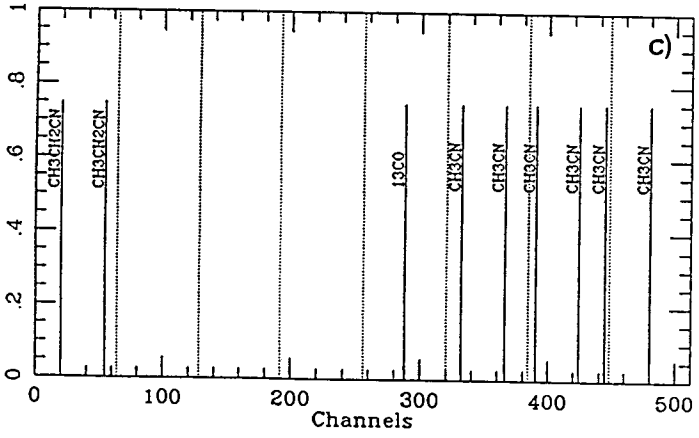
c)
CH3CH2CN
CH3CH2CN
13CO
CH3CN
CH3CN
CH3CN
CH3CN
CH3CN
CH3CN
0
.2
.4
.6
.8
1
0
100
200
300
400
500
Channels

lines in the upper and lower sidebands.

Figure 3.1a shows one of the correlator setups used for the HCN observations. This HCN setup used two analog filters in each sideband with filter widths of 10 and 40 MHz. The HCN line was set in the first filter of the upper sideband, The second filter in the upper sideband was tuned to the H42β recombination line. One of the filters in the lower sideband was tuned to the H52α recombination line. This setup resulted in a velocity resolution of 0.25 km $s^{-1}chan^{-1}$ for the HCN line and 1.0 km $s^{-1}chan^{-1}$ for the recombination lines. Figure 3.1b shows the HCO^+ setup which used four filters in each sideband with filter widths of 10 MHz each which gave a velocity resolution of 0.5 km $s^{-1}chan^{-1}$. The lines that can be observed with this setup are shown in the figure. Figure 3.1c shows the ^{13}CO setup which also used four filters in each band with filter widths of 20 MHz which resulted in a velocity resolution of 1.0 km $s^{-1}chan^{-1}$. Table 1 gives the molecule (column 1), the corresponding frequencies (column 2) and the various transitions (column 3) which were observable in the three setups.

The (u,v) coverage for the HCN and HCO^+ data ranged from the most compact spacings to the longest spacings and is seen in Figures 3.2a and 3.2b. Figure 3.2c shows the coverage for the ^{13}CO data. The instrumental phase was calibrated using the quasar BL Lac for all the observations. The RF passband shapes were calibrated using either 3C 84 or 3C 273.

TABLE 3.1

Molecular Transitions Observable in the

Hat Creek Correlator Setups

Molecule	Frequency (GHz)	Transition
H52β	85.40599	recombination line
H42α	85.68840	recombination line
SO	86.09355	2(2)-1(1)
SO_2	86.15371	39(9,31)-40(8,32)
SiO	86.24344	J=2-1, v=1
$H^{13}CN$	86.33877	J=1-0, F=1-1
	86.34018	J=1-0, F=2-1
	86.34227	J=1-0, F=0-1
HCN	88.63042	J=1-0, F=1-1
	88.63185	J=1-0, F=2-1
	88.63394	J=1-0, F=0-1
^{13}CO	110.20135	J=1-0
CH_3CN	110.34966	6(4)-5(4), F=7-6
	110.34980	6(4)-5(4), F=5-4
	110.36497	6(3)-5(3), F=7-6
	110.36452	6(3)-5(3), F=5-4
	110.37505	6(2)-5(2), F=7-6
	110.38140	6(1)-5(1), F=7-6

Figure 3.2 - a) (u,v) tracks for the interferometer observations of the HCN line. b) (u,v) tracks for the interferometer observations of HCO^+. c) (u,v) tracks for the observations of the ^{13}CO observations. The plot includes the tracks generated from the single dish data to fill in the short spacings.

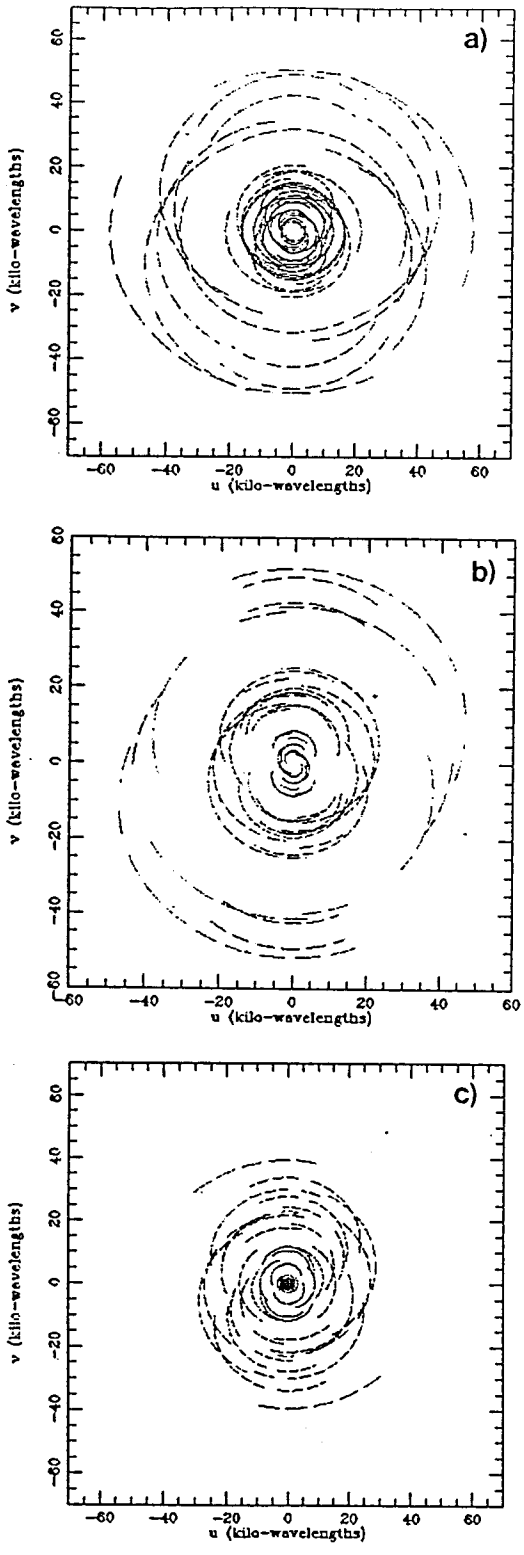
a)
b)
c)
v (kilo-wavelengths)
u (kilo-wavelengths)
-60
-40
-20
0
20
40
60

The flux density calibration was done using either a convenient planet or the strong quasars that were used for the RF passband calibration. First the raw interferometer data were phase and amplitude calibrated. Then the visibility data were gridded, convolved, and Fourier transformed using the RALINT data reduction software system. The HCN and HCO^+ results were examined with a ~9" beam and a ~3" beam. The low resolution data establish the large scale structure of the cloud while the high resolution data trace the small scale structure of the cloud.

§3.2 Combining Single Dish and Interferometer Data

The short spacings in the interferometer data were filled in with data from a single element telescope (the NRAO 12-m telescope). This procedure is necessary when there are large scale structures in the cloud that are not properly sampled by the interferometer. With proper sampling of the field, the single dish data can be added to the interferometer data in order to get the true brightness distribution of the source and a proper representation of the extended structure of the cloud.

Theoretically one can describe the process of combining the interferometer and single dish data as follows (Vogel et al. 1984). The visibility measured with an interferometer is

$$V_I(u,v) = \{[V(u,v)] * [b_I(u',v,)]\}\, s_I(u,v), \qquad (3.1)$$

where u,v = baseline coordinates projected in the plane of the sky, V(u,v) = Fourier transform (F.T.) of the true brightness distribution, $b_I(u,v)$ = F.T. of the interferometer beam pattern, and $s_I(u,v)$ = sampling function. The * denotes two dimensional convolution. The synthesized map is the F.T. of V_I and is written as

$$T_I(x,y) = \{[T(x,y)][B_I(x,y)]\} * S_I(x',y'), \qquad (3.2)$$

where $S_I(x',y')$ is the synthesized beam.

V_I is usually time averaged, weighted, convolved, and resampled onto a regular grid in order to perform a Fast Fourier Transform. The single dish measurements are represented by

$$T_S(x,y) = \{[T(x,y)]*[B_S(x',y')]\}\ S_S(x,y), \qquad (3.3)$$

where B_S = beam pattern of the single dish, and S_S = sample grid. The F.T. of T_S can be written as

$$V_S(u,v) = \{[V(u,v)]*[b_S(u,v)]\}\ s_S(u',v'). \qquad (3.4)$$

V_S can be measured but one needs the true visibility, V, at short spacings. If the single dish data are properly sampled (see the criteria below), the convolution in equation 3.4 can be ignored and the true visibility can be written as

$$V'(u,v) = V_S(u,v)/b_S(u,v) \qquad (3.5)$$

In order to combine equation 3.5 with the interferometer visibilities, V′ must be convolved with the F.T. of the beam pattern of the interferometer antennas and sampled at points s′. Then

$$V'_I(u,v) = \{[V'(u,v)]*[b_I(u',v')]\}\ s'(u',v'), \qquad (3.6)$$

The following criteria have to be met in order to get a proper sampling of the field:

1. The diameter of the single dish, D_s, should be greater than the radius of the central "hole" in the interferometer sampling grid, which is usually comparable to the diameter of the interferometer antennas, D_I; b_S goes to zero at D_S so the derived visibilities at spacings near D_S will be scaled by a large factor in equation 3.5. So it is preferable to have D_S as large as possible compared with D_I. The single dish data must have a higher signal to noise ratio and the beam of the single dish must be better known, the closer D_I is to D_S. Generally, the single dish diameter should be a factor of 2 to 3 larger than the interferometer antenna diameter.
2. The single dish data must be sampled at sufficiently fine intervals, $\Delta x \Delta y$, to avoid aliasing caused by the convolution with $s_S(u',v')$ (eqn. 3.4). The condition is $1/\Delta x \Delta y(\text{rad.}) > 2D_S(\text{wavelengths})$, which translates to sampling twice per beamwidth.
3. The region sampled by the single dish should include the field of

view of the interferometer or the actual emitting region.

4. The visibilities derived from the single dish data should have a signal to noise comparable to those measured by the interferometer in order not to degrade the combined maps.

The procedure followed to combine the two sets of data was as follows:

1. The single dish data were scaled by a Jy/K factor to convert the antenna temperatures to Jy/beam. For Kitt Peak spectral line data, calibrated by chopper wheel or vane, this conversion factor (which is the ratio of the forward gains of the two antennas) is

$$S_\nu/T_R^* = (\eta_l \eta_{fss}/\eta_A)\ (2k/A_p), \qquad (3.7)$$

where η_l = rear spillover efficiency = 0.85, η_{fss} = forward spillover efficiency = 0.75, A_p = physical aperture = 113 m^2, η_A = aperture efficiency = $\eta_{A0}\ \exp[-(4\pi\sigma/\lambda)^2]$, η_{A0} = infinite wavelength aperture efficiency = 0.52, and σ = r.m.s surface accuracy = 85 μm.

2. The spectra were then used to make single dish maps which were deconvolved by the single dish beam (which was assumed to be a two-dimensional gaussian).

3. The deconvolved single dish maps were then convolved by the interferometer primary beam. This set of data was used to generate visibilities at the short spacings. The longest of these short spacings was chosen to overlap with the shortest interferometer spacing wherever possible so that the amplitude calibration could be checked.

The single dish measurements were made with the NRAO 12-m telescope following the above criteria. The FWHM of the 12-m telescope beam was about 70" at 89 GHz. The HCN and HCO^+ observations consisted of a 7x7 grid of measurements centered on $\alpha(1950) = 23^h11^m37^s$, $\delta(1950) = 61°11'49"$. The points were separated by 30" and the frequency resolution was 100 kHz $chan^{-1}$. The integration time at each point was increased toward the center of the grid in order to get a constant signal to noise across the map after a deconvolution of the beam. Baselines were subtracted from the spectra and the data were transformed into interferometer format. The data were multiplied by a Jy/K factor of 32.0 to convert T_R^* into flux density. A symmetric gaussian of 60"x60" was deconvolved from the data to get an estimate of the true sky brightness distribution. This distribution was then convolved with the primary beam of the interferometer (FWHM ~ 2'.1) and model (u,v) visibilities were calculated for spacings ranging from 0.09 to 1.3 kλ. The derived (u,v) data retained the frequency resolution of the original single dish spectra. A similar procedure was followed for the ^{13}CO data with the scaling factors chosen for the higher frequency.

§3.3 HCN Results

Figure 3.3 presents channel maps across the F=2-1 component of the J=1-0 transition of HCN. The visibility data corresponding to six configurations of the three element array were used to make these

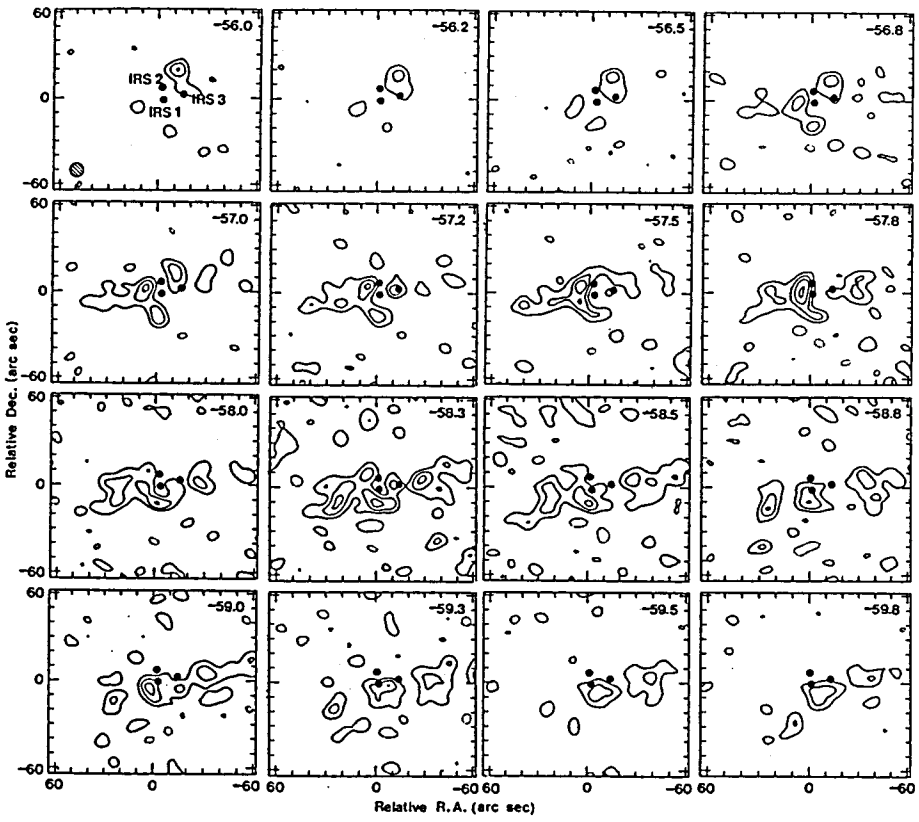

Figure 3.3 - Channel maps over the velocity interval covering the HCN (J=1-0, F=2-1) line. The three solid circles show the positions measured by Hackwell et al. (1982) for the infrared sources IRS 1 ($\alpha(1950) = 23^h11^m36^s.7\pm0.2$; $\delta(1950) = 61°11'48"\pm1$), IRS 2 ($23^h11^m36^s.8\pm0.2$; $61°11'56"\pm1$), and IRS 3 ($23^h11^m35^s.0\pm0.2$; $61°11'51"\pm1$). A label at the top right of each panel displays the LSR velocity corresponding to that map. The hatched circle at the bottom left of first panel outlines the FWHM of the synthesized beam. The lowest contour is at 1.2 Jy/beam and the subsequent contours levels are at intervals of 1.2 Jy/beam. The (0,0) pixel position in the maps is at $\alpha(1950) = 23^h11^m37^s$ and $\delta(1950) = 61°11'50"$.

maps. The raw data were gridded and Fourier transformed to obtain 256x256 maps with a pixel size of 2". A continuum map, which was constructed from the 15 channels at each end of the correlator segment, was subtracted from each channel map. The resulting maps were then CLEANed to an r.m.s. noise level of 0.8 Jy/beam. The FWHM of the synthesized beam is 9" in declination and 9".4 in right ascension and can be seen in the panel corresponding to a velocity of -56.0 km s^{-1}. The channel maps are plotted with contours at equal intervals of 1.2 Jy/beam with the lowest contour at 1.2 Jy/beam. The velocity structure of the HCN emission is shown relative to the positions of the three IR sources, IRS 1, IRS 2, and IRS 3. The HCN emission is very pronounced to the northwest of IRS 1 at velocities between -56.0 km s^{-1} and -57.0 km s^{-1} with a peak value of 3.6 Jy/beam at -56.0 km s^{-1}. The peak of the emission then shifts to the east and south of IRS 1 as the velocity approaches the LSR velocity of the molecular cloud associated with the source (V_{LSR} = -58 km s^{-1}). As the velocity becomes more negative, the emission peak shifts to the southwest of IRS 1. The HCN emission thus appears to trace a cavity around IRS 1. Note that the HCN emission never peaks at the IRS 1 position. In addition, there are two emission peaks along the east-west direction which are offset by about 25" on either side of IRS 1. These peaks can be most clearly seen in the channel map corresponding to a velocity of -58.3 km s^{-1}.

Figure 3.4 shows a sample HCN spectrum taken at a position of ($\Delta\alpha$, $\Delta\delta$) = (5".0, 5".0), which corresponds to one of the clumps to the east of IRS 1 and which is at one edge of the cavity. The line

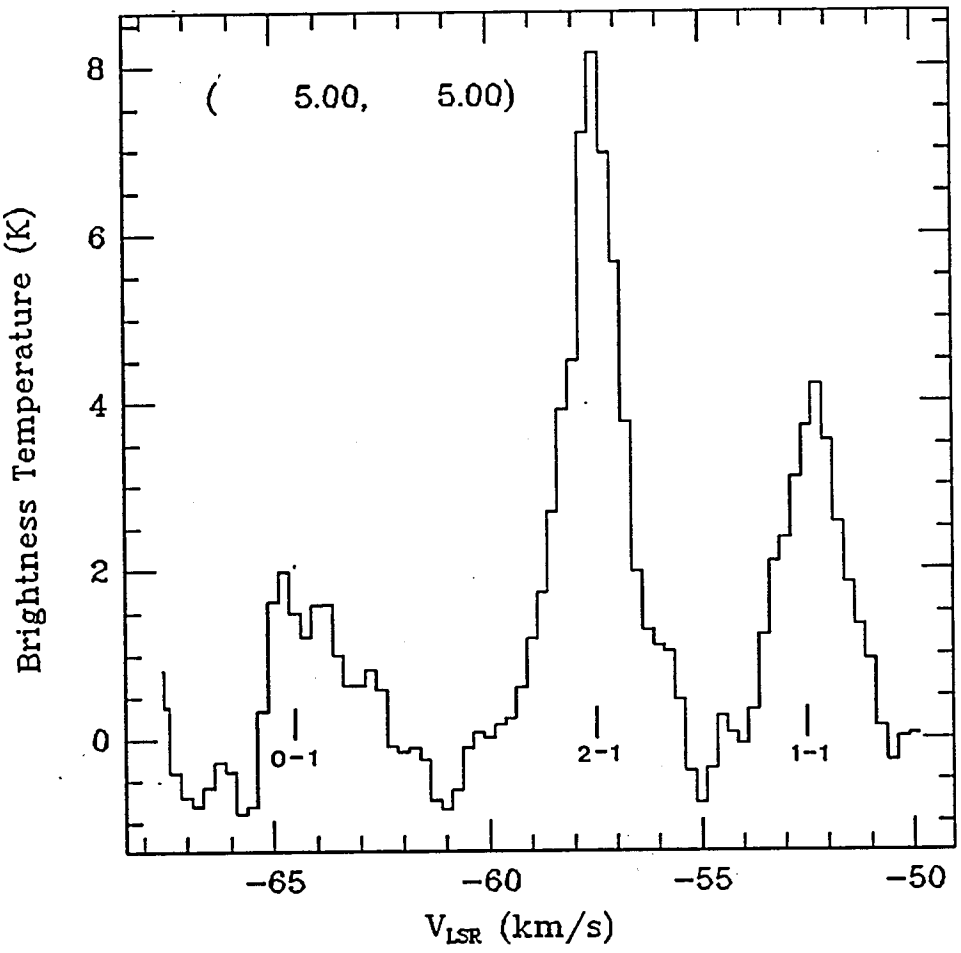

Figure 3.4 - A spectrum of the J=1-0 transition of HCN which is taken at a map position of $(\Delta\alpha, \Delta\delta) = (5''.0, 5''.0)$ relative to $\alpha(1950) = 23^h11^m37^s$ and $\delta(1950) = 61°11'50''$. The vertical lines indicate the positions of the hyperfine components.

profiles of the HCN transitions have widths of the order of 2 - 3 km s^{-1}, which are an order of magnitude wider than thermal line widths associated with kinetic temperatures of ~ 30 - 50 K (Δv ~ 0.14 - 0.18 km s^{-1}). The wide linewidths may either be due to small scale clumps withn the cloud or due to turbulent velocities in the cloud. This question can be answered by looking at the high resolution maps of HCN. Thus, the HCN maps provide strong evidence for large scale clumps and suggestions of small scale clumps in the molecular cloud around IRS 1 and IRS 2, which could thus provide the necessary density conditions for the complex maser excitation around IRS 1.

Figure 3.5 shows the high resolution maps across the same transition of HCN. These maps have been made by adding single dish data to the interferometer data (as described in the previous section). The combined set of visibility data were gridded and Fourier transformed to obtain a cube of 256x256x45 maps with a pixel size of 1" and a velocity resolution of 0.5 km s^{-1}. The visibilities were first weighted uniformly (which weights the data by the density of points within each grid cell in the (u,v) plane and then by the square of the system temperature. The FWHM of the resulting synthesized beam is 3".0x2".8 (which can be seen in the upper left hand corner of the panel corresponding to a velocity of -57.0 km s^{-1}). The maps were then CLEANed, resulting in an r.m.s. noise level, in a single channel, of 0.25 Jy/beam. The total flux in the combined maps is consistent with the flux in the single dish maps.

The channel maps (Figure 3.5) show the clumpy nature of the

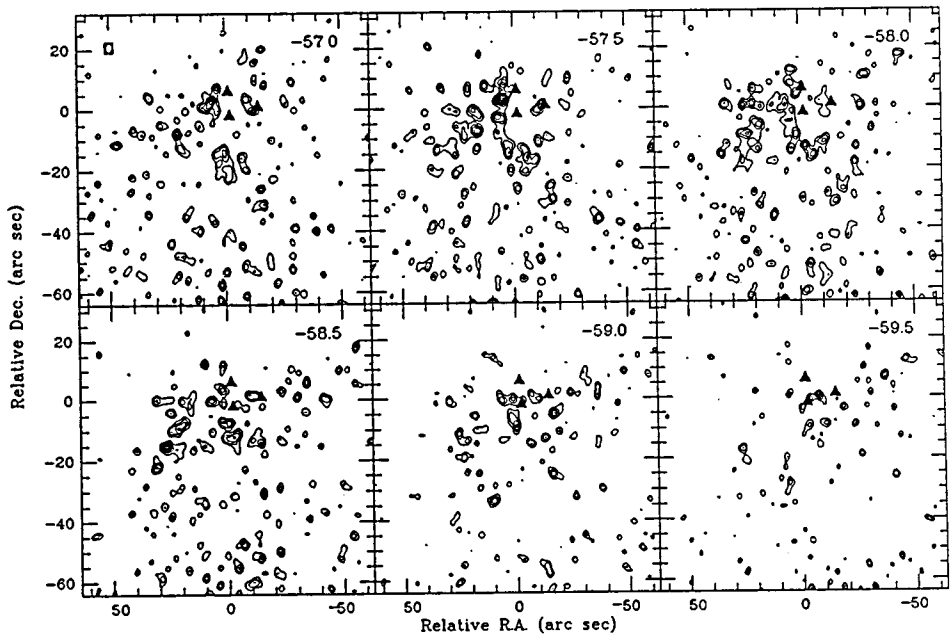

Figure 3.5 - Channel maps across the J-1-0 transition of HCN. The contours are at intervals of 0.75, 1.0, 1.25, 1.5, 1.75, 2.0, 2.25, and 2.5 Jy/beam. The FWHM of the beam is indicated in the upper left hand corner of the map corresponding to a velocity of -57.0 km s^{-1}. The three solid triangles correspond to the positions of IRS 1, IRS 2, and IRS 3. The (0,0) pixel position of each map is at $\alpha(1950) = 23^h11^m37^s$, $\delta(1950) = 61°11'50"$.

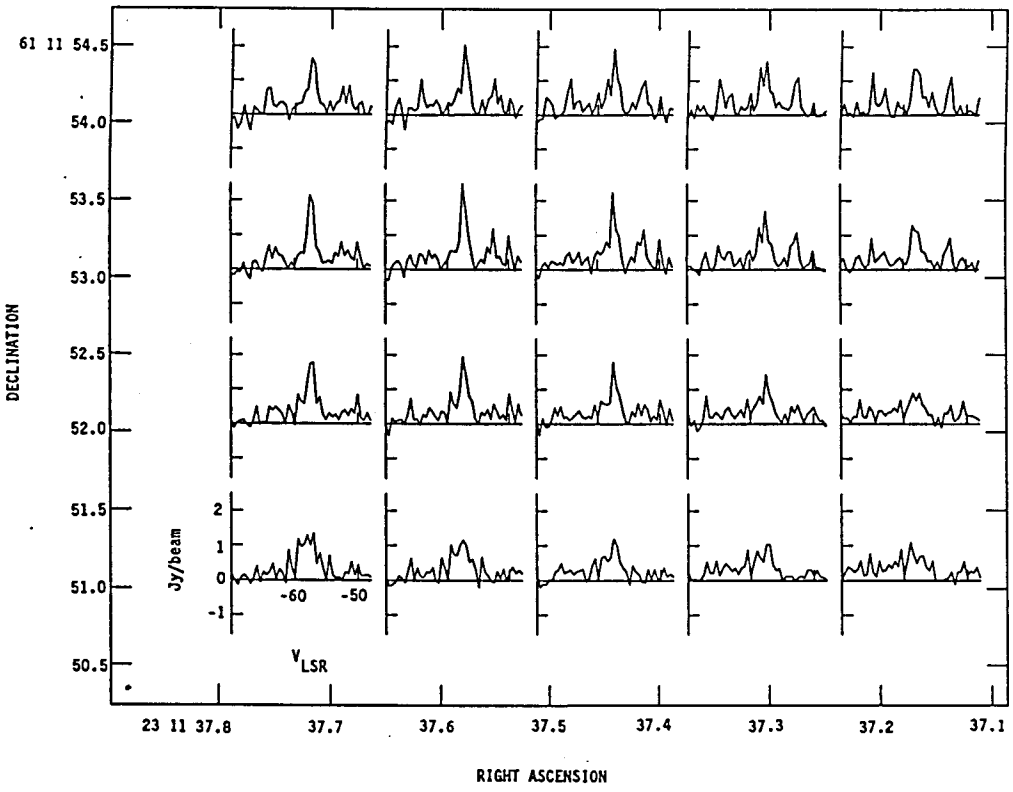

Figure 3.6 - Raster of HCN spectra around the strongest HCN peak ($\alpha(1950) = 23^h11^m37^s.6$; $\delta(1950) = 61°11'52".5$). IRS 1 is to the southwest of the plot. The spectra show that the linewidths are narrower than those seen in the low resolution data.

molecular cloud surrounding IRS 1, which confirms the prediction made from the line profile in the low resolution data. The line widths of the spectra from the high resolution maps, shown in Figure 3.6, are ~ 1 km s^{-1}. The velocity resolution in the spectra are 0.5 km s^{-1} compared to 0.25 km s^{-1} in the resolution of the low resolution maps (which is also the intrinsic resolution of the interferometer data). These spectra confirm the fact that the linewidths seen in the low resolution maps are due to clumping in the cloud. The distribution of the clumps in the maps corresponding to -57.5 and -58.0 km s^{-1} emphasizes the cavity in the molecular cloud that was seen in the low resolution maps. The strongest peaks of emission are situated to the south and east of IRS 1. The clumps are strung around the H II region and form a density enhancement which surrounds the cavity. The implications of such a structure for maser emission will be discussed in the next chapter.

§3.4 HCO^+ Results

The low resolution maps across the J=1-0 transition of HCO^+ were made with data from five configurations of the interferometer with (u,v) spacings ranging from 2.0 to 25.4 kλ. The data were gridded and Fourier transformed to obtain maps of 128x128 with a pixel size of 2". A continuum map, made from an average over channels in the adjoining, line free, filter was subtracted from the channel maps. The maps were CLEANed and the resulting r.m.s. noise in one channel map was 0.375

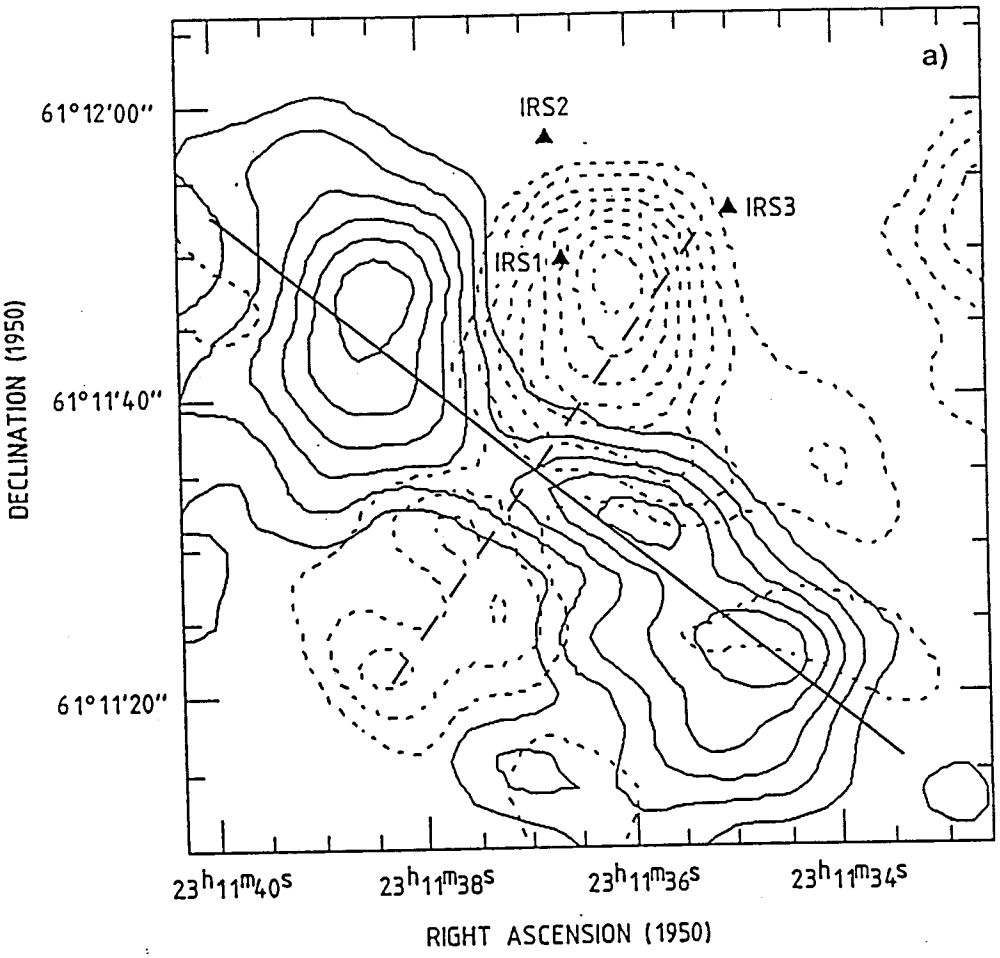

Figure 3.7 - a) Channel maps across the J=1-0 transition of HCO^+. The solid contours show the emission at -57.1 km s^{-1} and the dashed contours show the emission at -59.7 km s^{-1}. The solid line is at a position angle of 52° and the dashed line is at a position angle of 142°.5. The solid triangles mark the positions of IRS 1, IRS 2, and IRS 3.

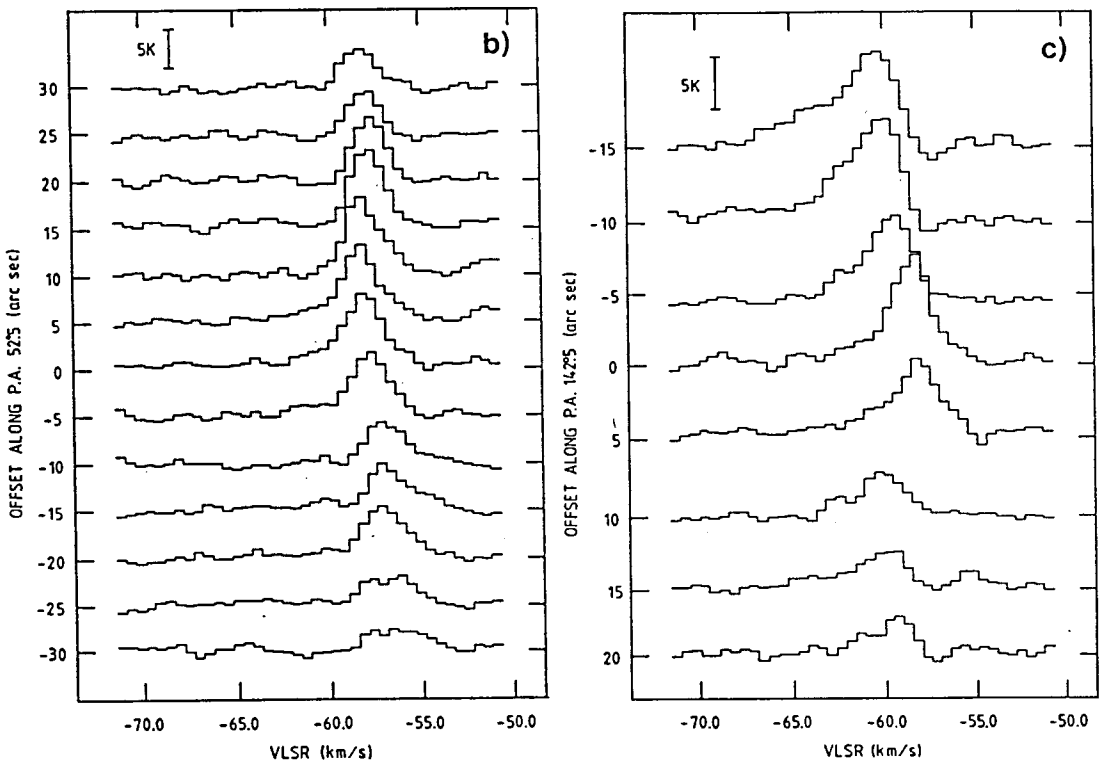

Figure 3.7 (cont.) - b) HCO^+ spectra along the solid line in Figure 3.7a. The positions are in arc seconds along a P.A. of 52° relative to $\alpha(1950) = 23^h11^m36^s.7$, $\delta(1950) = 61°11'34"$. c) HCO^+ spectra along the dashed line in Figure 3.7a. The positions are in arc seconds along a P.A. of 142°.5 relative to $\alpha(1950) = 23^h11^m36^s.7$, $\delta(1950) = 61°11'37"$.

Jy/beam. The synthesized beam was 8".5x6".7.

The main features in the channel maps across the J=1-0 transition of HCO^+ are seen in Figure 3.7a. The solid contours show the emission at a V_{LSR} of -57.1 km s^{-1} and the dashed contours show the emission at -59.7 km s^{-1}. The striking feature seen at -57.1 km s^{-1} is a symmetric double lobed structure which has a pronounced drop in intensity toward the center. The feature is highly elongated with an aspect ratio of 3.5 to 1 and is oriented at a position angle (P.A.) of 52°. The spectra along the solid line are seen in Figure 3.7b. The positions are given in arcseconds along P.A. 52°.5. relative to $\alpha(1950) = 23^h11^m36^s.7$, $\delta(1950) = 61°11'34"$. From an examination of the spectra it is evident that the drop in intensity toward the center of the structure is caused by the shift of the line peak toward more negative velocities. The dashed contours in the figure show a blue shifted emission peak that is perpendicular to the elongated structure. Figure 3.7c shows spectra along the dashed line in Figure 3.7a. The positions given are offsets in arcsecs relative to $\alpha(1950) = 23^h11^m36^s.7$, $\delta(1950) = 61°11'37"$ along a P.A. of 142°.5. At the central positions (0 and 5) the broad line wings are symmetric, which is in agreement with the above results. Toward more negative offsets, the peaks of the profiles shift to lower velocities and extremely asymmetric, strong blue shifted line wings appear. The implications of this structure toward explaining the bipolar outflow observed in this source will be discussed in the next chapter.

The high resolution channel maps across the HCO^+ line are shown in

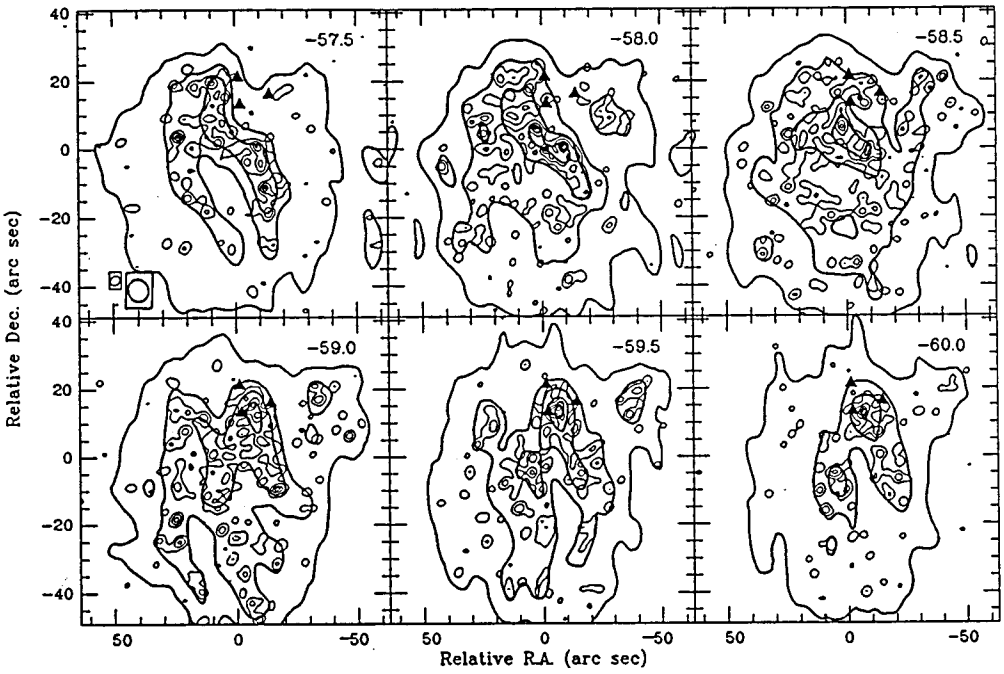

Figure 3.8 - Channel maps across the J=1-0 transition of HCO^+. The high resolution contours are at intervals of 1.0, 1.5, 2.0, 2.25, 2.5, 2.75, 3.0, 3.25, and 3.5 Jy/beam. The contours correspond to a resolution of 3".9x2".7. The bold contours are maps which have been made by convolving the high resolution data to a beam of 8.5x6".7. The contours are at intervals of 0.5, 0.8, 1.1, 1.4, and 1.6 Jy/beam. The panel corresponding to a velocity of -57.5 km s^{-1} contains the FWHM of the synthesized beams associated with of the two sets of contours. The (0,0) pixel position of each map is at $\alpha(1950) = 23^h11^m37^s$, $\delta(1950) = 61°11'35"$. The three solid triangles correspond to the positions of IRS 1, IRS 2, and IRS 3 (positions same as those in Figure 3.3).

Figure 3.8. These maps were made with the combined set of interferometer and single dish data which were gridded and Fourier transformed to obtain a cube of 256x256x45 maps with a pixel size of 1" and a velocity resolution of 0.5 km s^{-1}. The visibilities were first weighted uniformly and then by the square of the system temperature. The FWHM of the synthesized beam was 3".9x2".7. The maps were then CLEANed resulting in an r.m.s. noise level of 0.2 Jy/beam in one channel map. The data were also convolved to a beam of 8".5x6".7 in order to compare with the low resolution data (bold contours in figure).

The features in the low resolution maps agree very well with the features seen in Figure 3.7a. The high resolution data show the same features but the molecular cloud appears to be very clumpy. The elongated structure breaks up into several small clumps distributed around IRS 1 in a manner similar to the distribution of the HCN clumps (seen in panel corresponding to a velocity of -58.0 km s^{-1}). The clump parameters can be used to examine the statistical properties of such small scale clumps in the molecular cloud.

§3.5 ^{13}CO Results

Figure 3.9 shows channel maps across the J=1-0 transition of ^{13}CO. The maps were made with combined single dish and interferometer data ranging in u,v spacing from 0 to 35 kλ. The combined visibilities were gridded by weighting them uniformly and by system temperature. The

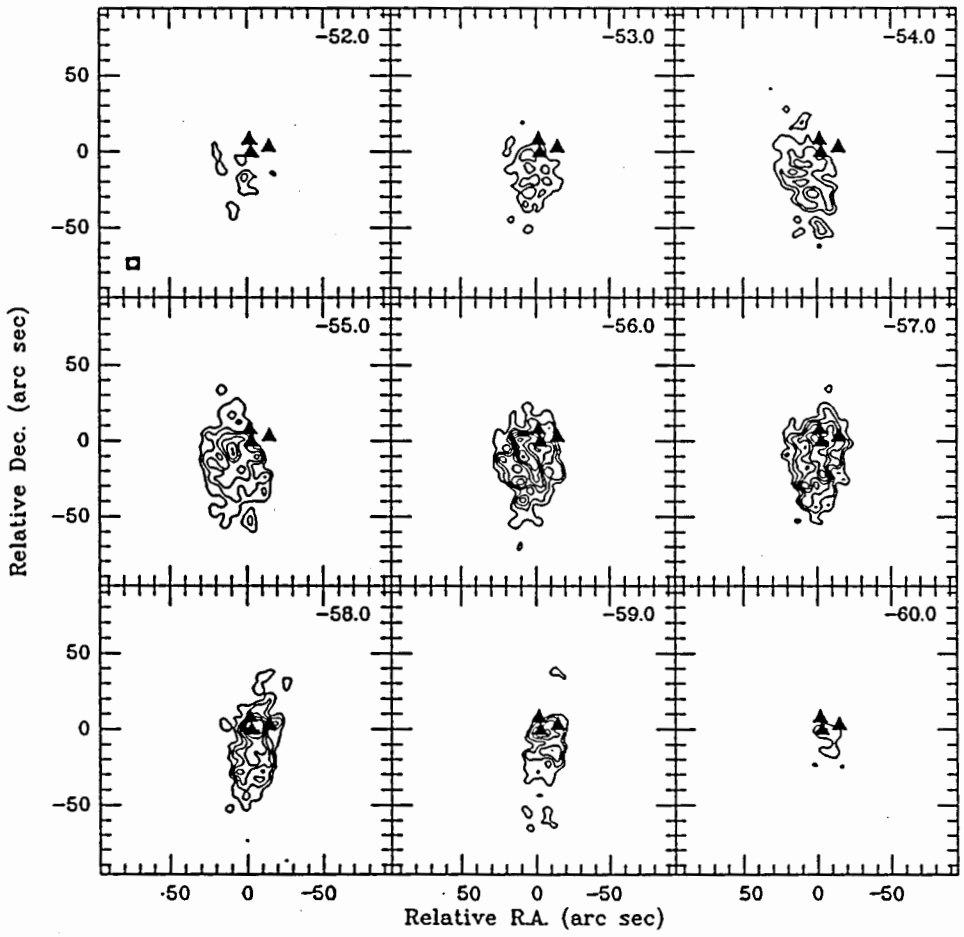

Figure 3.9 - Channel maps across the J=1-0 transition of ^{13}CO. The panel corresponding to a velocity of -52.0 km s^{-1} contains the synthesized beam in the lower left hand corner. The contours are at 3.0, 4.5, 6.0, 7.5, 9.0, 10.5, 12.0, 13.5, 15.0, and 16.0 Jy/beam. The three triangles indicate the positions of IRS 1, IRS 2, and IRS 3. The maps are centered at $\alpha(1950) = 23^h11^m37^s$; $\delta(1950) = 61°11'50"$.

gridded data were then Fourier transformed to obtain 256x256 maps with a pixel size of 1".5. The data were also tapered by a Gaussian with a FWHM of 20 kλ resulting in a synthesized beam of 6".35x5".58. The maps were then CLEANed resulting in an r.m.s noise of 0.48 Jy/beam. The velocity resolution of the maps is 1.0 km s^{-1}. The maps are centered at $\alpha(1950) = 23^h11^m37^s$; $\delta(1950) = 61°11'50"$. The size of the synthesized beam is shown in the channel corresponding to a velocity of -52.0 km s^{-1}. The contours are at 3.0, 4.5, 6.0, 7.5, 9.0, 10.5, 12.0, 13.5, 15.0, and 16.0 Jy/beam. The three triangles indicate the positions of IRS 1, IRS 2, and IRS 3. The maps show that the emission in the source appears to extend more in the north-south direction than in the east-west direction. The velocity structure also appears to be complicated. The emission in the northern part of the ^{13}CO cloud starts to the east of IRS 1 at the higher velocities (-53.0 to -56.0 km s^{-1}). Then the peak moves westward with decreasing velocity (see map corresponding to -59.0 km s^{-1}). However, the southern part of the cloud appears to have a much smaller gradient in the east-west direction. Figures 3.10a and 3.10b show position-velocity cuts across the source. Figure 3.10a is a cut along (x,y,P.A.) = (0,0,90) and Figure 3.10b is along (0,-30,90). Figure 3.10a shows the presence of a very definite gradient across the source. The two strong peaks are separated by about 1.5 km s^{-1} but the extent of the gradient is about 10 km s^{-1}. The velocity gradient extends for a spatial separation of about 60". Figure 3.10b shows that the extent, both in velocity and in space, of the gradient is reduced as one moves to the south of IRS 1.

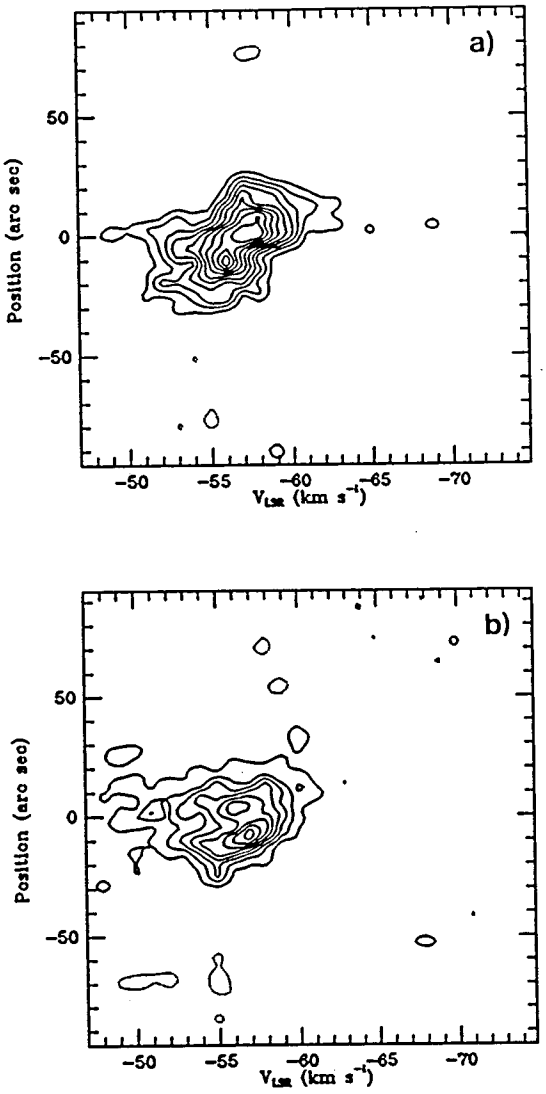

Figure 3.10 - a) Position-velocity cut across the J=1-0 transition of ^{13}CO. The cut is along (x,y,P.A.) = (0,0,90). The contours are intervals of 1.5 Jy/beam and the peak is 16.4 Jy/beam. The (0,0) position is at $\alpha(1950) = 23^h11^m37^s$, $\delta(1950) = 61°11'48''.6$. b) Position-velocity cut along the same transition along (x,y,P.A.) = (0,-30,90). The contours are at intervals of 1.5 Jy/beam and the peak value in the plot is 13.1 Jy/beam.

The velocity extent is about 8.0 km s^{-1} and the spatial extent is about 45". The emission is also not as strong to the south.

It can also be seen in the channel maps that the emission at the velocities between -56.0 km s^{-1} and -59.0 km s^{-1} shows no evidence of a cavity around IRS 1 as was seen in the HCN and HCO^+ maps. The implications of this in terms of the H_2 densities in the molecular cloud around IRS 1 will be discussed in the next chapter.

§3.6 Continuum Results

High resolution continuum maps have been made at 88.67 GHz and at 110.2 GHz. The map at 88.67 GHz was made with data in the second correlator segment in the upper sideband of the HCN setup. This correlator segment had a bandwidth of 40 MHz and was tuned to a recombination line. Since the line was not observed, the data were used to make the continuum map. This map is seen in Figure 3.11a. The map was made with an average over 25 km s^{-1}. The data were gridded uniformly and by system temperature and a 128x128 map was made with a cell size of 1". This resulted in a beam of 2".85x2".64. A CLEAN box of 31" by 24" was used which just included the three infrared sources. The resulting r.m.s noise in the map was 0.08 Jy/beam. The region around IRS 1 is shown in Figure 3.11a. The contours start at 0.3 Jy/beam and are in intervals of 0.1 Jy/beam. The peak value of the continuum emission is 1.06 Jy/beam. The beamsize is shown in the bottom left corner of the map. The peak of the continuum seems to be

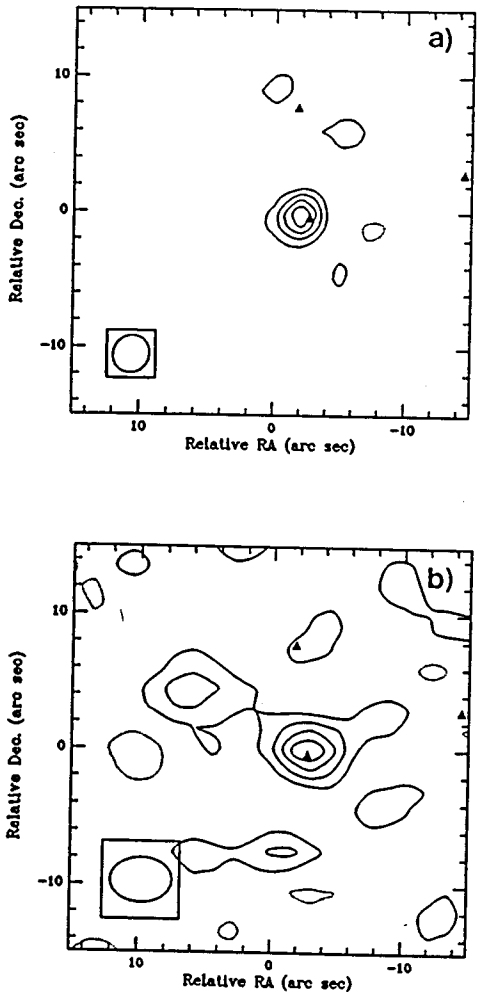

Figure 3.11 - a) Continuum map of IRS 1 at 88.7 GHz. The contours are ar intervals of 0.2 Jy/beam and the peak value in the map is 1.06 Jy/beam. The synthesized beam is indicated in the lower right hand corner and is 2".85x2".64 in size. The map is 30" square with the positions of IRS 1, IRS 2, and IRS 3 indicated by the solid triangles. b) Continuum map of IRS 1 at 110.2 GHz. The contours are at intervals of 0.2 Jy/beam and the peak value in the map is 0.996 Jy/beam. The synthesized beam is 4".57x3".31 in size. The scale of the map is the same as that of Figure 3.11a.

offset from the IRS 1 position. But since the offset is less than a beamsize it may not be significant. The continuum around IRS 1 still appears to be unresolved. So the peak value may be taken as the continuum flux at this frequency.

Figure 3.11b shows the continuum map at 110.2 GHz plotted with the same contours as Figure 3.11a. This map has been made by averaging 25 channels around the ^{13}CO line. The data were gridded uniformly and by system temperature onto a 128x128 grid with a pixel size of 1".5 resulting in a beam of 4".6x3".3. A CLEAN box of 15"x15" was used and the map was CLEANed resulting in an r.m.s noise of 0.13 Jy/beam. The peak value of the emission is 0.996 Jy/beam. The beamsize is shown in the bottom left corner of the map. The continuum map here also seems to be unresolved. These values of the continuum fluxes can now be added to the H II region spectrum. The resulting model spectrum will be discussed in the next chapter.

IV. DISCUSSION AND ANALYSIS OF MOLECULAR RESULTS

§4.1 Implications of the Molecular Emission

In analyzing the molecular maps, we assume that the emission is optically thin so that the densities probed by the various molecules are of the order of the critical densities discussed in §1.4. The validity of the assumption of low optical depths can be examined for each molecule.

In the case of ^{13}CO, several arguments can be made to show that the line is optically thin. From our own single dish spectra of ^{12}CO, ^{13}CO, and $C^{18}O$ taken at Kitt Peak, we can calculate the ratio $^{13}CO/C^{18}O$. The usual Galactic ratios, $^{12}CO/^{13}CO = 40$ and $^{12}CO/C^{18}O = 200$, give $^{13}CO/C^{18}O = 5$. From the integrated intensity in the single dish spectra, the ratio $^{13}CO/C^{18}O$ is found to be 5.8, which suggests the ^{13}CO is optically thin. In addition, optical depth estimates for the ^{13}CO line have been made by Campbell (1984b). Her study indicates that the optical depth of the J=1-0 transition of ^{13}CO across the cloud is directly proportional to $T_A^*(^{13}CO)/T_A^*(^{12}CO)$. The resulting values for $\tau(^{13}CO)$ range from 0.1 to 0.6. Using $T_B = 10$ K, $T_x = 20$ K, and $T_B(0) = 2.7$ K in equation 1.22, the higher end of the range in τ gives a ratio $n_{H_2}(c)/n_{H_2}$ of about 0.15. The low value of the ratio implies that the density in the region is at least 2×10^3 cm^{-3}, which corresponds to the thermalization of ^{13}CO.

For HCN and HCO^+, the calculation is not as simple. From single dish data the ratio of HCN to $H^{13}CN$ (integrated intensity) is about 8, while the ratio of HCO^+ to $H^{13}CO^+$ is about 10. An estimate for the HCN and HCO^+ optical depths can be made from the equation of radiative transfer,

$$\frac{T_B(12)}{T_B(13)} = \frac{T_x(12)}{T_x(13)} \frac{(1 - e^{-\tau(12)})}{(1 - e^{-\tau(13)})}, \qquad (4.1)$$

where $T_B(12)$, $T_x(12)$, and $\tau(12)$ correspond to the molecule with ^{12}C and $T_B(13)$, $T_x(13)$, and $\tau(13)$ correspond to the ^{13}C isotope.

We will assume all hyperfine components are blended together in the following discussion. If we assume the same optical depth for $H^{13}CN$ as for ^{13}CO, $\tau(13) = 0.1$. For the line with blended hyperfine components, $T_x(12) = T_x(13)$, $T_B(12)/T_B(13) = 8$, and we get $\tau(12) = 1.4$. For $T_B(12) = 4.5$ K (which is the peak value of our single dish spectrum)), $T_x = 20$ K, and $T_B(0) = 2.7$ K, equation 1.22 gives a value $n_{H_2}(c)/n_{H_2} = 1.1$. Thus, the critical densities probed by the HCN transition are still of the order of 10^6 cm^{-3}. A similar calculation for HCO^+, with $\tau(13) = 0.1$, gives $\tau(12) = 3.04$. From equation 1.22, for $T_B = 6$, we get $n_{H_2}(c)/n_{H_2} = 2.1$. This results in the critical density probed by the HCO^+ transition being reduced to about 9.5×10^4 cm^{-3}. Thus, the density interpretations made in the following sections are still valid.

The contour maps in Figure 3.3 are plotted across the strongest

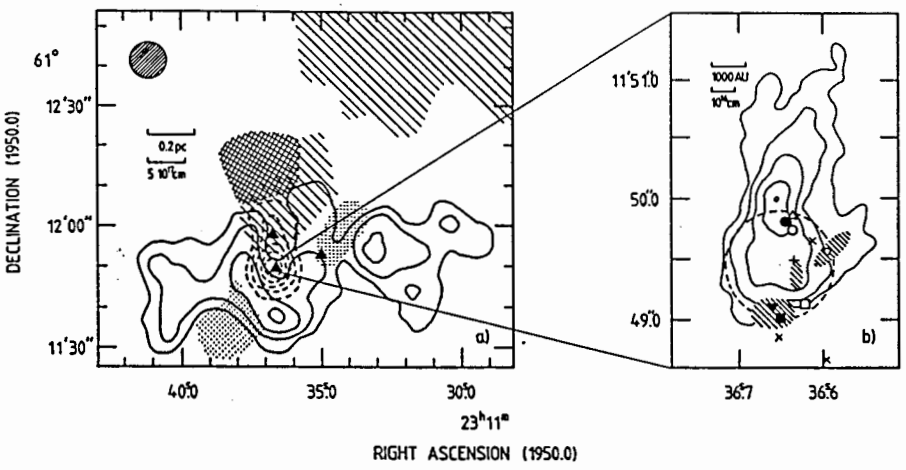

Figure 4.1 - a) Map of the average emission in the HCN (J=1-0, F=2-1) transition in the velocity interval $-61.0 \leq V_{LSR} \leq -55.0$ km/s (solid contours at intervals of 0.5 Jy/beam; the peak value in the map is 2.16 Jy/beam) overlaid with a map of the 3-mm continuum emission (dashed contours at intervals of 0.18 Jy/beam; the peak of the continuum has a value of 1.1 Jy/beam). Solid triangles mark the positions of the infrared sources IRS 1 (south), IRS 2 (north), and IRS 3 (west). The cross hatched area corresponds to the half power width of the intensity of emission from vibrationally excited hydrogen (Fischer et al. 1980), while the hatched regions outline the optical HII region (Campbell 1985) and the dotted fields outline the red (southeast) and blue (northwest) lobes of the high velocity CO emission (Scoville et al. 1986). The hatched circle at the top left gives the FWHP of the synthesized beam of the HCN observations and the 3 mm continuum observations.

b) Map of the 15 GHz continuum emission (from Campbell 1984a) overlaid with symbols denoting regions of maser emission associated with IRS 1. The symbols are explained in Table 2.4. The dashed ring indicates the extent and position of the 4.8 GHz continuum emission. The water maser position lies outside the map to the southwest. The second highest

hyperfine (J=1-0, F=2-1) component of the HCN molecule. It is evident in these maps that HCN emission never peaks at the IRS 1 position. Figure 4.1a shows a map of the emission in the J=0, F=2-1 transition of HCN averaged over the velocity interval -61.0 km s^{-1} < V_{LSR} < -55.0 km s^{-1} (solid contours). The cavity around IRS 1 is clearly seen in this map. The averaged map also emphasizes the east-west extent of the molecular material traced by HCN, which implies H_2 densities ~10^6 cm^{-3} (§1.4). The east-west structure outlines the interface between the visible H II region to the north (hatched region) and the extended molecular cloud to the south. The H II regions associated with IRS 1 and IRS 2 seem to be located at this interface, in the dense molecular gas. This is also consistent with a gradient in H_2 column density found from ^{12}CO and ^{13}CO observations (Campbell and Thompson 1984), and it indicates a sharp increase in H_2 column density from the north to south across the interface. The increase in molecular density is also evident from extinction estimates towards the infrared sources. Campbell and Thompson (1984) have found an extinction A(V) of 14 ± 6 mag. toward IRS 2 and between 37 and ~ 60 mag. toward IRS 1. This suggests that IRS 1 is more deeply embedded in the molecular material than is IRS 2.

The cavity toward the H II region is also seen in high resolution maps across the HCN line. Figure 4.2 presents a map of the emission in the J=1-0 transition of HCN (integrated over the velocity interval -58.0 km s^{-1} to -57.0 km s^{-1}) overlaid on a grey scale image of the optical emission around the infrared sources. The emission to the

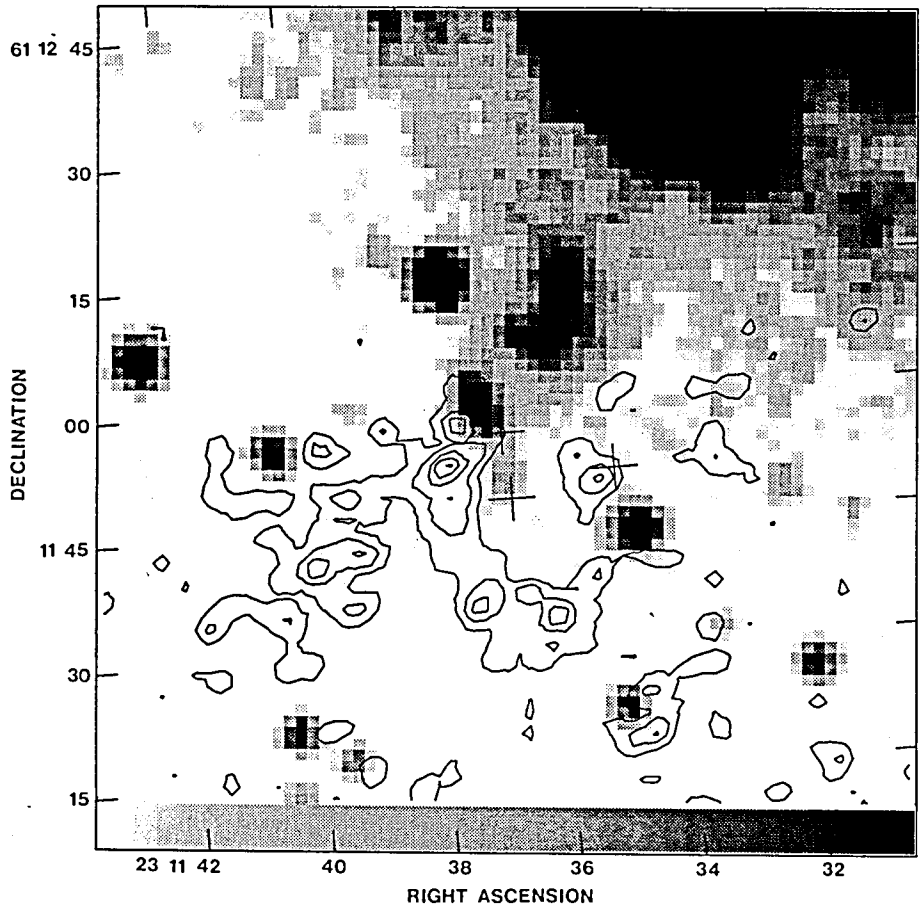

Figure 4.2 - An overlay of HCN contours on an optical image taken from the red plate of the Palomar Observatory Sky Survey. The grey scale ranges from 65 (light grey) to 300 (dark grey) flux units. The HCN contours have been summed over a velocity interval between -57.0 km/s and -58.0 km/s. The contours levels are at 1.875, 2.625, 3.375, 4.125, and 4.875 Jy/beam. The positions of IRS 1, IRS 2, and IRS 3 are indicated by the three crosses.

north of the molecular gas is the visible H II region. The positions of IRS 1, IRS 2 and IRS 3 are marked by crosses. The figure shows the anticorrelation between the optical emission and the high density material around IRS 1 and IRS 2. Since HCN traces high densities, the lack of emission around the infrared sources can be interpreted as a lack of high density material in that region. This interpretation provides an upper bound for the density in the cavity. Figure 4.2 also indicates that the optical emission appears to reach into this cavity, which provides support for the interpretation of low densities in the cavity. The HCN emission which surrounds the cavity forms a density enhancement that has a clumpy appearance. This density enhancement seems to outline the interface between the expanding H II region and the molecular cloud. The expansion of the H II region or a stellar wind from the young star could be pushing the molecular material aside thus resulting in a cavity depleted of high density material. If such an expansion takes place in a clumpy molecular cloud, the material pushed aside (which is found at the interface) retains the uneven density structure of the original cloud.

Figure 4.3 is a comparison of the HCO^+ and HCN emission around IRS 1. The grey scale corresponds to the HCO^+ emission and the contours correspond to the HCN emission. Both the maps are sums integrated over the velocity interval -58.0 km s^{-1} < V_{LSR} < -57.0 km s^{-1}. The HCO^+ emission, which has a peak value of 6.5 Jy/beam, is not significantly stronger (within calibration errors) than the HCN emission, which has a peak value 5 Jy/beam. However, the strongest HCN

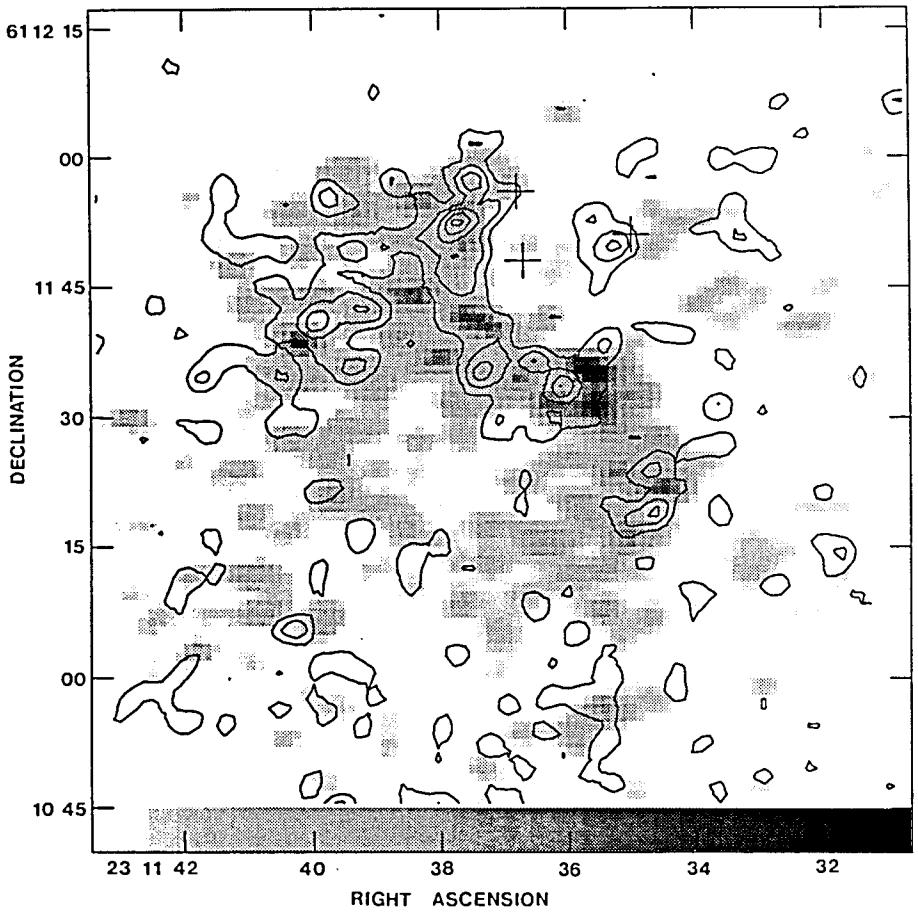

Figure 4.3 - Integrated HCN contours overlaid on an integrated grey scale map of HCO^+ emission. Both the maps are sums integrated over the velocity interval -58.0 km s^{-1} < V_{LSR} < -57.0 km s^{-1}. The grey scale covers a flux range from 1.875 Jy/beam (light grey) to 6.5 Jy/beam (dark grey). The HCN contours are at intervals of 1.875, 2.625, 3.375, 4.125, and 4.875 Jy/beam. The three crosses indicate the positions of IRS 1, IRS 2, and IRS 3.

peak is situated to the northeast of IRS 1 while the strongest HCO^+ peak is to the southwest of IRS 1. Both the molecules trace clumps around the infrared sources. These clumps are strung around the H II regions and clearly outline the cavity in the molecular cloud. The fact that the cavity is also seen in the HCO^+ emission provides strong evidence for the interpretation of low densities in the cavity since HCO^+ traces densities $> 10^5$ cm^{-3} (§1.4). The high resolution maps indicate that the cavity has a diameter of about 0.09 pc ($\sim 2 \times 10^{17}$ cm at a distance of 3.5 kpc) and extends to the south of IRS 1.

Although the HCO^+ emission follows the HCN emission rather closely in the general structure of the emission, a detailed comparison of the positions of the individual peaks of the HCN and the HCO^+ emission shows no correlation. Such an anticorrelation has been seen before in Orion, by Vogel et al. (1984). The beamsize in their maps is about 18", but since Orion is about 6 times closer than NGC 7538, their absolute scale is roughly the same as the scale of the maps presented here. The explanation offered by Vogel et al. (1984) for the observed difference is that the HCO^+ and the HCN emission arise from different but adjacent parts of the molecular cloud. In the case of NGC 7538 IRS 1, a possible explanation could be that a shock front or an ionization front from the HII region is expanding into the clumpy molecular cloud. This, in turn, could cause high ionization levels in the clumps it hits first, ultimately resulting in the HCO^+ emission (de Jong et al. 1975). The neutral clumps would then show the HCN emission. Such an explanation assumes that both the HCN and HCO^+

transitions are optically thin. This explanation is further supported by the fact that the HCN clumps are, in general, smaller than the HCO^+ clumps (as is discussed later) and thus could be a probe of the dense cores of the clumps.

The interpretation of low densities in the region around IRS 1 can be tested by looking at the emission in this region from a molecular transition that thermalizes at lower densities. The J=1-0 transition of ^{13}CO thermalizes at densities of ~2 x 10^3 cm^{-3}. So if the lack of HCN and HCO^+ emission around IRS 1 is indeed due to lack of high density material, there should be no evidence of the cavity in the ^{13}CO maps. In fact, the maps (Figure 3.9) do not show a lack of ^{13}CO emission in that region, at any velocity. We have discussed at the beginning of the section that the ^{13}CO emission in the source is optically thin and the optical depths provide a lower bound for the densities in the region of ~ 2 x 10^3 cm^{-3}. Hence, we can conclude that the presence of ^{13}CO emission does indicate that the densities in the cavity are low. Figure 4.4 is a comparison of the HCN, HCO^+, and ^{13}CO spectra around IRS 1. The position of IRS 1 is at $\alpha(1950) = 23^h11^m36^s.7$; $\delta(1950) = 61°11'48"$. The spectra show clearly the lack of HCN emission in the region around IRS 1 (Figure 4.4a). The HCO^+ emission is present but it is very weak (Figure 4.4b). Also, the center velocity of the HCO^+ emission is at -60.0 km s^{-1} which is blue shifted with respect to the quiescent velocity of -58.0 km s^{-1}. This indicates that the emission is in fact from the high velocity outflow which has been seen in HCO^+ and CO (§4.4). This would imply

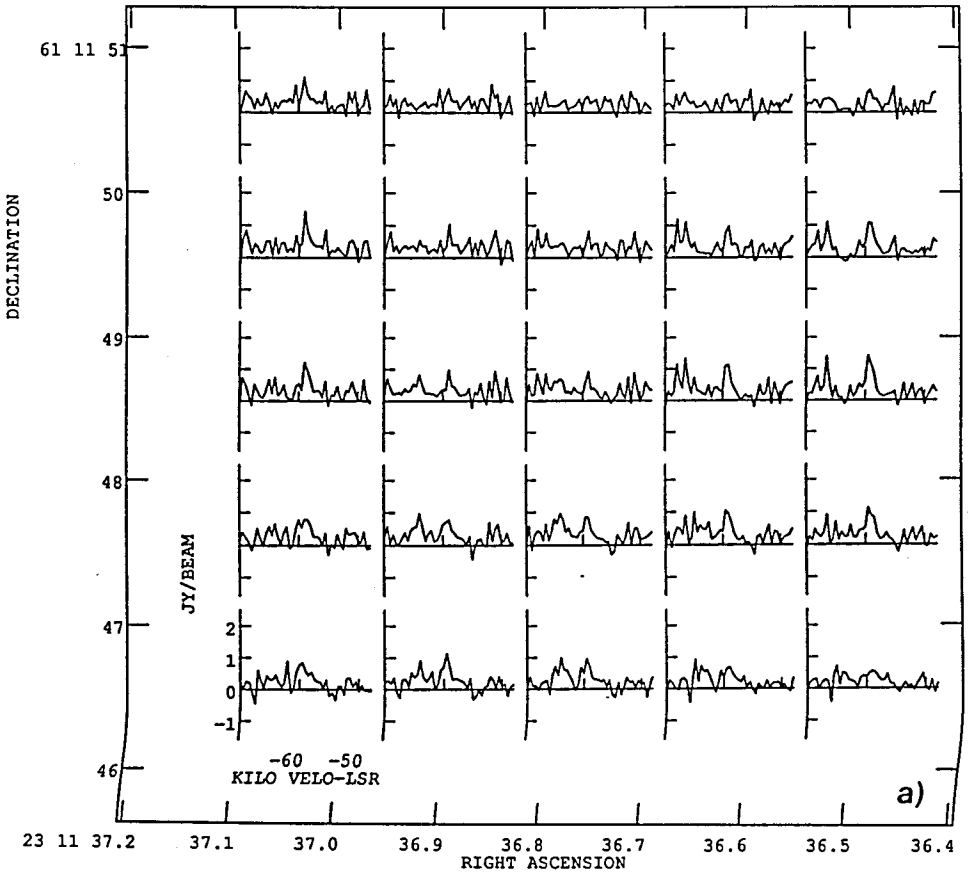

Figure 4.4 - a) Raster of HCN (J=1-0) spectra around IRS 1. The IRS 1 position is approximately at $\alpha(1950) = 23^h11^m36^s.7$, $\delta(1950) = 61°11'48"$. The intensity scale and the range of velocities is given in the spectrum at the lower left hand corner.

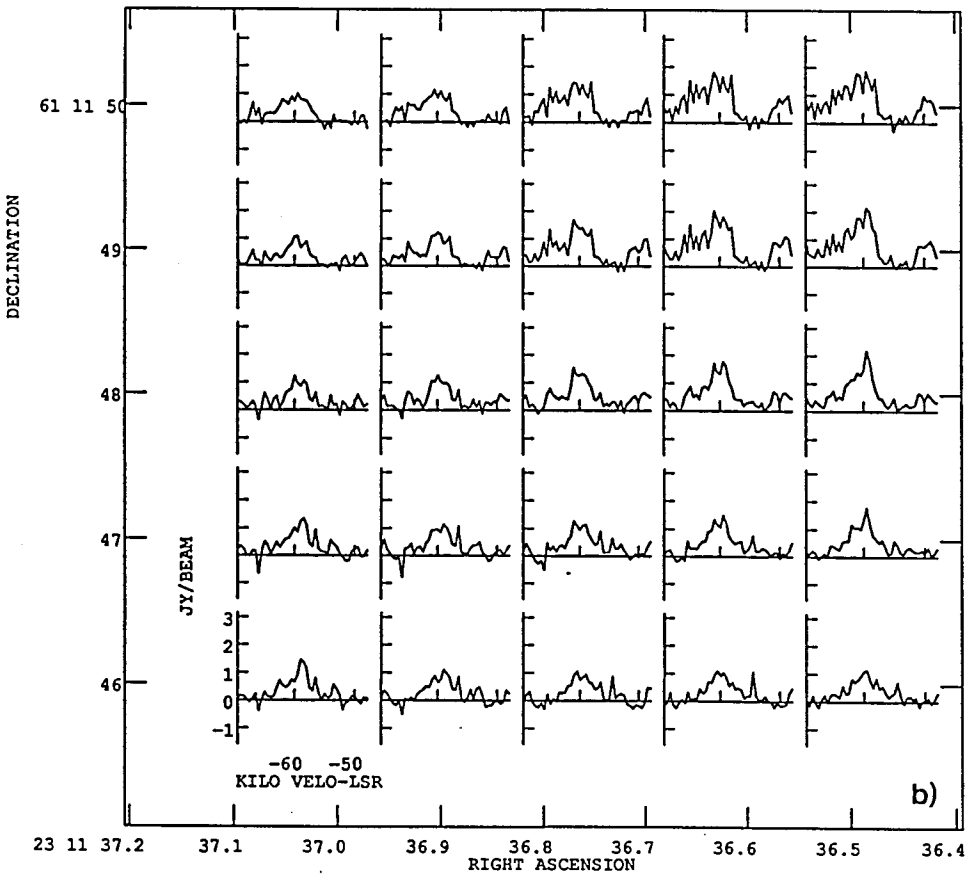

Figure 4.4 (cont.) - b) Raster of HCO^+ (J=1-0) spectra in the same region around IRS 1 as shown in Figure 4.4a. The intensity and velocity scales are shown in the spectrum in the lower left hand corner.

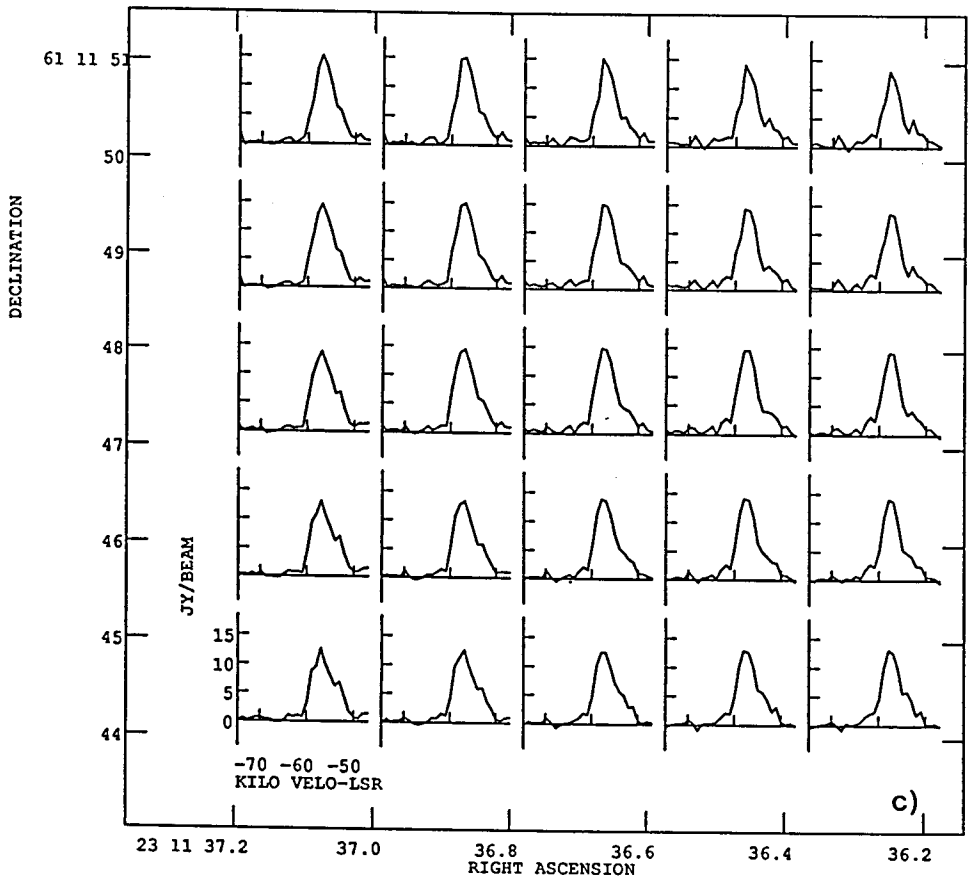

Figure 4.4 (cont.) - c) Raster of ^{13}CO (J=1-0) spectra around the same region around IRS 1 as shown in Figure 4.4a and 4.4b. The velocity resolution in the spectra is lower than that in HCN and HCO^+ spectra by a factor of 2.

that the HCO^+ gas is in front of IRS 1 and has a component of motion out from the source. The outflow can be seen in Figure 3.7 which shows the emission shift as the velocity becomes more negative. However, as seen in Figure 4.3, the emission at the quiescent velocity (-57.0 to -58.0 km s^{-1}) does not peak at the IRS 1 position.

Figure 4.4c shows the ^{13}CO spectra in this region, which clearly indicates that the cavity seen in the HCN maps is due to low density material around the H II region. The peak of the ^{13}CO lines is between 10 and 15 Jy/beam while the strongest HCO^+ emission in this region is between 1 and 2 Jy/beam, and the HCN emission is less than 1 Jy/beam. These spectra provide support for the interpretation that the densities in the region around IRS 1 are of the order of 10^4 cm^{-3}.

§4.2 Continuum Spectrum of IRS 1

The dashed contours in Figure 4.1a outline the low resolution 3.3 mm continuum map. The map shows an unresolved source with a peak value of 1.1 Jy at the position of IRS 1 and a weak northward extension toward IRS 2. Figure 3.11a shows the high resolution continuum map at 3.3 mm. The emission still appears to be unresolved and so the peak flux of 1.06 Jy/beam can be taken as the total flux from IRS 1 at this wavelength. Figure 3.11b shows a similar continuum map at 2.7 mm with a peak value of 0.996 Jy/beam. These continuum values can be considered along with the measurements of IRS 1 fluxes which are tabulated in Table 2.2. The continuum spectrum of IRS 1 was plotted in

Figure 2.3. The previous measurement at 2.7 mm (Scoville et al. 1986) is more than a factor of 2 higher than the value expected from the spectrum calculated from the 15 and 23 GHz flux values (Henkel, Wilson, and Johnston 1984). This is the spectrum plotted in Figure 2.3. The turnover frequency in this model was found to be 20 GHz. Although the model fits the fluxes at centimeter wavelength very well, the millimeter data suggest a rising spectrum. Observationally, one can consider this model in terms of the Boland and de Jong model for the excitation of the H_2CO maser (§1.5.3). Their model predicts that the 2 cm H_2CO transition should be observed in maser emission for high millimeter fluxes. However, this has not been observed, and Martin-Pintado et al. (1985) report only stringent upper limits on the 2 cm emission. In addition, the Boland and de Jong model requires the H II region to be optically thin at millimeter wavelengths to provide the pumping photons for the maser excitation. A better fit to the observed values that satisfies all the observational constraints can be obtained by invoking a two component model for the H II region - a hot, dense, compact component which is optically thick at millimeter wavelengths and a cooler, less dense and more extended component which is transparent to the millimeter photons.

Evidence for both the components can be found from centimeter observations. The most convincing fact is the difference in geometry between the 4.8 and 15 GHz continuum emission. Figure 2.2a shows the 15 GHz continuum map made with a 0".1 resolution by Campbell (1984a). The peak of this map is contained in the two-lobed emission centered

on IRS 1. The elongated structure suggests a bipolar flow of ionized material. To the south of the central peak indications of a weak spherical extension of the emission can be seen, while to the north an extension is not as well defined. In contrast the 4.8 GHz maps of Dickel et al. (1982) and Campbell (1984a - Figure 2.2b) display a spherical region of radius 0".5 which is centered 0".5 south of IRS 1 and features a weak extension to the north. In the proposed two-component model for the H II region the 15 GHz emission outlines the hot compact component while the 4.8 GHz emission depicts the cooler and slightly extended component. The southern, extended component might be created when the bipolar flow is confined by the high density molecular material to the south of IRS 1 to a region of radius 0".5 or $\sim 2 \times 10^{16}$ cm, the center of which is coincident in position with the dominant source of the 4.8 GHz continuum peak. To the north, the ionized flow escapes the confinement of the dense material and runs into the visible H II region. Evidence of this is seen from the observations of shock excited emission from the vibrationally excited levels of molecular hydrogen, which is illustrated by the cross-hatched region in Figure 4.1a.

In order to calculate the parameters of the extended component, it is assumed that the 4.8 GHz emission is optically thick. Then the electron temperature can be calculated from equation 1.17 for $\nu \ll \nu_c$. The distance to the source is assumed to be 3.5 kpc. The source size of the extended component is taken to be 0".5 (from Dickel et al. 1982). The equations from Olnon (1975; §1.3) for a spherical H II

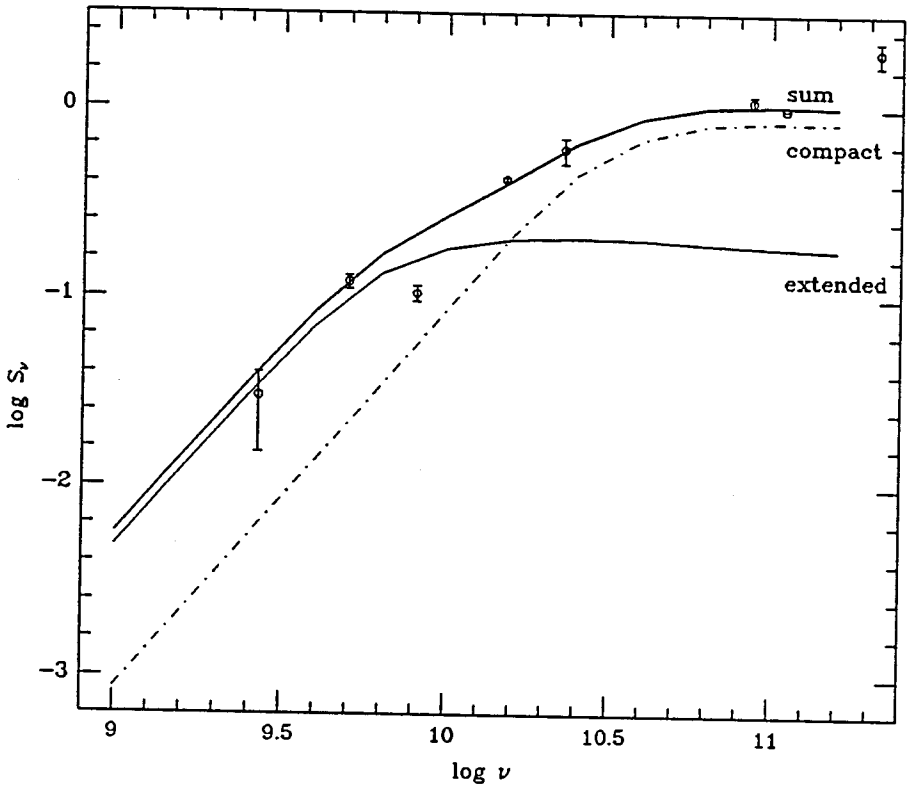

Figure 4.5 - Model H II region spectra for the compact (dot-dashed line) and extended (solid line) components associated with IRS 1. The compact component has an electron density of 2.7 x 10^6 cm^{-3} and an electron temperature of 2.7 x 10^4 K. The extended component has an electron density of 1.1 x 10^5 cm^{-3} and an electron temperature of 8.5 x 10^3 K. The other solid line is the sum of the model spectra. The points are the observed continuum fluxes (Table 2.2).

region with a constant electron density give an electron temperature, T_e, of 8500 K for this component. To calculate the electron density, the 15 GHz flux from this component is assumed to be optically thin. The fraction of the integrated flux density of the 15 GHz emission from the southern extension is found to be 0.2 Jy. These assumptions results in an electron density, n_e, of 1.1×10^5 cm^{-3} and an emission measure of 2.2×10^8 cm^{-6} pc. The turnover wavelength (corresponding to ν_c) is found to be 3.7 cm for the extended component.

The parameters of the compact component are calculated by assuming that the 15 GHz emission from this component is optically thick. The fraction of the 15 GHz flux density from the compact component is 0.19 Jy and the source size is taken to be 0".12 (Campbell 1984a). Using this value in equation 1.17 gives an electron temperature of 2.7×10^4 K. For the optically thin part, the 88 GHz flux is used. The fraction of the 88 GHz flux contributing to the extended component is found to be 0.19 Jy (from the calculated spectrum for the extended component). This implies that the flux density contribution to the compact component is 0.92 Jy. These values give an electron density of 2.7×10^6 cm^{-3}, an emission measure of 3×10^{10} cm^{-6} pc and a turnover wavelength of 0.72 cm. The resulting spectra are plotted in Figure 4.5. The points are the actual observed flux densities. The solid line is the sum of the theoretical spectra for the compact and the extended component. The model seems to fit the observed values quite well. The parameters calculated from the model are mostly upper limits, especially for the fluxes at the millimeter wavelengths, since the

dust contribution to the flux densities has not been taken into account.

The flux densities at 88 GHz and 110 GHz have been measured at Hat Creek. The 110 GHz flux density is not as strong as that measured by Scoville et al. (1986). In fact, our measured values at 88 GHz and 110 GHz give a spectral index of about -0.3. These values are much closer to a typical, optically thin H II region and they remove the need to assume a stellar wind H II region model to explain a rising spectrum. The flux density at 1 mm also agrees with this model. The excess emission from the free-free value can be taken to be a contribution from optically thin dust grains. The observed flux density can be used to estimate the mass of gas and dust in the source. In the optically thin limit the observed flux density can be related to the associated mass by

$$M = \frac{S_\nu d^2 \mu_G m_{H_2}}{B_\nu(T_d)[\tau_d/N_{H_2}]}, \qquad (4.2)$$

where T_d and τ_d are the temperature and opacity of the dust, $\mu_G = 1.36$ is the mean atomic weight of the gas, d is the diameter of the source, S_ν is the flux density, B_ν is the blackbody intensity, and N_{H_2} is the column density. To extrapolate the ratio of the dust opacity to the hydrogen column density to millimeter wavelengths (Scovile et al. 1986 and references therein) use

$$[N_{H_2}/\tau_d] = 3.75 \times 10^{25}\ \lambda_{mm}\ cm^{-2}. \qquad (4.3)$$

The mass can then be written as

$$M = 19.6 S_\nu\ \lambda_{mm}{}^5 [\exp(14.4/\lambda_{mm} T_d)-1] d_{kpc}{}^2 M_\odot\ , \qquad (4.4)$$

where S_ν is in Janskys. For an excess of 2.1 Jy at 1 mm, the resulting mass of gas and dust is about 180 $M_\odot$.

§4.3 Implications of Molecular Results on Maser Models

Figure 4.1b shows the positions of all the masers around IRS 1. The explanation for the symbols in the figure is in Table 2.4. All the masers appear to be associated with the southern, circular component of the H II region. The typical H_2 densities for inverting the OH maser lines with collisions are of the order of 10^7 cm^{-3}. Such densities can be achieved in dense shells around H II regions (Elitzur and de Jong 1978). The figure shows that the OH masers around IRS 1 appear to be around the edge of the ionized region, which is consistent with the above model.

The H_2CO masers, however, need lower densities for inversion since densities $\geq 3 \times 10^5$ cm^{-3} quench the maser. According to the Boland and de Jong model (§1.5c), the H_2CO maser is inverted by free-free emission from the H II region and the inversion requires densities of $\approx 3 \times 10^4$ cm^{-3}. The cavity in the HCN and HCO^+ emission sets an upper

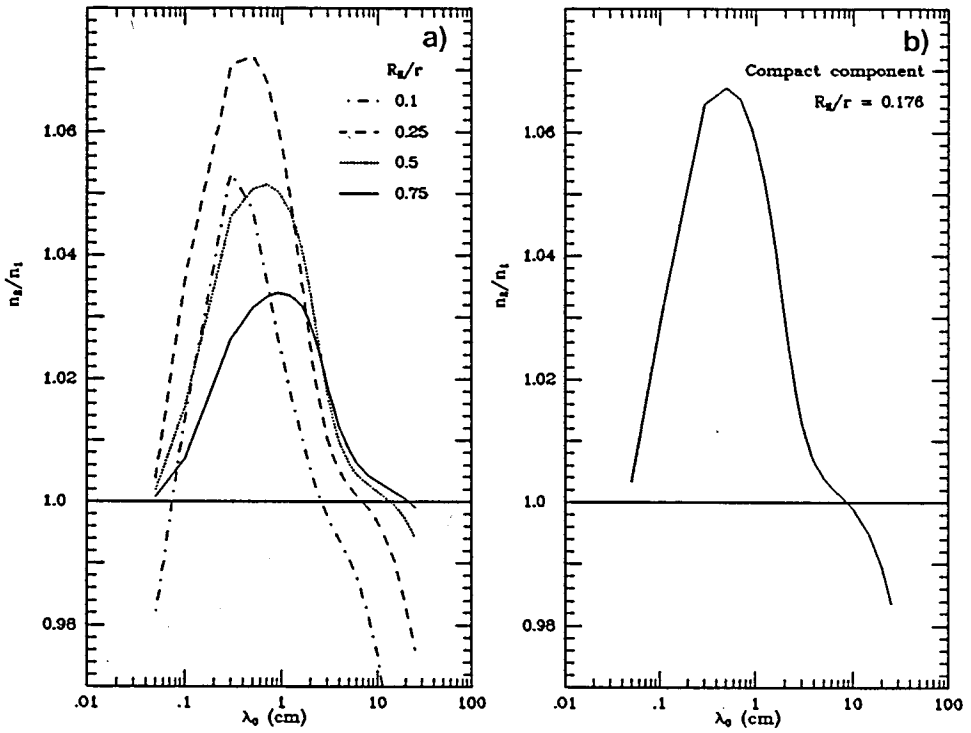

Figure 4.6 - a) Population ratios in the ground state doublet of the 14-level H_2CO system plotted against turnover wavelength. The ratios are plotted for the parameters of the extended component of IRS 1 for various values of R_{II}/r (where r is the distance of the inversion layer and R_{II} = 0.0085 pc). b) Population ratio in the ground state doublet of H_2CO plotted against λ_0 for the parameters of the compact component. The curve is plotted for the value of R_{II}/r for which the extended component gives the maximum inversion at λ_0 = 3.7 cm. The radius of the compact component is 0.002 pc.

limit to the densities in the region around IRS 1 since the densities at which these transitions are thermalized is $> 10^5$ cm^{-3}, which indicates that the H_2CO emission must be originating in the region in the molecular cloud where no HCN and HCO^+ emission is seen. Since ^{13}CO thermalizes at densities of the order of 2×10^3 cm^{-3}, the H_2 density in the cavity must be in the range between 10^3 and 10^5 cm^{-3}. This condition is in agreement with the stringent requirement set by the Boland and de Jong model for the inversion of the H_2CO maser line. The different H_2 densities required for the excitation of the various masers seen around IRS 1 can be explained if one considers the expansion of the H II region into a clumpy molecular cloud. The clumpy nature of the cloud is retained, thus creating a range of H_2 densities that provide the varied conditions for the different masers.

The continuum spectrum of IRS 1 provides the parameters required for the H_2CO maser models. The Boland and de Jong model requires that the H II region be optically thin at millimeter wavelengths and compact with emission measures between 10^8 - 10^{10} cm^{-6} pc. The H_2CO maser observed toward IRS 1 seems to be associated with the extended, southern component of the two-component model described in §4.2. This component is compact with an emission measure of 2.2×10^8 cm^{-6} pc, which is in the range required by the model. The turnover frequency, ν_0, is found to be 8 GHz (λ_0 = 3.7 cm), which is in the required range of 10 GHz< ν_0 <3 GHz for only the 1_{10}-1_{11} transition to be inverted.

The model is now examined for the specific conditions calculated for the two component model. The maser spots have been observed toward

the extended, southern component of IRS 1 (Rots et al. 1981). Figure 4.6a and 4.6b show the results of a calculation for the 14-level H_2CO molecule. The calculations use the equations from the Boland and de Jong model. Collisions and radiative trapping have been ignored. Including collisions would tend to narrow the range of λ_0 over which the transition is inverted. For the extended component (Figure 4.6a) the maximum inversion (n_2/n_1) is obtained for $R_{II}/r = 0.25$. Reducing R_{II}/r (which moves the masing gas farther out from the H II region) shifts the maximum inversion to lower turnover wavelengths (more compact H II regions). But the turnover wavelength of the extended component is 3.7 cm. The ratio R_{II}/r is 0.75 for the greatest inversion at 3.7 cm (solid curve in Figure 4.6a). This implies that the masing gas is at a distance of 0.011 pc from the center of the H II region if the radius of the extended component is taken to be 0.0085 pc (0".5 at 3.5 kpc). The inversion curve for the compact component has also been calculated (Figure 4.6b) for r = 0.011 pc. This gives a ratio R_{II}/r of 0.176 (R_{II} = 0.002 pc for the compact component). The inversion for the compact component is higher than that for the extended component. In fact, the peak inversion for the compact component is at about 0.7 cm, which is the turnover wavelength found for that component of the H II region.

The relative abundance of formaldehyde required to produce the observed maser brightness temperature can now be calculated for the parameters obtained from our data and compared to the Boland and de Jong model. The brightness temperature of the H_2CO line is given by

$$T_b = T_c \{\exp(-\tau) - 1\}, \qquad (4.5)$$

resulting in an optical depth of

$$\tau = 3.4 \times 10^{-8} \eta n(H_2CO)\Delta l/v_{th} \ . \qquad (4.6)$$

Here τ is the optical depth of the 6 cm H_2CO line, Δl is the thickness of the inversion layer, $v_{th} = 0.1$ km s^{-1} is the thermal velocity of H_2CO molecules and η is $(1-n_2/n_1)$. The observed brightness temperature of the maser is 10^6 K and the brightness temperature of the radio continuum radiation from the H II region, T_c, is found to be 8.5×10^3 K. Using these values, the optical depth required to produce the observed maser emission is about -5. For $R_{II}/r = 0.75$ ($\Delta l = 1.33$ R_{II}), the inversion at $\lambda_0 = 3.7$ cm is found to be 1.0137. With these parameters and an H_2 density of 10^4 cm^{-3}, the abundance of H_2CO relative to H_2 is found to be 4×10^{-7} in order to get the required optical depth. This is half the value that is found by Boland and de Jong. However, our value is consistent with the values predicted by models of molecular cloud chemistry (de Jong et al. 1980).

Following the discussion in Boland and de Jong (1981), the scheme for H_2CO formation is initiated by the radiative association reaction

$$C^+ + H_2 \rightarrow CH_2^+ + h\nu, \qquad (4.7)$$

which leads to CH_3^+ after collisions with H_2. At large densities

($n(H_2) > 10^4$ cm^{-3}) CH_3^+ is removed from the gas by

$$CH_3^+ + H_2 \rightarrow CH_5^+ + h\nu, \qquad (4.8)$$

rather than by recombinations. CH_5^+ is mainly destroyed by dissociative recombinations, which leads to the production of CH_3 and CH_4. CH_3 is destroyed by collisions with C^+ and H_3^+ and by the reaction

$$CH_3 + O \rightarrow H_2CO + H. \qquad (4.9)$$

It is assumed that H_2CO is removed from the gas by collisions with HCO^+, H_3^+, and C^+. At large densities, the formation of C^+ is initiated by cosmic ray ionization of He atoms followed by the reaction

$$He^+ + CO \rightarrow C^+ + O + He. \qquad (4.10)$$

The C^+ ions are mostly destroyed by reaction 4.7. The model calculations of de Jong et al. (1980) find that in dense dark clouds all the hydrogen is in H_2, all the carbon is in CO and about two-thirds of the oxygen is in O_2. Assuming that electrons are mainly produced by cosmic ray ionization of H_2 and removed from the gas by dissociative recombination with molecular ions like HCO^+ and H_3^+, Boland and de Jong (1981) find that the electron density for a gas temperature of 20 K and a cosmic ray ionization rate of H_2, ζ, is given by

$$n(e) = 1.6 \times 10^{-4} \left(\frac{\zeta}{5 \times 10^{-8}\ s^{-1}}\right)^{1/2} \left(\frac{n(H_2)}{10^4\ cm^{-3}}\right)^{1/2}. \quad (4.11)$$

Using a H_2CO destruction rate due to collisions with molecular ions of $2 \times 10^{-9}\ n(e)\ s^{-1}$, the formaldehyde abundance relative to hydrogen can be written as

$$\frac{n(H_2CO)}{n(H_2)} = 8 \times 10^{-7} \left(\frac{\zeta}{5 \times 10^{-18}\ s^{-1}}\right)^{1/2} \left(\frac{10^4\ cm^{-3}}{n(H_2)}\right)^{1/2}. \quad (4.12)$$

The parameter ζ is the cosmic ray ionization rate of H_2 and the equation is valid for a gas temperature, T_K, of 20K. The value assumed for ζ can account for the difference between the value calculated by Boland and de Jong and our value. It appears from the above discussion and our results that the Boland and de Jong model is satisfactory in explaining the H_2CO maser emission in NGC 7538.

The molecular data presented here can also provide useful inputs to OH maser models. The data do not show the presence of a high density close to the H II region where the OH masers are presumed to form. It is possible that such a shell may be too thin and hence escapes detection. It is also possible that the OH masers are in fact formed in the molecular cloud in front of the H II region and are seen in projection against the H II region. The clumpy nature of the cloud can provide the high densities required by the OH maser models.

The H_2O maser in IRS 1 is seen to be offset from the H II region

and could also be forming in the molecular cloud. The high density enhancement surrounding the cavity around IRS 1 provides support for this interpretation and could be the site of the maser formation.

§4.4 The High Velocity Outflow

The low resolution HCO^+ results (§3.4) show the broad line wings that indicate the presence of a high velocity outflow in the source. The outflow in this source has been detected in the line wings of the J=1-0 transition of CO (§2.3). The dotted regions in Figure 4.1a outline the red (southeast) and the blue (northwest) lobes of the high velocity CO emission (Scoville et al. 1986). The outflow is oriented at a position angle of 145°. The orientation of the HCO^+ emission agrees very well with that of the CO outflow. Since HCO^+ thermalizes at densities that are about two orders of magnitude higher that CO, the HCO^+ emission must be sampling molecular material that forms the high density component of the outflow. This material could also be closer to the source of the outflow.

The two main structures seen in the low resolution HCO^+ results are seen in Figure 3.7a. The symmetric double-lobed feature seen at -57.1 km s^{-1} is highly elongated and is oriented at a P.A. of 52°. Figure 3.7b shows the spectra along this feature. The line peaks toward the center of this structure are shifted toward more negative velocities. In addition, the spectra toward the center show symmetric,broad line wings extending about 10 km s^{-1}. At positive

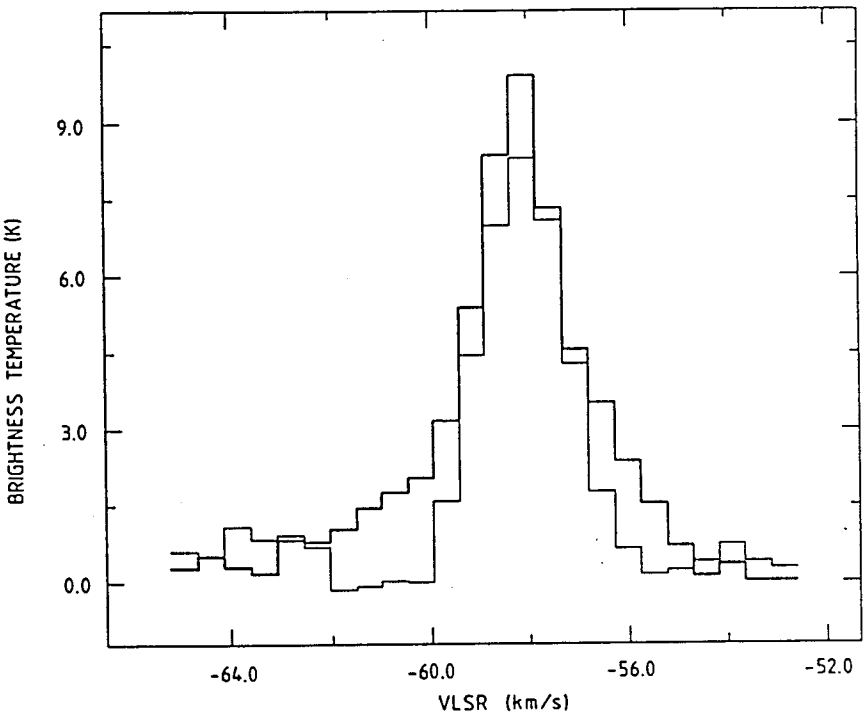

Figure 4.7 - Overlay of the spectrum at offset 20 (thin line) and offset 5 in figure 3.7b. The spectrum at offset 20 was shifted by one channel to the left so that the channel of the peak intensities agree. Note the broad symmetric line wings at offset 5.

offsets (northeast) the line wings disappear and the profiles are gaussian, peaking at a V_{LSR} of -57.58 km s^{-1} and with a FWHM of 1.96 km s^{-1}. Figure 4.7 shows this difference in line shape where the spectrum at offset 20 (shifted by one channel - thin line) is overlaid on the spectrum at offset 5 (thick line). Toward the negative offsets (Figure 3.7b - southwest), the line peaks shift to higher velocities and the line profiles display extended redshifted line wings.

Figure 3.7a also shows an elongated structure, perpendicular to the one described above, which corresponds to the emission at -59.7 km s^{-1}. This structure is at the same position angle as the orientation of the outflow seen in CO. The structure has a strong peak to the northwest that is three times stronger than the peak to the southwest. Spectra along this feature are shown in Figure 3.7c. The spectra at the central positions have symmetric, broad line wings consistent with the spectra at the center of the previously described structure. At positive offsets the line emission is weak and peaks at slightly lower velocities. Toward negative offsets the peaks of the profiles shift to progressively lower velocities and show extremely asymmetric blue shifted line wings.

The high resolution maps (Figure 3.8) show the same elongated structure at high velocities although the emission breaks up into clumps. The dark contours in Figure 3.8 show the high resolution maps convolved to match the resolution of the low resolution maps. The channel maps show that at the map corresponding to a velocity of -57.5 km s^{-1}, the clumps appear to be distributed preferentially in the

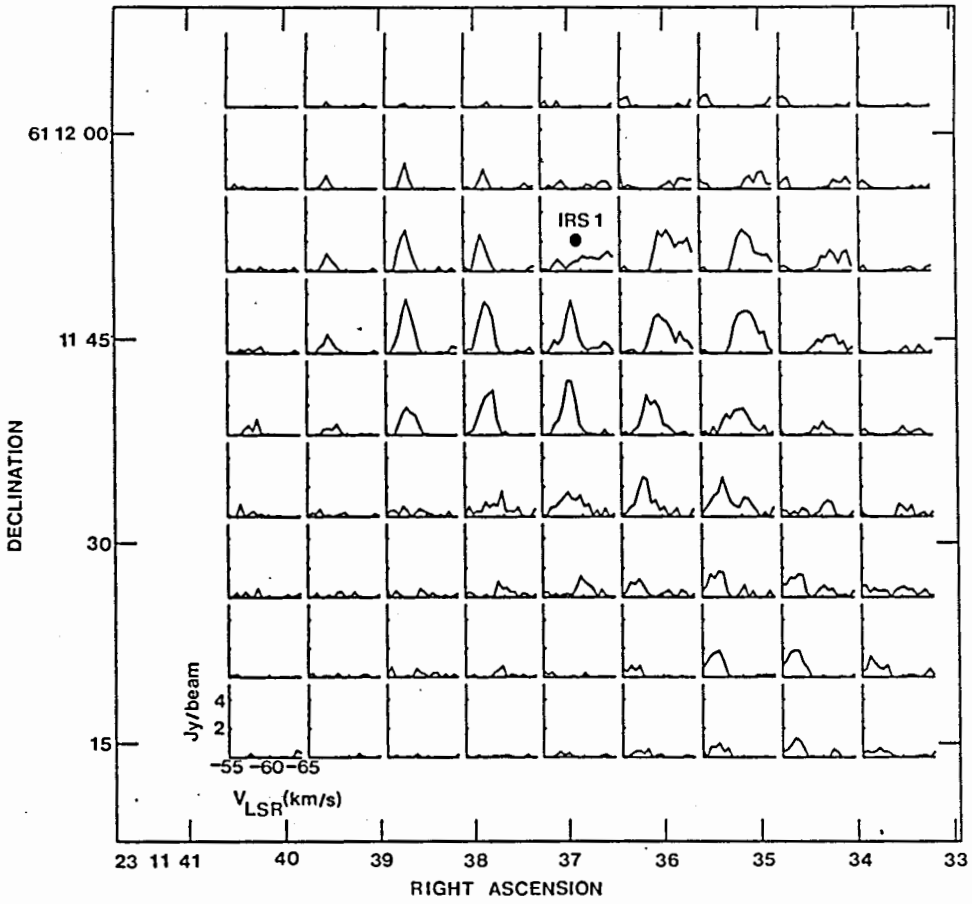

Figure 4.8 - A raster of HCO^+ spectra showing the elongated emission structure stretching from the northeast to the southwest and the blue shifted outflow toward the northwest. The approximate position of IRS 1 is marked by the filled circle. The spectrum in the lower left hand corner shows the velocity and intensity scales. It is evident that the peak of the spectra along the elongated structure is greater than -60.0 km s^{-1} while the position of the peak to the northwest (at about $\alpha(1950) = 23^h11^m35^s$ and $\delta(1950) = 61°11'45"$) is shifted to more negative velocities.

elongated structure. At a velocity of -58.5 km s^{-1} the clumps appear to have moved to the center of the structure. This position shift implies that the clumps near the center of the structure have lower velocities than the clumps at the edges of the elongated structure. At velocities of -58.0 km s^{-1} and -58.5 km s^{-1}, which are around the quiescent velocity of the source, the strongest emission peaks appear most prominently to the south and southeast of the H II region. At lower velocities, starting at a velocity of -59 km s^{-1}, the clumps separate into two groups northwest and southeast of IRS 1. A group of clumps in a direction perpendicular to the elongated structure can be seen in the maps corresponding to -59.5 and -60.0 km s^{-1}. It is this group of clumps that shows up in the low resolution maps as a blue component of the outflow.

The presence of the outflow and the velocity structure of the source can be seen in Figure 4.8, which is a raster of HCO^+ spectra around IRS 1. The velocity and intensity scale are shown in the lower left hand corner. The spectra trace the elongated structure that was seen in the channel maps. There appears to be some velocity shift in the line peaks going from the southwest to the northeast along the elongated structure. The emission toward the southeast end of the structure appears to peak toward higher velocities than those toward the northwest lobe. To the northwest, the blue lobe of the outflow is clearly seen. The line peak shifts toward more negative velocities. There is no clear evidence for a red component of the outflow.

The outflow in this source has been studied in the J=1-0

transition of CO by several authors. The studies have found that the outflow is oriented at a position angle of 145° with a separation of 44" between the red and blue lobes. On small scales, the continuum map at 15 GHz, made with a resolution of 0".1, shows evidence for an ionized outflow in the north-south direction. If the outflow, seen in CO, originates from IRS 1, then there should be some mechanism that changes the orientation of the outflow from small scales to large scales. Kameya et al. (1989) provide an explanation for this phenomenon by invoking density enhancements to the northeast and southwest of IRS 1. The HCO^+ maps, which have been presented here, have a resolution of about 3". The maps show that the orientation of the HCO^+ outflow is the same as that of the CO outflow. However, the origin of the outflow is definitely to the south of IRS 1, which can be seen in the HCO^+ channel maps (Figure 3.8) corresponding to velocities of -59.0, -59.5, and -60.0 km s^{-1}. In addition, the outflow appears to originate at the center of the elongated, double-lobed structure seen at a velocity of -57.5 km s^{-1} and appears to be perpendicular to this structure.

The evidence presented by the HCO^+ results points to the presence of another source as the origin of the outflow. No source has been detected toward this position in the infrared. However, the low resolution map across the J=1-0 transition of HCN shows a peak of emission to the south of IRS 1, which is situated at the center of the elongated structure (Figure 4.1). This peak of emission is also seen in the high resolution HCN maps corresponding to the velocities

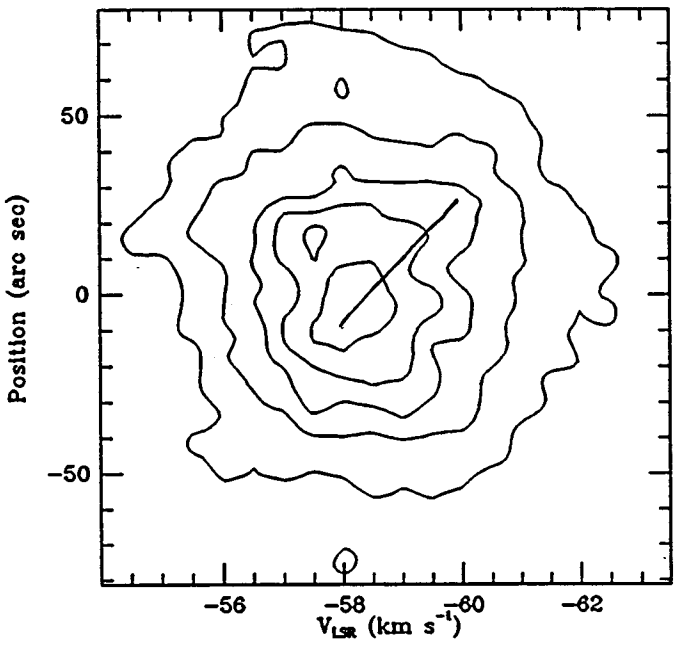

Figure 4.9 - Position - velocity cut along the low resolution HCO^+ cube. The cut is through (0,0) at a position angle of 52° which is along the elongated structure. The (0,0) position is at $\alpha(1950) = 23^h11^m37^s$, $\delta(1950) = 61°11'50"$. The solid line shows the extent of the velocity shift used in the mass calculation.

of -57.0, -57.5, -58.0, and -58.5 km s^{-1} (Figure 3.5). The high resolution HCO^+ and HCN maps point to the presence of high density clumps in the vicinity of the apparent origin of the outflow source. So the source of the outflow is either of very low luminosity or is a young star undergoing a considerable amount of extinction.

It is possible that the elongated structure seen in HCO^+ forms a disk-like structure around the outflow source. If the disk is being seen edge on, there could be enough material along the line of sight to obscure the source of the outflow. Figure 4.9 shows a position-velocity cut along the elongated structure in HCO^+. The shift in peak velocity of 2.0 km s^{-1} occurs over a spatial extent of about 30" (solid line). This gives a virial mass ($M = v^2RG$) for this structure of about 475 $M_\odot$. This mass is enough to collimate the outflow of 45 $M_\odot$ from a central source, which was measured by Scoville et al. (1986). The mass calculated from this plot is just an estimate since the velocity shift of the peak is not very well defined.

A position-velocity cut along the same position angle in the ^{13}CO maps is shown in Figure 4.10. The plot shows that the shift in peak velocity is 2.0 km s^{-1} over an extent of about 20". This gives a mass of about 320 $M_\odot$. The spatial extent of the structure is harder to define since the ^{13}CO emission is much more complex than the HCO^+ emission in velocity. This could introduce significant errors in the mass estimates. However, the mass estimates made above are similar to those made from the HCO^+ results. An estimate of the H_2 density in this structure can be made by taking an aspect ratio of 3.5:1 for the

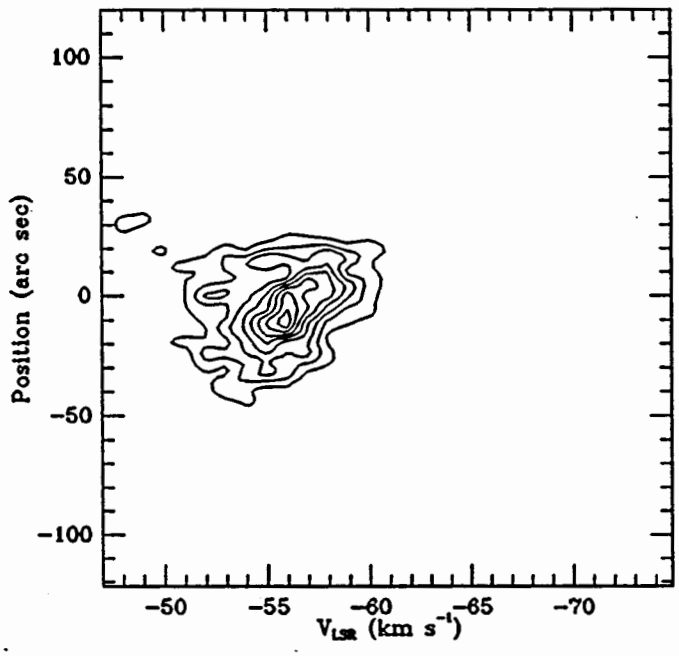

Figure 4.10 - Position - velocity cut along the ^{13}CO cube. The cut is through (x,y,P.A.) = (0,-15,52°). The (0,0) position in this cube is at $\alpha(1950) = 23^h11^m37^s$, $\delta(1950) = 61°11'50"$.

elongated structure (from the low resolution HCO^+ map - Figure 3.7a). The H_2 density is found to be about 7 x 10^5 cm^{-3} from the HCO^+ results and about 1.5 x 10^6 cm^{-3} from the ^{13}CO data, which is quite good agreement and is consistent with densities calculated from optically thin HCN emission in this region (§4.1).

Scoville et al. (1986) also see an elongated structure in their ^{13}CO maps. The structure is found to be elongated in the east-west direction with an extent of 22" and an orbital velocity of 4 km s^{-1}. Assuming a distance of 3.5 kpc to the source, a mass of about 650 $M_\odot$ is required to bind this structure gravitationally. The ^{13}CO maps presented here show a more complicated structure for the molecular cloud. The east-west peaks of emission that were seen by Scoville et al. (1986) can be seen in the channel maps corresponding to the velocities of -56.0 to -59.0 km s^{-1} (Figure 3.9). Figure 3.10a shows a position-velocity cut along this structure. It shows that the spatial extent of the structure is about 55" and the velocity extent is about 8 km s^{-1}. The shift in the peak velocity is about 2.0 km s^{-1} over a spatial extent of 20". If this structure is embedded in the molecular material, the mass required to bind such a structure gravitationally is about 160 $M_\odot$. The mass estimate made by Scoville et al. 1986) was 500 $M_\odot$ from the virial equation. They also made an alternate calculation for the mass by using the integrated line intensity, which gave a mass of 130 $M_\odot$. These estimates are comparable to the estimate of the mass of the ^{13}CO structure made from the data presented here.

The ^{13}CO data show that the east-west structure seen by Scoville

et al. (1986) is in fact embedded in an extended molecular cloud. The data do not show, conclusively, the elongated structure seen in the HCO^+ maps. But the emission is extended in the north-south direction and there is a velocity shift along the same direction as the HCO^+ structure, which is perpendicular to the direction of the outflow. The elongated structure seen in HCO^+ is massive enough to collimate the CO outflow.

Preliminary recombination line results (H42α and H66α - Gaume et al. 1990) seem to indicate that IRS 1 has a velocity of about -40.0 km s^{-1}, which would imply that the H II region is moving away from the molecular cloud at a velocity of about 18 km s^{-1}. The CO outflow has an average velocity of about -60 km s^{-1}, which is the average of the velocity extent of the red and blue lobes. If this outflow originated from IRS 1, it should have a velocity comparable to that of the H II region. The difference in velocities can be taken as additional support for the interpretation that the outflow does not originate from IRS 1. The southern source is, thus, still embedded in the molecular cloud and has a velocity comparable to the quiescent velocity of the cloud.

§4.5 Small Scale Clumps

The channel maps across the HCO^+ and the HCN lines indicate that the molecular cloud surrounding IRS 1 is very clumpy. With the large number of clumps seen in these maps it is possible to study the

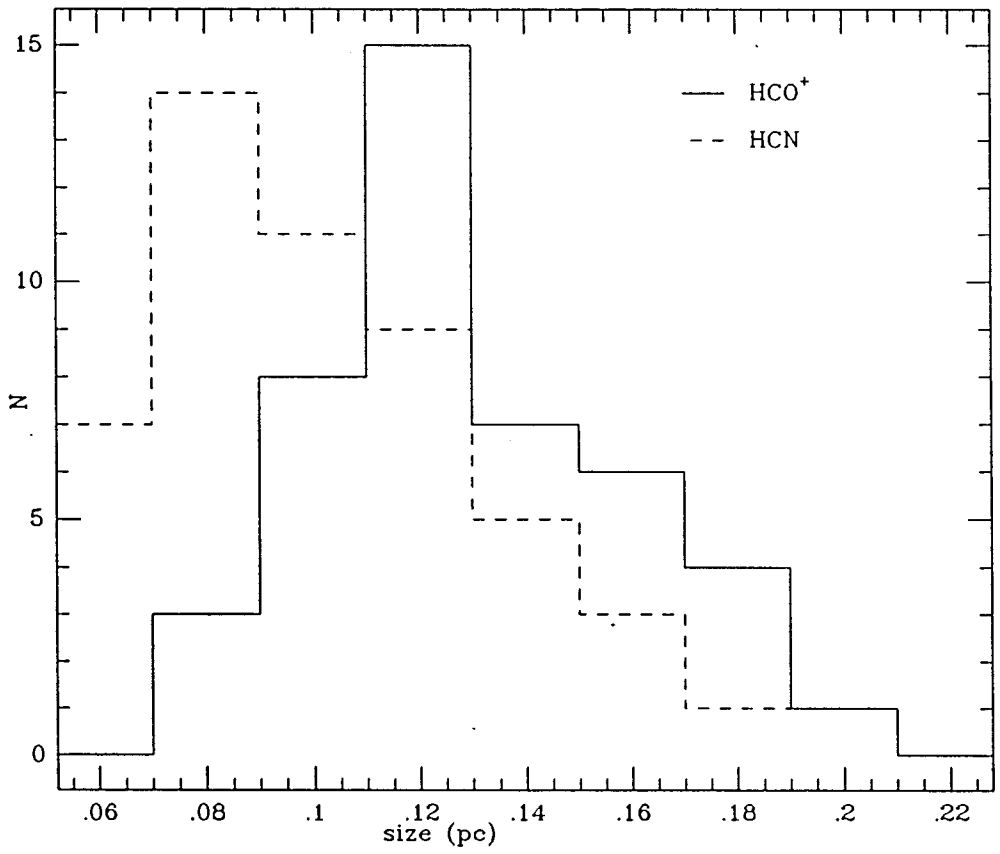

Figure 4.11 - Histograms of the HCO^+ clump sizes (solid line) and HCN clump sizes (dashed line). The sizes are in parsecs, assuming a distance of 3.5 kpc to the source.

statistical behavior of some of the clump parameters. The clumps were selected from peaks in single channel maps. The criterion for the selection was that the peak value was at least 6σ (~1.2 Jy/beam). The adjacent velocity channels were then examined and only those clumps that were seen over at least 2 velocity channels (~1.0 km s^{-1}) were taken. These criteria led to a selection of 44 clumps from the HCO^+ maps and 53 clumps from the HCN maps. The sizes of the clumps were measured by fitting two dimensional gaussians to the channel of the peak emissions in order to determine the deconvolved widths. The clump sizes used in the statistical analysis were averages of the major axis and minor axis of the fitted gaussians. The V_{LSR} and deconvolved linewidths of the clumps were measured by fitting gaussians to the spectra at the peak positions of the clumps. Figure 4.11 shows histograms of the sizes of the clumps measured in HCN (dashed line) and HCO^+ (solid line). The clump sizes are in parsecs (assuming a distance of 3.5 kpc to the source). The HCO^+ clump sizes follow a near gaussian distribution with a mean of 0.124 pc and a standard deviation of 0.028. The 95% confidence interval for the mean is between 0.115 pc and 0.133 pc. The fact that there are no HCO^+ clumps at the size of the beam (which defines the left edge of the plot) demonstrates that the HCO^+ clumps are resolved by the 3" beam. The HCN distribution does not appear gaussian and the presence of HCN clumps at the beam size indicates that there are clumps that are still unresolved. The separation between the peaks of the two distributions indicate that the HCN probes the molecular condensations which are smaller than

those sampled by HCO^+. The difference is size scales is understandable since HCN probes densities an order of magnitude higher than the densities probed by HCO^+.

The main uncertainty in the absolute values for the clump sizes lies in the uncertainty in the distance to NGC 7538. Distance estimates to the source vary from 2.8 kpc (Crampton, Georgelin, and Georgelin 1978; Campbell (1984b) to 3.5 kpc (Israel et al. 1973). The upper limit on the HCN clump sizes in the cloud thus ranges from 1.4×10^{17} cm to 1.7×10^{17} cm depending on the distance assumed for the source. Although the value assumed for the distance would cause an uncertainty in the value of the mean of the distribution, the shape of the distribution would remain unchanged.

Estimates for the masses of these dense cores can be derived from the clump sizes by assuming spheres with constant density. The density was taken to be the critical number density of hydrogen molecules at which the transition thermalized, which was 3×10^6 cm^{-3} for the HCN J=1-0 line and 2×10^5 cm^{-3} for the HCO^+ transition. The masses of the HCN clumps ranged from about 7 $M_\odot$ to 350 $M_\odot$ (assuming a distance of 3.5 kpc to the source), although most of the clumps have masses between 10 and 50 $M_\odot$. The HCO^+ clumps ranged from about 2 $M_\odot$ to 40 $M_\odot$ with most of the clumps having masses between 2 and 15 $M_\odot$. The HCO^+ clump masses are lower than HCN clump masses because the density assumed for the HCO^+ clump material is an order of magnitude lower than that assumed for the HCN clumps. If the HCN emission is optically thick ($\tau \sim 10$) this would reduce the densities and thus the mass. The

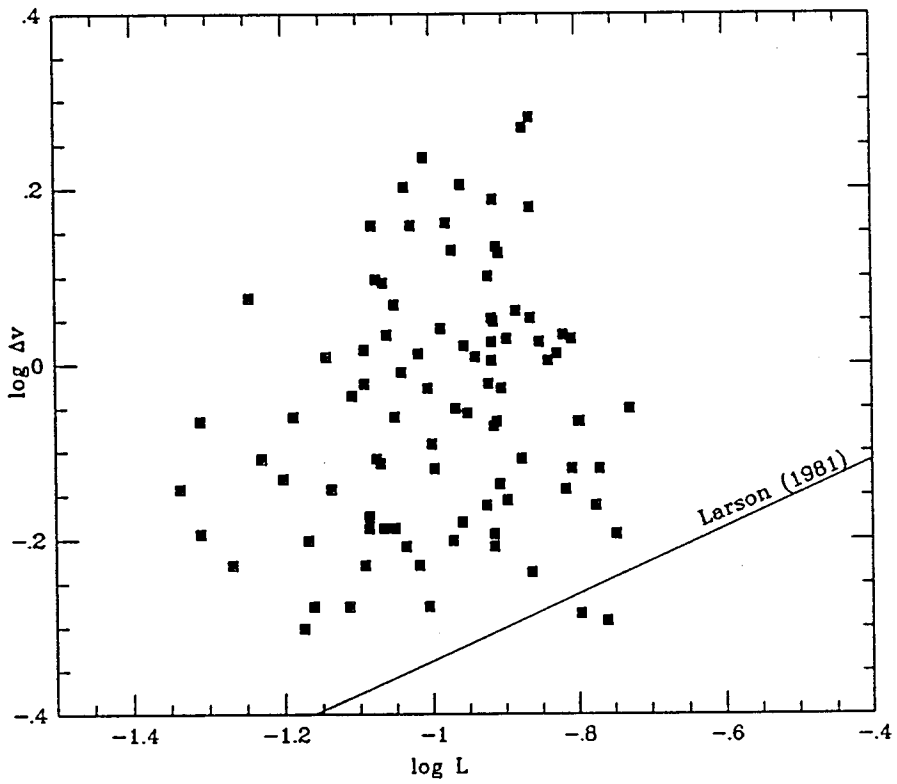

Figure 4.12 - Log L - Log Δv plot of a selection of clumps from HCN and HCO^+ data. The straight line is the correlation found from Larson (1981).

uncertainty in the distance to the source can introduce large changes in the mass estimates. For example, they are reduced by a factor of 0.6 if the smaller distance is assumed for the source. So these numbers must be taken as upper limits to the clump masses in the cloud. Nevertheless, the derived masses show that the interaction of the compact HII regions with the parent molecular cloud could lead to the formation of a cluster of low and medium mass stars.

The statistical analysis was extended to examine the data for correlations between the linewidth and the clump size. Several previous studies (Larson 1981, Leung et al. 1982, Myers 1983) have found that a power law correlation exists between the line widths and the clump size. The data presented here do not show any evidence for such a correlation (Figure 4.12). In fact, the clump sizes are consistently smaller than those predicted by Larson for a given line width. Such a deviation has also been found by Martin-Pintado et al. (1985) from observations of H_2CO in several molecular clouds. There are several possible explanations for this lack of correlation. One possibility is that the correlation between clump size and linewidth breaks down at small clump sizes. It is also possible that the lack of correlation is due the proximity of the clumps to the H II region since the ambient pressure around H II regions is higher than in the general molecular cloud material. Also, an inherent assumption in all the models predicting the correlation is that the column density is constant across the cloud. So a variation of the column density from clump to clump could also be responsible for the lack of correlation

since the virial relationship (i.e. $GM \sim 2\Delta v^2 L$) together with the constancy of column density are equivalent to the proportionality of Δv to L^n, with $0.38 \leq n \leq 0.6$ (Wilson and Walmsley 1989 and references therein). Some of these possibilities can be examined by mapping the source in a molecule which traces lower densities and hence would be a measure of the bigger clumps in the cloud. Detection of a wider range of clump sizes would be useful in understanding the behavior of such clumps around H II regions.

V. CONCLUSIONS AND FUTURE WORK

§5.1 Conclusions

The study was done in order to obtain a better understanding of the formaldehyde masers in NGC 7538. The millimeter transitions of HCN, HCO^+ and ^{13}CO proved to be good tracers of high density material. HCN traced molecular hydrogen densities of $> 10^6$ cm^{-3}, HCO^+ traced densities of $> 10^5$ cm^{-3} and ^{13}CO traced densities $> 2 \times 10^3$ cm^{-3}. The molecular cloud was found to be very clumpy and the high density material outlined the density enhancement that formed the interface between the H II region and the molecular cloud. The high density tracers indicate the presence of a cavity around IRS 1. The cavity is interpreted as a lack of high density material in that region. The interpretation is supported by the presence of strong ^{13}CO emission in the cavity. The ^{13}CO emission indicates densities of the order of 2×10^3 cm^{-3} in the cavity which is a lower bound and agrees with the requirements of the Boland and de Jong (1981) model for the excitation of the formaldehyde maser. The continuum source, IRS 1, is found to consist of two components - a compact component with an electron density of 2.7×10^6 cm^{-3} in the north and an extended component with $n_e = 1.1 \times 10^5$ cm^{-3} to the south. The masers are found to be associated with the southern, extended component. The inversion curves for the H_2CO maser have been recalculated for the parameters of the extended continuum source. The H_2CO gas has to be situated at a

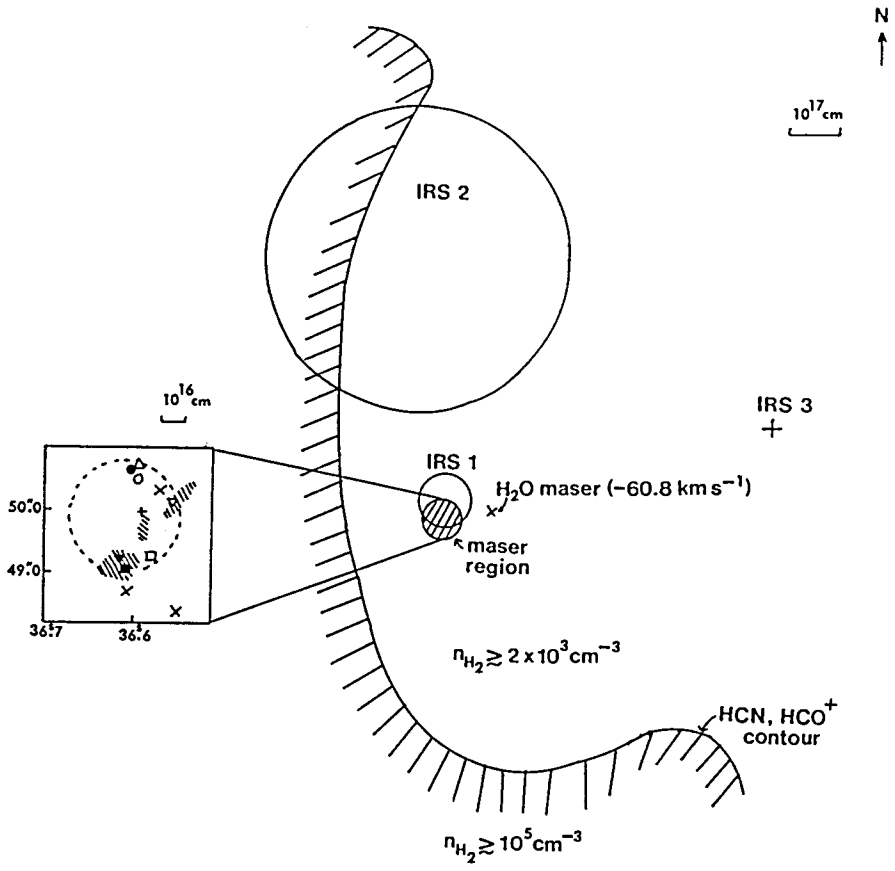

Figure 5.1 - Front view of the molecular cloud around IRS 1, IRS 2, and IRS 3. The circles around IRS 1 and IRS 2 indicate the relative sizes of the radio continuum sources associated with them. The solid contour shows the edge of the high density material surrounding the low density cavity, as seen in the HCN and HCO^+ maps. The hatched circle is the region toward IRS 1 where all the masers (except the H_2O maser) are found. The inset shows an expanded view of this region. The crosses, filled and open squares, the hatched region, and the inverted, filled triangle are various OH masers. The open and filled circles are the H_2CO masers and the open triangle is the CH_3OH maser. A detailed explanation of the symbols can be found in Table 2.4. The linear scale for the main plot is indicated in the upper right hand corner and the linear scale corresponding to the inset is shown just above the inset.

distance of 0.01 pc from the H II region in order to get the observed brightness temperatures. The resulting H_2CO fractional abundance with respect to H_2 is 4×10^{-7}. The various densities required for the excitation of the other masers (e.g. OH and H_2O) can be explained by assuming that these masers are produced in the clumps in the molecular cloud surrounding the H II region.

Figure 5.1 presents a front view of the H II region and the surrounding molecular cloud as found from the molecular observations. The solid line is a contour showing the edge of the cavity, as seen in HCN and HCO^+. The hatched circle in the southern part of IRS 1 shows the region where all the masers are found. The region is expanded in the inset, where the positions of all the masers are seen. A detailed explanation of all the symbols can be found in Table 2.4. The HCN/HCO^+ contour indicates the boundary of the high density material. The material in the cavity is at $n_{H_2} > 2 \times 10^3$ cm^{-3}. The H_2O maser is offset from IRS 1. The position and size of IRS 2 and the postion of IRS 3 are also indicated. Figure 5.2 shows a side view of the region with the velocity distribution of the various masers. The dashed line indicates a possible boundary for the high density material, from the blue shifted HCO^+ maps. The velocity scale is assumed to be linear with distance along the line of sight. The preliminary recombination line results (Gaume et al. 1990) show IRS 1 to have a velocity of about -40 km s^{-1} (marked by the position X_1). On our linear scale, this puts IRS 1 at a distance of about 5×10^{17} cm (0.16 pc) from the H_2CO gas. This does not agree with our calculations, which require the

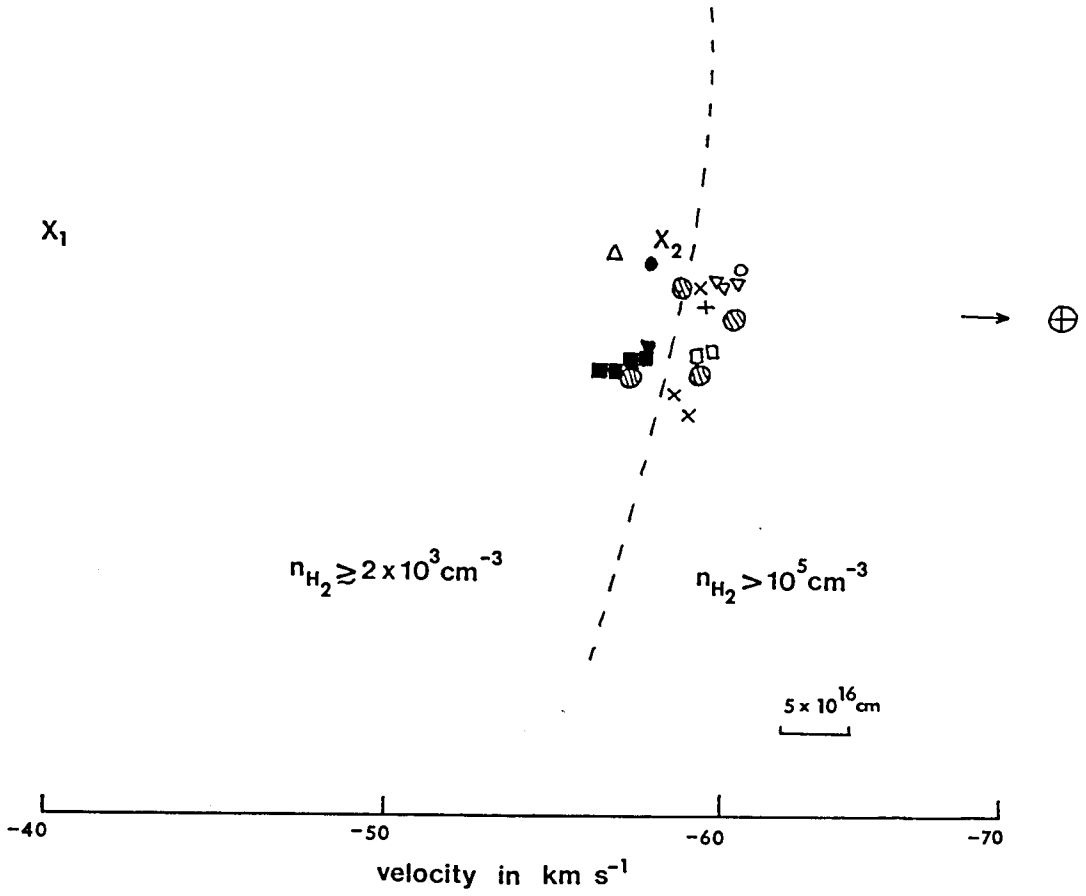

Figure 5.2 - Side view of the region around IRS 1 showing the velocity distribution of the masers. The explanation for the symbols is the same as in Figure 5.1. The velocity scale, indicated at the bottom of the figure, is scaled linearly with distance. The positions X_1 and X_2 are two possible positions of IRS 1 corresponding to different velocities. The dashed line, derived from the ^{13}CO maps and the blue shifted HCO^+ maps, indicates a possible boundary between the low density and high density material. The linear distance scale is shown at the bottom right hand corner and the direction of the line of sight is indicated to the right of the figure.

H_2CO gas to be situated at a distance of 0.01 pc from the H II region. If IRS 1 has a velocity closer to the quiescent velocity of the cloud (marked by X_2), then the H II region is at the right distance from the H_2CO gas, as suggested by the model. This would also agree with the velocities of all the other masers seen toward IRS 1, which range from -56 km s^{-1} to -60 km s^{-1}. Thus, if the masers are in fact associated with IRS 1, a velocity closer to -58 km s^{-1} for the H II region seems more plausible. It is also possible that optical depth effects could be causing the recombination line to have a asymmetric line profile, which in turn could cause a shift in the measured velocity.

The molecular results also provided insight into the nature of the outflow seen in toward IRS 1. The HCO^+ emission has extended line wings that trace a high density molecular outflow. The outflow is oriented at the same position angle as the CO outflow seen in the source. The CO outflow has a greater velocity and spatial extent. Also, the HCO^+ outflow only has a blue wing. The results are consistent with the fact that since HCO^+ traces higher densities, the molecular emission traces the high velocity material closer to the source of the outflow. The HCO^+ emission seems to indicate that the source of the outflow is not IRS 1 but some other source about 15" south of IRS 1. Although no source has been detected at that position, the emission from the quiescent HCO^+ velocities shows an elongated structure perpendicular to the direction of the outflow. It is possible that the outflow is deeply embedded in the high density material and has not been detected.

Finally, it is possible to study the statistical behavior of the high density clumps in the molecular cloud. It is found that the clumps seen in HCN are not resolved by the beam while those seen in HCO^+ are resolved. Since HCN traces densities higher than those traced by HCO^+, it can be concluded that HCN probes the dense cores of the clumps. The presence of unresolved clumps also provides support for the interpretation that the masers originate in the molecular cloud, since masers are essentially a small-scale phenomenon. The clumps also show that the size-linewidth relationship that has been seen to hold for molecular clouds breaks down for our sample of clumps.

The observations in this paper show the usefulness of high resolution observations of molecular clouds in various millimeter transitions.

§5.2 Future Work

The Boland and de Jong model appears specific to the H_2CO masers in NGC 7538. A good test of the model would be to apply it to the masers seen in Sgr B2. Of the five masers detected in Sgr B2, only one (maser C in Gardner et al. 1986) coincides with a compact continuum source. Gardner et al. (1986) also calculate the minimum maser gain for each spectral component of the masers, assuming they are produced by the amplification of the background continuum emission. Maser C has the lowest maser gain while maser A has the highest. High resolution continuum maps at 6 cm and 2 cm (Benson and Johnston 1984) and at

88 GHz (Carlstrom and Vogel 1989) can be used to obtain continuum fluxes which can, in turn, be used to calculate H II region spectra. Following the procedure used for IRS 1 (§4.2), the emission measure for the compact source associated with maser C is found to be about 6 x 10^8 cm^{-6} pc. This is within the range required by the Boland and de Jong model. The model may also be able to account for masers A and D which are situated close to continuum sources. No H II regions have been detected near masers B and E. However, all the masers are near (within 15") sites of OH or H_2O maser emission. Since there must exist some pumping source for these masers, there might still exist compact H II regions which are heavily obscured and thus below the level of detection.

The densities in the Sgr B2 cloud should be sufficient to satisfy the criteria set by the Boland and de Jong model. However, high resolution studies need to be made to trace the local high density structure around the maser regions. Molecular maps of the source in the transitions of high density tracers can provide information about the local conditions around the maser regions.

APPENDIX A

THE ASTROPHYSICAL JOURNAL, 330:L67–L70, 1988 July 1

INTERFEROMETRIC OBSERVATIONS OF THE 1–0 TRANSITION OF HCO^+ TOWARD NGC 7538 IRS 1

WOLFGANG BATRLA, PREETHI PRATAP, AND LEWIS E. SNYDER
Astronomy Department, University of Illinois
Received 1988 March 23; accepted 1988 April 6

ABSTRACT

We report interferometric observations of the molecular cloud toward the compact H II region IRS 1 in NGC 7538 in the 1–0 line of HCO^+. Employing a resolution of 8".5, we find a highly elongated molecular cloud oriented at position angle 52°, perpendicular to the axis of the bipolar CO outflow. In perfect alignment with the blueshifted lobe in CO, strong blueshifted line wings are detected in HCO^+. The origin of the flow is at the center of the HCO^+ cloud, 15" to the south of IRS 1, which is clearly *not* the source that powers this outflow. So far no other indication of star formation has been detected at this position.

Subject headings: interferometry — interstellar: matter — interstellar: molecules — radio sources: lines

I. INTRODUCTION

High-velocity, bipolar flows have been found to be a very marked characteristic of star formation regions with a wide spectrum of masses for the central objects. Toward the compact H II regions IRS 1, IRS 2, and IRS 3 in the star formation region NGC 7538, a high-velocity outflow from the 1–0 transition of CO was first reported by Campbell and Thompson (1984). The authors were not able to spatially separate the location of the blue and red line wings employing an angular resolution of 66". Subsequently, Fisher *et al.* (1985) showed that the high-velocity outflow was oriented along a position angle[1] (in the following denoted by P.A.) of 145°, with a separation of the red and blue shifted lobes of about 44". Interferometric observations with an angular resolution of 7" in the 1–0 line of CO (Scoville *et al.* 1986) confirmed the orientation of the flow, but found a distance between the lobes of only 28". Their result suggested that the compact H II region IRS 1 was located on the axis of the flow, and apparently the central power source. However, in the 1–0 transition of ^{13}CO, the same authors found an east-west elongated structure inclined by a P.A. of 55° with respect to the axis of the ^{12}CO outflow and centered on IRS 1. The east-west orientation in ^{13}CO was consistent with the geometry of an extended structure detected at 5 μm by Hackwell, Grasdalen, and Gehrz (1982). Campbell (1984) proposed that the 5 μm source could be a disk which might play a role in confining the north-south-oriented bipolar flow detected by her high resolution continuum observations at 15 GHz. On small scales the orientation of the outflow is at P.A. 0°, perpendicular to the disk seen in ^{13}CO and 5 μm infrared. The CO outflow axis is at P.A. 145°. If IRS 1 were also the origin of the bipolar CO outflow, it would be rather difficult to explain a change of 55° in the orientation of the outflow axis on such small scales.

In order to resolve this discrepancy and to study the small-scale structure toward NGC 7538 IRS 1 we have mapped several transitions of high-density and medium-density tracing molecules (e.g., three isotopic species of HCN, SO, SiO) with the Hat Creek Millimeter-Array of the University of California, Berkeley (Welch and Thornton 1985). We will limit our discussion in this *Letter* to the most timely and interesting aspect of the results obtained in the 1–0 transition of HCO^+. Detailed results of the remaining material will be reported elsewhere (Pratap, Batrla, and Snyder 1988).

[1] Following the usual definition, we measure the position angle in degrees east of north.

II. OBSERVATIONS

Between 1987 November 23 and 1988 February 27, we observed NGC 7538 in five configurations of the three-element Hat Creek Millimeter-Array, sampling the *u-v* plane in the interval from 2 to 25.4 kλ using a line rest frequency of the 1–0 transition of HCO^+, 89.18852 GHz. The phase tracking center was $\alpha(1950) = 23^h11^m37^s$, $\delta(1950) = 61°11'50"$, and the LSR-velocity -58 km s^{-1}. Integrations of 30 minutes on source were interspersed with 10 minute integrations on the phase calibrator BL Lac. Observations of Mars were used to establish the flux density scale while the radio frequency passband corrections were derived from observations of 3C 84. The correlator backend (Urry, Thornton, and Hudson 1985) was split into eight subreceivers of 64 channels with bandwidth of 10 MHz, yielding a velocity resolution of 0.53 km s^{-1}. The 1–0 transition was centered in one filter in the upper sideband, while the adjacent filter of 64 channels was placed in a line-free portion of the spectrum.

The data were processed using the RALINT software package developed by the Radio Astronomy Laboratory at the University of California, Berkeley. The *u-v* data were gridded, convolved, and Fourier-transformed to obtain maps of 128 × 128 pixels with a pixel size of 2", employing natural weighting. Forty channels centered on the line were mapped. Since the source IRS 1 shows continuum emission at 3 mm, we obtained a continuum map from the average over the channels in the line-free filter. This map was subtracted from the individual channel maps. The maps were then CLEANed and restored using an elliptical Gaussian approximation to the synthesized beam of 8".5 × 6".7, P.A. 82°. The resulting rms noise level in one channel map is 0.375 Jy per beam.

III. RESULTS AND DISCUSSION

In Figure 1 we present an overlay of two individual channel maps. Solid triangles outline the positions of IRS 1, IRS 2, and IRS 3. The solid contours show the emission at VLSR -57.1 km s^{-1}; dashed contours, that at -59.7 km s^{-1}. The most striking characteristic seen at -57 km s^{-1} is the symmetric,

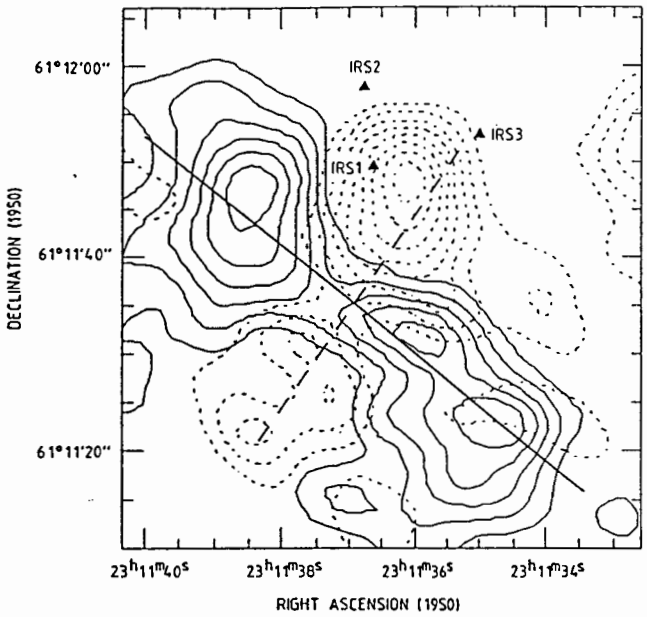

FIG. 1.—Overlay of two channel maps of the 1–0 transition of HCO^+. Solid contours show the emission centered at -57.1 km s^{-1}; dashed contours, that at -59.7 km s^{-1}. Contour intervals in both cases are 1.3 K brightness temperature T_R^*. The solid triangles outline the position of the infrared sources IRS 1, IRS 2, and IRS 3 (Hackwell *et al.* 1982). The solid line (P.A. 52°.5) indicates the location of the spectra displayed in Fig. 2; the dashed line (P.A. 142°.5), that of the spectra in Fig. 4.

double-lobed structure with a pronounced drop in intensity toward the center. The feature is highly elongated with an aspect ratio of 3.5 to 1 and is oriented along P.A. 52°. In Figure 2 we show individual spectra along the main axis outlined in Figure 1 by the solid line. The positions are given in seconds of arc along P.A. 52°.5 relative to $\alpha(1950) = 23^h11^m36^s.7$, $\delta(1950) = 61°11'34''$. A comparison reveals that the drop in intensity toward the center is caused by a shift of the line peak to negative velocities. In addition the spectra toward the zero position depict symmetric, broad line wings extending about 10 km s^{-1}. At positive offsets the line wings disappear, and the profiles are of Gaussian shape with VLSR -57.58 and Δv_{FWHP} of 1.96 km s^{-1}. This difference in line shapes is apparent from Figure 3 where the spectrum at offset 20 shifted by one channel (*thin line*) is plotted together with that at offset 5 (*thick line*). Toward negative offsets (see Fig. 2), the peaks of the lines shift back to more positive velocities. The profiles display extended redshifted wings, and at offset -30 indications of a possible double structure can be seen.

The HCO^+ emission at -59.7 km s^{-1} (*dashed contours* in Fig. 1) shows an elongated structure which is perpendicular to the first one. There is a very strong contrast in intensity of 3 to 1 along the feature, the stronger peak being to the northwest. Spectra along the main axis of this feature, shown by the dashed line in Figure 1, are displayed in Figure 4. The positions given are offsets in seconds of arc relative to $\alpha(1950) = 23^h11^m36^s.7$, $\delta(1950) = 61°11'37''$ along P.A. 142°.5. At the central positions (0 and 5 in Fig. 4) we see symmetric, broad line wings consistent with our above findings. At positive offsets we notice weak emission at slightly lower velocities. Toward more negative offsets, the peaks of the profiles shift to progressively lower velocities, and extremely asymmetric, strong blueshifted line wings appear.

We interpret the kinematic structure of the emission as a high-velocity flow interacting with a molecular cloud. The center of the outflow, at the intersection of the two elongated emission features in Figure 1, is marked by symmetric, high-velocity line wings. It is located at $\alpha(1950) = 23^h11^m37^s.1$, $\delta(1950) = 61°11'33''$. 15″ to the south of IRS 1. The flow appears bipolar with a spatially very well defined, strong, blueshifted lobe to the northwest. The map at -59.7 km s^{-1} outlines the extent of the flow. The direction is very well aligned with the orientation of the bipolar CO outflow along P.A. 145° (Scoville *et al.* 1986). Spatial and velocity extent agree very well with the blueshifted CO lobe. The redshifted counterpart is weaker and not so well defined in the 1–0 line of HCO^+. This could be explained if the outflowing gas to the southeast is confined by high-density molecular material. Campbell and Thompson (1984) have shown that a steep increase in molecular hydrogen column density exists to the south of the visible H II region.

No radio continuum or infrared source has been detected at the center of the outflow. However, the position coincides with a high-density molecular condensation elongated along P.A. 52°, which was detected in the 1–0 transition of HCN (Pratap, Batrla, and Snyder 1988) and has similar extent and orientation as the HCO^+ cloud at -57.1 km s^{-1}. Both clouds trace the interface between the extended H II region to the north and the molecular cloud south of it. The pronounced elongation gives this cloud the appearance of a disk seen edge-on. By Gaussian fits to the line profiles, we find the peak of emission at the edges of this disk to be identical in velocity. Toward the center, in the vicinity of the outflow source, the line peaks are markedly blueshifted, pointing to a radial motion of the gas in

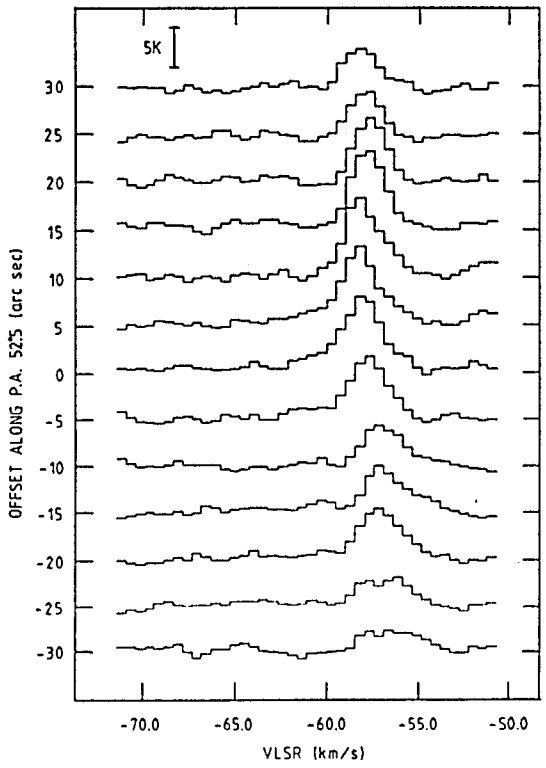

FIG. 2

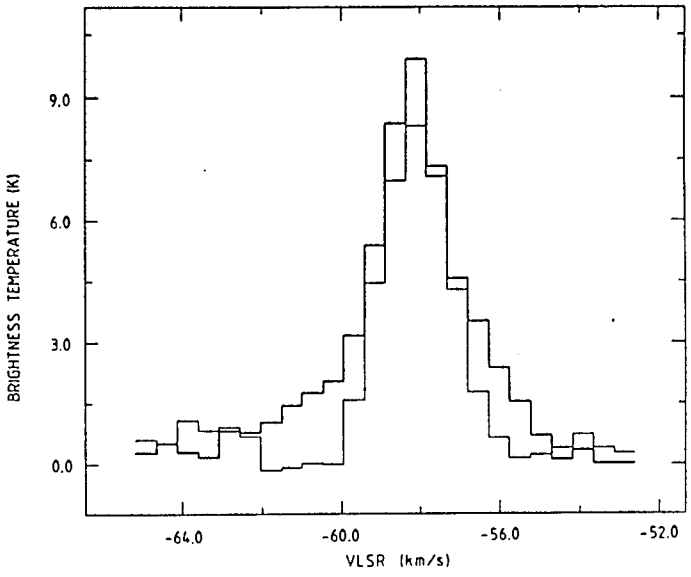

FIG. 3

FIG. 2.—Individual spectra along position angle 52°.5. The offsets are given in seconds of arc relative to $\alpha(1950) = 23^h11^m36^s.7$, $\delta(1950) = 61°11'34''$. The bar at top left gives the brightness temperature scale.

FIG. 3.—Overlay of the spectrum at offset 20 (*thin line*) and offset 5 (*thick line*) in Fig. 2. The spectrum at offset 20 was shifted by one channel to the left so that the channels of the peak intensities agree. Note the broad symmetric line wings at offset 5.

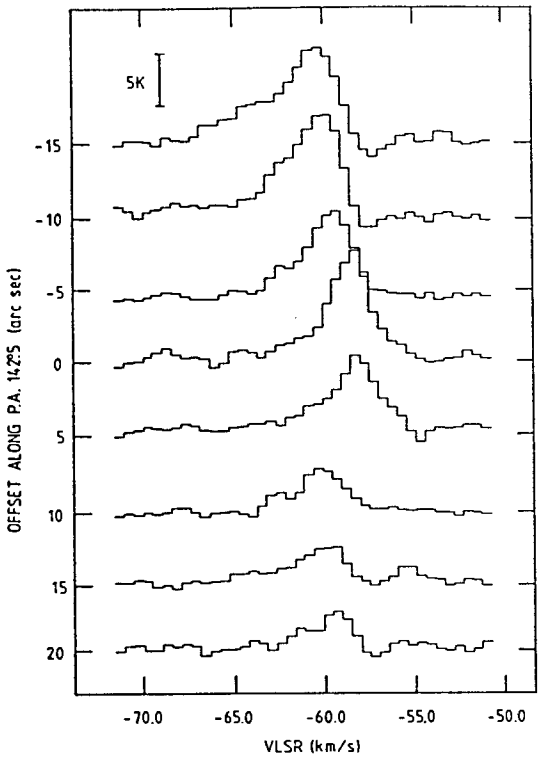

FIG. 4.—Individual spectra along position angle 142°5. The offsets are given in seconds of arc relative to $\alpha(1950) = 23^h11^m36^s7$, $\delta(1950) = 61°11'37''$. The bar at top left gives the brightness temperature scale.

the disk, probably caused by an interaction between the outflow and the disk. We cannot distinguish whether this motion is directed toward or away from the source. For a symmetrical disk, however, one would expect to find a red-shifted component of the radial motion as well. The latter is not detectable in this transition. It is noteworthy to mention that the disk we describe is not identical to the east-west oriented ^{13}CO condensation detected by Scoville *et al.* (1986). The high-velocity outflow is oriented perpendicular to the elongated molecular cloud. That the central power source of the outflow escaped detection has two possible explanations: (1) the source is of low luminosity, or (2) the source is very young and obscured by a considerable amount of extinction.

The perfect agreement in orientation and extent of the newly detected HCO^+ outflow with the bipolar flow found in the 1–0 transition of CO lead us to conclude that both are manifestations of the very same physical process. IRS 1 is not the source which powers both flows; rather, the center of the outflow is located 15″ to the south of IRS 1. Since high-velocity outflows are closely associated with the early stages of star formation, the flow points to the formation of a star or stars at the high-density interface between the visible H II region and the molecular cloud to its south. This finding clearly shows that sequential star formation is progressing from north to south through the molecular cloud. No infrared or radio continuum source is known at the center of the outflow.

We thank the director of the Radio Astronomy Lab at University of California, Berkeley, W. J. Welch, for the observing time. We acknowledge the cooperation of all astronomers of the Laboratory who made the remote observations with the Hat Creek Array possible. Mel Wright was very helpful with the data reduction using the RALINT interferometer software. This project has been supported by funds provided for the Berkeley-Illinois-Maryland-Array project by the University of Illinois.

REFERENCES

Campbell, B. 1984, *Ap. J. (Letters)*, 282, L27.
Campbell, B., and Thompson, R. I. 1984, *Ap. J.*, 279, 650.
Fisher, J., Sanders, D. B., Simon, M., and Solomon, P. M. 1985, *Ap. J.*, 293, 508.
Hackwell, J. A., Grasdalen, G. L., and Gehrz, R. D. 1982, *Ap. J.*, 252, 250.
Pratap, P., Batrla, W., and Snyder, L. E. 1988, in preparation.
Scoville, N. Z., Sargent, A. I., Sanders, D. B., Claussen, M. J., Masson, C. R., Lo, K. Y., and Phillips, T. G. 1986, *Ap. J.*, 303, 416.
Urry, L., Thornton, D. D., and Hudson, J. 1985, *Pub. A.S.P.*, 97, 745.
Welch, W. J., and Thornton, D. D. 1985, in *International Symposium on Millimeter and Submillimeter Wave Radio Astronomy*, ed. J. Gomez-Gonzalez (Granada: URSI), p. 53.

WOLFGANG BATRLA, PREETHI PRATAP, and LEWIS E. SNYDER: University of Illinois, Department of Astronomy, 349 Astronomy Building, 1011 West Springfield Avenue, Urbana, IL 61801

APPENDIX B

THE ASTROPHYSICAL JOURNAL, 341:832–838, 1989 June 15

MASERS AND MOLECULES NEAR THE UNUSUAL FORMALDEHYDE MASER NGC 7538 IRS 1

PREETHI PRATAP, WOLFGANG BATRLA, AND L. E. SNYDER
Astronomy Department, University of Illinois
Received 1988 July 21; accepted 1988 November 16

ABSTRACT

The physical conditions in the molecular cloud associated with NGC 7538 IRS 1 and its unusual 6 cm formaldehyde (H_2CO) maser have been examined via interferometric observations of the emission from the three hyperfine lines of the $J = 1$–0 transition of hydrogen cyanide (HCN). The data show that the peak of the HCN emission is offset from any infrared source. There is a pronounced lack of emission around IRS 2 and to a lesser extent around IRS 1. Since the $J = 1$–0 transition of HCN requires neutral hydrogen (H_2) densities $\geq 10^6$ cm^{-3} for excitation, the lack of HCN emission around IRS 1 and IRS 2 suggests lower H_2 densities in that region. This cavity in the HCN emission could be a result of the expansion of the H II region. This expansion could also cause the highly clumped appearance of the HCN emission which shows evidence of structures smaller than the resolved density structures in the molecular cloud surrounding IRS 1 and IRS 2. The density structure in HCN seems to agree with the requirements of the Boland and de Jong H_2CO maser model, and the presence of high-density clumps around IRS 1 can explain the different excitation requirements for the H_2CO masers and the OH masers.

Subject headings: infrared: sources — interstellar: molecules — masers — nebulae: H II regions — nebulae: individual (NGC 7538)

I. INTRODUCTION

NGC 7538 is an optically visible H II region situated in the Perseus arm of the galaxy at $l^{II} = 111°.54$ and $b^{II} = 0°.78$ and at a distance of ≈ 3.5 kpc. Radio measurements by Martin (1973) identified three very compact radio emission components located near the southern border of the visible H II region. These components were found to be strong infrared sources IRS 1, 2, and 3 by Wynn-Williams, Becklin, and Neugebauer (1974). The very unusual nature of NGC 7538 IRS 1 began to emerge when Downes and Wilson (1974) detected the $J_{K_{-1}K_1} = 1_{10} \rightarrow 1_{11}$ transition of formaldehyde (H_2CO) at 4829.660 MHz ($\lambda \approx 6$ cm) in emission toward this source and Rots *et al.* (1981) showed that the H_2CO is in maser emission with the masers offset from the 4.8 GHz continuum peak of IRS 1 by $\sim 0''.3$. To date, only five additional H_2CO masers have been found in spite of numerous searches (Forster *et al.* 1985), and all of these are located in the H II region/molecular cloud complex Sgr B2, close to the Galactic center (Whiteoak and Gardner 1983; Gardner *et al.* 1986). Thus detections of the H_2CO maser are extremely rare, perhaps because (*a*) the maser emission may be hidden by the more common, wide absorption features of Galactic H_2CO; (*b*) H_2CO masers have short lifetimes; (*c*) H_2CO masers are intrinsically weak; or (*d*) the range of conditions supporting the H_2CO masers is very rare. In support of the second possibility, both Forster *et al.* (1985) and Wilson and Snyder (1985) have found time variability in the H_2CO maser emission toward NGC 7538 IRS 1.

Boland and de Jong (1981) have proposed a model to explain the H_2CO maser emission in which the ultracompact H II region[1] NGC 7538 IRS 1, and its surrounding molecular cloud must have rather specific properties. The H II region must be very compact, with an emission measure in the range 10^8–10^{10} cm^{-6} pc, so that it is optically thick at centimeter wavelengths but still optically thin at millimeter wavelengths. As a consequence, the free-free continuum radiation from this H II region inverts the population of the 1_{10} level relative to the 1_{11} level of H_2CO. The requirements for this model are that the H_2 density should be $\approx 3 \times 10^4$ cm^{-3}, the masing H_2CO must be in front of the H II region so that it amplifies the continuum radiation, the gas must have a large velocity gradient which allows millimeter-wavelength radiative pumping photons to escape, and molecules must be aligned in velocity over long path lengths to create sufficient amplification. Clearly, if the detailed parameters of this model can be confirmed observationally, the H_2CO maser could be used to detect and locate very compact H II regions which are below the conventional level of detection, yet adequate for pumping the maser (see, e.g., Gardner *et al.* 1986). Thus, H_2CO maser emission is a potentially interesting tool for detecting and studying ultracompact H II regions associated with regions of star formation.

The purpose of this paper is to show how selected millimeter-wave interferometric measurements may be used to measure some of the parameters necessary for verifying the proposed pumping mechanism of Boland and de Jong (1981) for the H_2CO maser at 6 cm wavelength. To do this, the Hat Creek Millimeter Array was used to map the NGC 7538 IRS 1 region around the H_2CO maser location in the three hyperfine lines of the $J = 1$–0 transition of HCN at 88.6 GHz. This transition was chosen because it thermalizes at H_2 densities of $\geq 10^6$ cm^{-3} over a wide range of kinetic temperatures. Because a critical density of 3×10^4 cm^{-3} is required for population inversion of the 1_{10} level of H_2CO relative to the 1_{11} level, and because the lowest levels of H_2CO thermalize at H_2 densities $\geq 3 \times 10^3$ cm^{-3}, anywhere that the $J = 1$–0 transition of HCN is observed in emission should be a region where the 6 cm H_2CO maser cannot exist. In particular, with a 9″ beam, it is possible to detect small-scale structure in the high-density

[1] Ultracompact H II regions, as defined by Israel, Habing, and de Jong (1973), have $d < 0.1$ pc (3×10^{17} cm) and $n_e > 10^4$ cm^{-3}, whereas compact H II regions have 0.1 pc $< d <$ 1 pc and 10^4 cm^{-3} $> n_e > 10^3$ cm^{-3}.

molecular material both near the interface of the H II region where the H_2CO maser emission originates and also where the other masers such as OH, H_2O, $^{15}NH_3$, and CH_3OH are found. In turn, this should be very helpful in understanding the well known but puzzling correlation between H_2CO, OH, and H_2O masers (see, e.g., Gardner *et al.* 1986).

II. OBSERVATIONS

Observations which tracked the position $\alpha(1950) = 23^h11^m37^s$, $\delta(1950) = 61°11'50''$ (near the IRS 1 position) were performed with the Hat Creek Millimeter Array during the period from 1985 October to 1987 August. The Hat Creek hybrid spectrometer allows simultaneous observations of spectral lines in the upper and lower sidebands (Urry, Thorton, and Hudson 1985). For the HCN observations, the upper sideband consisted of two correlator segments of 128 channels each, with one of the correlator segments tuned to the HCN $J = 1$–0 frequencies ($F = 1$–1 at 88630.4157 MHz, $F = 2$–1 at 88631.8473 MHz, $F = 0$–1 at 88633.9360 MHz) and the other tuned to the H52β recombination line at 88405.99 MHz. The correlator segment with the HCN line had a bandwidth of 10 MHz, and a velocity resolution of 0.25 km s^{-1}. The correlator segment which contained the recombination line had a bandwidth of 40 MHz and a velocity resolution of 1 km s^{-1}. Six configurations of the three-element array were used with UV spacing ranging from 2.2 kλ to 18 kλ. The instrumental phase was calibrated against the quasar BL Lac at ~35 minute intervals. The flux density scale was fixed by pointing observations of Venus. The RF passband shape was calibrated using observations of the quasar 3C 84.

Visibility data were gridded, convolved, and Fourier transformed to obtain 256 × 256 maps with a pixel size of 2″. A continuum map was constructed from the 15 channels at each end of the correlator segment which were selected to exclude the line signal and avoid bad end channels. This map was then subtracted from each of the channel maps, and the resulting maps were CLEANed. The full width at half-maximum (FWHM) of the synthesized beam was 9.″0 in declination by 9.″4 in right ascension. The rms noise level in the cleaned channel maps is 0.8 Jy per beam.

A continuum map was also made over a bandwidth of 32 MHz with the data in the second correlator segment in the upper sideband. The synthesized beam had a FWHM of 8.″9 in right ascension and 8.″5 in declination. This map was CLEANed down to a theoretically expected noise level of 0.03 Jy per beam. All line and continuum maps were obtained with natural weighting.

III. DISCUSSION

a) HCN *Observations*

Figure 1 presents the channel maps across the $F = 2$–1 component of the $J = 1$–0 transition of HCN. The lowest contour in the map is 1.2 Jy per beam, and subsequent contours are plotted at equal intervals of 1.2 Jy per beam. These channel maps show the detailed velocity structure of the HCN emission, relative to the positions of the three infrared sources IRS 1, IRS 2, and IRS 3. The HCN emission is very pronounced to the northwest of IRS 1 at velocities between −56.0 and −57.0 km s^{-1} with a peak value of 3.6 Jy per beam at −56.0 km s^{-1}. The peak of the emission then shifts to the east and south of IRS 1 as the velocity approaches the LSR velocity of the molecular cloud associated with the source ($V_{LSR} = -58$ km s^{-1}). As the velocity becomes more negative, the emission peak shifts to the southwest of IRS 1. The HCN emission thus appears to trace a cavity around IRS 1. Note that the HCN emission never peaks at the IRS 1 position. In addition, there are two emission peaks along the east-west direction which are offset by ~25″ on either side of IRS 1. These peaks can be most clearly seen in the channel map corresponding to a velocity of −58.3 km s^{-1}.

The cavity around IRS 1 is clearly seen in Figure 2*a* which is a map of the emission in the $J = 1$–0, $F = 2$–1 transition of HCN averaged over the velocity interval -61.0 km s$^{-1} \leq V_{LSR} \leq -55.0$ km s^{-1} (*solid contours*). Figure 2*a* emphasizes the east-west extent of the molecular material traced by the HCN emission. The east-west structure outlines the interface between the visible H II region to the north (*hatched region*) and the extended molecular cloud to the south. The H II regions associated with IRS 1 and IRS 2 seem to be located at this interface in the dense molecular gas. This is consistent with a gradient in H_2 column density found from ^{12}CO and ^{13}CO observations (Campbell and Thompson 1984), and it indicates a sharp increase in H_2 column density from the north to south across the interface. Campbell and Thompson (1984) have also found that the extinction $A(V)$ is 14 ± 6 mag toward IRS 2 and between 37 and ≈60 mag toward IRS 1, which is consistent with the density gradient and suggests that IRS 1 is more deeply embedded in higher density material than IRS 2.

b) *Continuum Observations*

The dashed contours in Figure 2*a* outline the 3.3 mm continuum map which was described in § II. The map shows an unresolved source with a peak value of 1.1 Jy at the position of IRS 1 and a weak northward extension toward IRS 2. This continuum flux density value is consistent with the 2.7 mm continuum flux density of Scoville *et al.* (1986). The millimeter flux densities are more than a factor of 2 higher than the values derived from the model spectrum of Henkel, Wilson, and Johnston (1984; see their Fig. 2). The turnover frequency of their spectrum was found to be 20 GHz from data points at 15 and 23 GHz, but the millimeter data suggest that the continuum spectrum continues to rise. However, for high millimeter flux densities, the Boland and de Jong (1981) model predicts that the 2 cm H_2CO transition should be observed in maser emission. This has not been observed. Martin-Pintado *et al.* (1985) reported only very stringent upper limits on 2 cm H_2CO maser emission. In addition, the Boland and de Jong model for the 6 cm H_2CO maser emission requires the H II region to be optically thin at millimeter wavelengths. All of these observational and model constraints can be satisfied by invoking a two-component model for the H II region—a hot, dense, compact component which is optically thick at millimeter wavelengths and a cooler, less dense and more extended component which provides the millimeter photons required to pump the maser.

Evidence for both components can be found from centimeter observations. The most convincing fact is the difference in geometry between the 4.8 and 15 GHz continuum emission regions. Figure 2*b* shows the 15 GHz continuum map made with 0.″1 resolution by Campbell (1984). The peak of this map is contained in the two-lobed emission region centered on IRS 1. The elongated structure suggests a bipolar flow of ionized material. To the south of the central peak indications of a weak spherical extension of the emission can be seen, while to the north an extension is not as well defined. In contrast, the 4.8 GHz maps of Dickel *et al.* (1982) and Campbell (1984) display a spherical region of radius 0.″5 which is centered 0.″5 south of

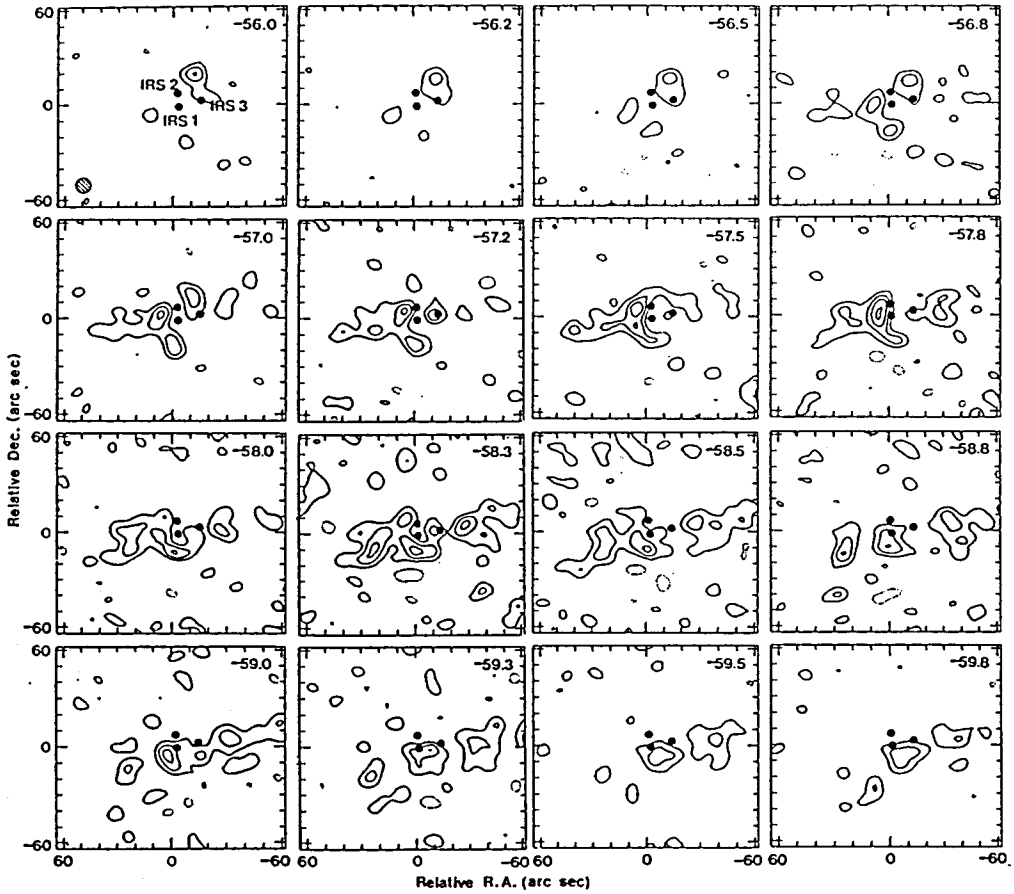

FIG. 1.—Channel maps over the velocity interval covering the HCN ($J = 1$–0, $F = 2$–1) line. The three solid circles show the positions measured by Hackwell, Grasdalen, and Gehrz (1982) for the infrared sources IRS 1 [$\alpha(1950) = 23^h11^m36^s.7 \pm 0.2$; $\delta(1950) = 61°11'48'' \pm 1$], IRS 2 [$23^h11^m36^s.8 \pm 0.2$; $61°11'56'' \pm 1$], and IRS 3 [$23^h11^m35^s.0 \pm 0.2$; $61°11'51'' \pm 1$]. Label at the top right of each panel displays the LSR velocity corresponding to that map. Hatched circle at the bottom left of first panel outlines the FWHM of the synthesized beam. Lowest contour is at 1.2 Jy per beam, and subsequent contour levels are at intervals of 1.2 Jy per beam. The (0, 0) pixel position in the maps is at $\alpha(1950) = 23^h11^m37^s$ and $\delta(1950) = 61°11'50''$.

IRS 1 (indicated by the dashed ring in Fig. 2*b*) and features a weak extension to the north. In the proposed two-component model for the H II region the 15 GHz emission outlines the hot, compact component, while the 4.8 GHz emission depicts the cooler and slightly extended component. The resolution of the 23 GHz observations of Henkel, Wilson, and Johnston (1984) and of the millimeter continuum observations is too low to resolve the two components. The southern extended component might be created when the bipolar flow is confined by the high-density molecular material to the south of IRS 1 to a region of radius 0".5 or $\sim 2 \times 10^{16}$ cm, the center of which is coincident in position with the dominant source of the 4.8 GHz continuum peak. To the north, the ionized flow escapes the confinement of the dense material and runs into the visible H II region. Evidence of this is seen from the observations of shock excited emission from the vibrationally excited levels of molecular hydrogen, which is illustrated by the cross-hatched region in Figure 2*a* (Fischer *et al.* 1980).

In order to calculate the parameters of the two components, it is necessary to use high-resolution observations which resolve the source. For the extended component the electron temperature, T_e, can be calculated from the 4.8 GHz flux density—assuming that the emission is optically thick. The source size is 0".5, and a distance of 3.5 kpc is assumed. The equations from Olnon (1975) for a spherical H II region with a constant electron density give a T_e of 8500 K for the extended component. In order to calculate the electron density for this component, the integrated flux density from the southern extension of the 15 GHz map was used. The fraction of the flux density, in this southern component was found to be 0.2 Jy. This value, along with the assumption that the extended component is optically thin at 15 GHz, resulted in an electron density, n_e, of 1.2×10^5 cm^{-3} and an emission measure of 2.2×10^8 cm^{-6} pc (which falls within the range required by Boland and de Jong 1981 for pumping the H_2CO maser). The 3.3 mm flux density contribution of the extended southern

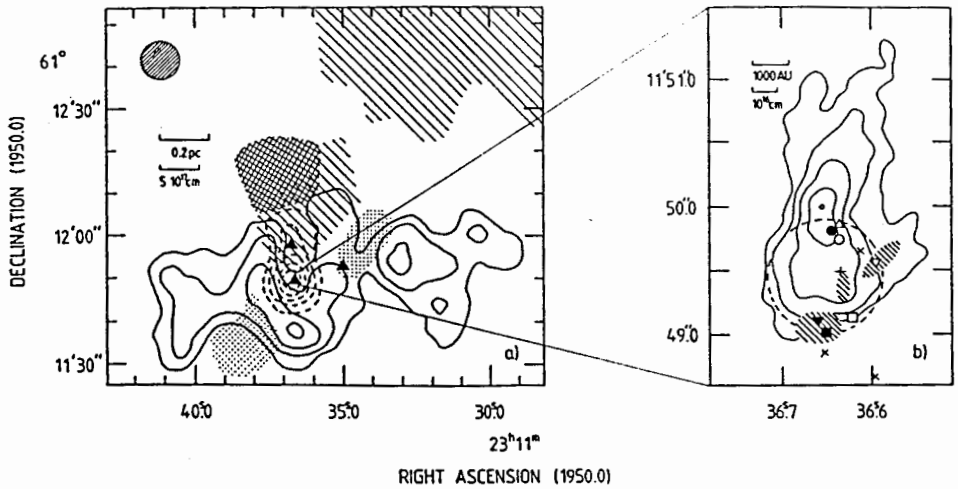

FIG. 2.—(*a*) Map of the average emission in the HCN ($J = 1$–0, $F = 2$–1) transition in the velocity interval $-61.0 \leq V_{LSR} \leq -55.0$ km s^{-1} (solid contours at intervals of 0.5 Jy per beam; the peak value in the map is 2.16 Jy per beam) overlaid with a map of the 3 mm continuum emission (dashed contours at intervals of 0.18 Jy per beam; the peak of the continuum has a value of 1.1 Jy per beam). Solid triangles mark the positions of the infrared sources IRS 1 (south), IRS 2 (north), and IRS 3 (west). Cross-hatched area corresponds to the half-power width of the intensity of emission from vibrationally excited hydrogen (Fischer *et al.* 1980), while hatched regions outline the optical H II region (Campbell 1985) and dotted fields outline the red (southeast) and blue (northwest) lobes of the high-velocity CO emission (Scoville *et al.* 1986). Hatched circle at the top left gives the FWHP of the synthesized beam of the HCN observations and the 3 mm continuum observations. (*b*) Map of the 15 GHz continuum emission (from Campbell 1984) overlaid with symbols denoting regions of maser emission associated with IRS 1. The symbols are explained in Table 1. Dashed ring indicates the extent and position of the 4.8 GHz continuum emission. The water maser position lies outside the map to the southwest. The second highest contour in the map is centered at the IRS 1 position.

component was found to be 0.2 Jy using these values of n_e and E_m. The remaining 3.3 mm flux density of 0.9 Jy was taken as the contribution from the compact component and was assumed to be optically thin. This gave $n_e = 2.7 \times 10^6$ cm and $E_m = 3 \times 10^{10}$ cm^{-6} pc. All these numbers are upper limits since the dust contribution to the flux densities has not been taken into account. In order to verify this scenario, further tests are needed with additional high resolution continuum observations at frequencies higher than 15 GHz.

c) Masers near NGC 7538 IRS 1

Figure 2*b* shows that all the maser emission sources are associated with the southern part of the ultracompact H II region NGC 7538 IRS 1, apparently at the interface between the density-confined ionized gas and the neutral gas. Table 1 lists the LSR velocities and positions of all the masers observed toward IRS 1. The OH masers all have velocities in the range from -56.2 km s^{-1} to -60.1 km s^{-1}. In general, the 1720 MHz OH masers are found in two spatially separated velocity groups, one with velocities lower than -58.0 km s^{-1} and the other with higher velocities. The 1665 MHz and the 1667 MHz OH masers have velocities that are mostly lower than -58.0 km s^{-1}. The positions of the 1720 MHz and the 1665 MHz OH masers have been obtained from VLBI measurements (Forster *et al.* 1982; Norris *et al.* 1982). The 4765 MHz OH maser has three main components which are at -57.06, -58.75, and -59.19 km s^{-1}. There is also a component of the 4765 MHz emission at -60.1 km s^{-1} which is situated near the 4.8 GHz continuum peak. The description of the symbols corresponding to the various masers in Figure 2*b* is given in the last column of Table 1. The 1720 MHz, the 1665 MHz, and the 4765 MHz OH masers all appear to be associated with the southern component of the H II region. The masers are spatially grouped, but their different velocity components are not necessarily correlated. This may be due to the masers arising from different points along the line of sight and being affected by the velocity field around the expanding H II region. The components of the 1665 MHz OH maser which have velocities higher than -59.0 km s^{-1} appear to be offset to the south of the H II region. The H_2CO masers do not seem to be spatially coincident with any of the OH masers, even though the velocities of the two H_2CO masers are within the same range as that of the OH masers. In fact, Guilloteau and Lucas (1981) conclude that since the 1720 MHz OH spectrum is much more complex than the H_2CO spectrum and since the two masers are not spatially coincident on small scales, they arise in regions with different excitation conditions. Similar conclusions have been drawn regarding the coincidence of the 4765 MHz OH masers (Palmer, Gardner, and Whiteoak 1984) and the main line OH masers (Norris *et al.* 1982) with the H_2CO maser spots. However, recent VLBI measurements of the CH_3OH maser position in this source (Menten *et al.* 1988) indicate that this maser is, within the errors, spatially coincident with the H_2CO masers. In addition, the two velocity components that have been observed also coincide with the velocities of the H_2CO masers. The H_2O maser, which has a strong component at -60.1 km s^{-1} and several weaker components at much lower velocities, is situated just off the map to the west of IRS 1 in Figure 2*b*. The NH_3 and $^{15}NH_3$ masers are not shown in the figure since interferometric position measurements have not been made.

Since observations have, in general, ruled out radiative pumping mechanisms for the OH masers around H II regions (Elitzur 1985), collisional pumping schemes have to be con-

TABLE 1

MASERS NEAR IRS 1

Molecule	Frequency (MHz)	LSR Velocity (km s^{-1})	Position α(1950): 23^{h}11^m	Position δ(1950): 61°11′	Symbols
OH[a]	1665.4	−58.4 ± 0.1	36.653 ± 0.025	48.853 ± 0.249	×
		−58.9	36.597 ± 0.022	48.697 ± 0.229	×
		−59.2	36.615 ± 0.021	49.636 ± 0.240	×
		−59.6	36.60 ± 0.02	49.652 ± 0.150	▽
		−59.9	36.598 ± 0.021	49.652 ± 0.153	▽
		−60.1	36.597 ± 0.023	49.659 ± 0.167	▽
OH[a]	1667.4	−59.9 ± 0.1	36.60 ± 0.02	49.670 ± 0.150	▽
		−59.4	36.623 ± 0.022	49.495 ± 0.162	+
OH[b]	1720.5	−56.2 ± 0.1	36.659 ± 0.010	49.00 ± 0.10	■
		−56.6	36.658	49.00	■
		−57.1	36.649	49.05	■
		−57.6	36.655	49.05	■
		−57.8	36.661	49.11	▼
		−59.1	36.624	49.13	□
		−59.4	36.623	49.15	□
OH[c,d]	4765.6	−57.06 ± 0.05	36.65	49.0	▨
		−58.75	36.60	49.6	▨
		−59.19	36.65	49.0	▨
		−60.10	36.63	49.4	▨
H_2CO[e]	4829.7	−57.9 ± 0.4	36.645 ± 0.014	49.82 ± 0.10	●
		−60.1	36.637	49.74	○
CH_3OH[f]	12178.6	−56.39 ± 0.01	36.64 ± 0.25	49.9 ± 0.25	△
		−60.0	...	...	...
NH_3[g,h]	18499.4	−60.0 ± 0.01	36.5	46.0	...
H_2O[i,j]	22235.1	−60.8 ± 0.2	36.47 ± 0.05	49.4 ± 0.	...
		−70.7	36.6 ± 0.4	49 ± 3	...
		−84.4	...	...	...
		−89.4	...	...	...
$^{15}NH_3$[h,l]	22879.4	−55.6 ± 0.1	36.6	48.0	...
		−56.1 ± 0.2	...	...	...
		−58.5 ± 0.5	...	...	...
		−59.7 ± 0.2	...	...	...
		−60.1 ± 0.2	...	...	...
HCN clumps[m]	88631.8	−55.75 ± 0.25	35.4 ± 4.7	1′09.1 ± 4.5	...
		−57.75	37.7	50.0	...
		−58.25	40.1	40.0	...
			37.0	40.0	...
			33.2	55.9	...
		−59.0	37.3	45.0	...
		−60.0	35.8	44.5	...

[a] Norris *et al.* 1982.
[b] Forster *et al.* 1982.
[c] Velocities from Gardner and Martin-Pintado 1983.
[d] Palmer, Gardner, and Whiteoak 1984. The absolute positions of the masers were not given, but the positions of the three regions where groups of masers were found were indicated. Since the positions are of the areas of maser emission, no errors are given.
[e] Rots *et al.* 1981.
[f] Batrla *et al.* 1987.
[g] Madden *et al.* 1986.
[h] The observations were made with single-element radio telescopes so the maser positions could not be determined accurately.
[i] Genzel and Downes 1976.
[j] Forster *et al.* 1978.
[l] Mauersberger, Wilson, and Henkel 1986.
[m] This paper.

sidered. The typical H_2 densities required for inverting the OH maser lines with collisions are of the order of 10^7 cm^{-3}. Such densities can be achieved in dense shells around H II regions (Elitzur and de Jong 1978). In IRS 1 the OH masers appear to be situated around the edge of the ionized region, which is consistent with the above model. The H_2CO maser, however, requires a different model to explain the observed emission because H_2 densities $\gtrsim 3 \times 10^5$ cm^{-3} quench the maser. According to the Boland and de Jong model, the H_2CO maser is inverted by free-free emission from the H II region and requires densities of $\approx 3 \times 10^4$ cm^{-3}. Since the HCN emission is an indication of H_2 densities of $\gtrsim 10^6$ cm^{-3}, the H_2CO emission must be originating in the region between the ionized material and the surrounding molecular cloud where no HCN emission is seen. Since both the OH and H_2CO masers seem to arise from the edge of the ionized region, an explanation for their excitation requires varying H_2 densities on small scales. Such density enhancements could be caused by the expansion of the H II region into an inhomogeneous molecular cloud. The clumpy nature of the HCN maps appears to support this inter-

pretation. The emission appears to be concentrated in clumps which have a velocity range from -56.0 km s^{-1} to -59.8 km s^{-1}. This clumping, along with the broad line shapes of the HCN emission, could be an indication of unresolved clumps on a scale smaller than the present beam. Figure 3 shows a sample HCN spectrum taken at a position of $(\Delta\alpha, \Delta\delta) = (-5\overset{s}{.}0, 5\overset{s}{.}0)$ which corresponds to one of the clumps to the east of IRS 1 and which is at one edge of the cavity. The line profiles of the HCN transitions have widths of the order of 2–3 km s^{-1} which are an order of magnitude wider than thermal line widths associated with kinetic temperatures of ~30–50 K ($\Delta v \sim 0.14$–0.18 km s^{-1}). This is evidence for small-scale clumps within the molecular cloud. Thus, the HCN maps provide strong evidence for large-scale clumps and suggestions of small-scale clumps in the molecular cloud around IRS 1 and IRS 2 which could thus provide the necessary density conditions for the complex maser excitation around IRS 1.

Figure 4 shows an enlarged picture of the region around IRS 1 and IRS 2. The solid contours around this region are HCN contours, and each number indicates the contour value in Jy per beam. The hatched circle is the size of IRS 2 as measured in the 23 GHz continuum by Henkel, Wilson, and Johnston (1984). Thus, the expansion of IRS 2 into the molecular cloud seems to have created a cavity of diameter 5×10^{17} cm in the dense material. The HCN contours outline the continuum size rather well. The larger size of IRS 2 could thus be due to the H II region expanding into a less dense medium. The contour around IRS 1 in the figure is the lowest contour of the 15 GHz map of Campbell (1984). IRS 1 also appears to be situated at the edge of the cavity around IRS 2 which may be an indication of sequential star formation.

IV. CONCLUSIONS

Interferometric observations of the emission from the three hyperfine lines of the $J = 1$–0 transition of hydrogen cyanide

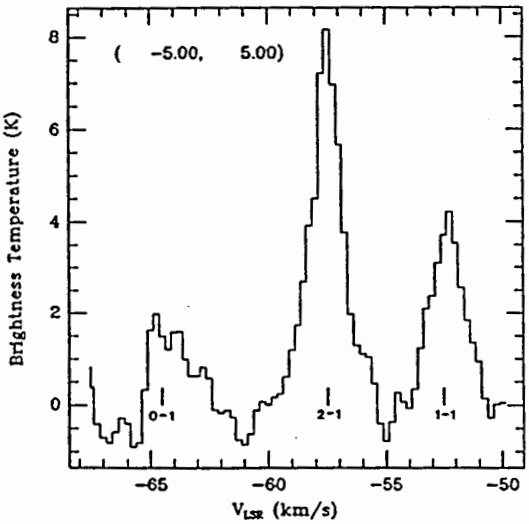

FIG. 3.—Spectrum of the $J = 1$–0 transition of HCN which is taken at a map position of $(\Delta\alpha, \Delta\delta) = (-5\overset{s}{.}0, 5\overset{s}{.}0)$ relative to $\alpha(1950) = 23^h11^m37^s$ and $\delta(1950) = 61°11'50''$. Vertical lines indicate the positions of the hyperfine components.

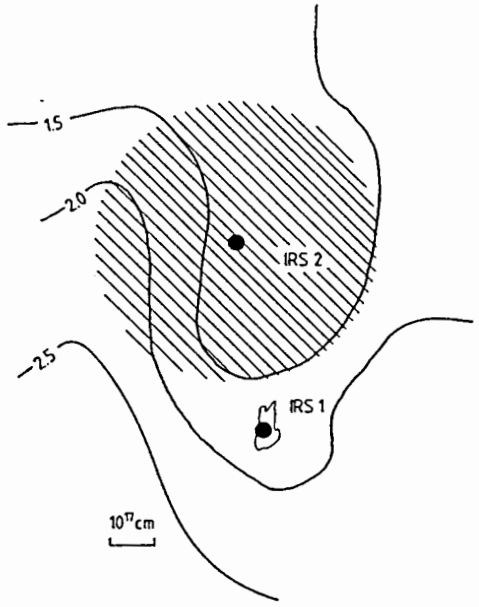

FIG. 4.—Solid contours show the average emission in the $J = 1$–0, $F = 2$–1 transition of HCN in the velocity interval $-61.0 \leq V_{LSR} \leq -55.0$ km s^{-1} (the numbers on the contours indicate their value in Jy per beam). Filled circles show the positions of the infrared sources IRS 1 and IRS 2. Hatched circle outlines the diameter of the H II region surrounding IRS 2 as measured at 23 GHz by Henkel, Wilson, and Johnston (1984). The contour around IRS 1 is the lowest contour of the 15 GHz continuum map of Campbell (1984).

show that the peak of the HCN emission is offset from any infrared source. There is a pronounced lack of emission around IRS 2 and to a lesser extent around IRS 1. Since the $J = 1$–0 transition of HCN requires neutral hydrogen (H_2) densities of $\geq 10^6$ cm^{-3} for excitation, the lack of HCN densities around IRS 1 and IRS 2 suggests lower H_2 densities in that region. The emission also appears highly clumped with evidence of even smaller scale density structures in the molecular cloud surrounding IRS 1 and IRS 2. Such small-scale structures are plausible if the H II regions expand into an inhomogeneous molecular cloud thus creating the small-scale density inhomogeneities required to explain the excitation of the different masers. The observed range of velocities in the HCN clumps corresponds to the range of maser velocities. Further observations at even higher resolution can be useful in providing a limit on the clump sizes in the molecular material around IRS 1, which would, in turn, provide a better trace of the maser emission regions. The continuum measurements reported in this paper support a two-component H II region model which consists of a compact core and extended halo. However, more measurements at frequencies above 15 GHz are needed before such a model can be accepted.

The density structure in HCN seems to agree with the requirements of the Boland and de Jong (1981) H_2CO maser excitation model in that the lack of HCN emission around IRS 1 puts an upper limit of less than 10^6 cm^{-3} on H_2 densities surrounding the H II region. The extended halo component of the H II region has an emission measure of 2.2×10^8 cm^{-6} pc

which falls within the range required by Boland and de Jong (1981).

This work has been supported by the Laboratory for Astronomical Imaging with funds provided for the Berkeley-Illinois-Maryland array project by the University of Illinois. We would like to acknowledge the cooperation of all the astronomers at the Radio Astronomy Laboratory at the University of California, Berkeley, who made remote observing with the Hat Creek Array possible. We would also like to thank Dr. M. C. H. Wright who helped us with the RALINT data reduction software system.

REFERENCES

Batrla, W., Matthews, H. E., Menten, K. M., and Walmsley, C. M. 1987, *Nature*, 326, 49.
Boland, W., and de Jong, T. 1981, *Astr. Ap.*, 98, 149.
Campbell, B. 1984, *Ap. J. (Letters)*, 282, L27.
———. 1985, in *Masers, Molecules and Mass Outflows in Star Forming Regions*, ed. A. D. Haschick (Haystack Observatory), p. 101.
Campbell, B., and Thompson, R. I. 1984, *Ap. J.*, 279, 650.
Dickel, H. R., Rots, A. H., Goss, W. M., and Forster, J. R. 1982, *M.N.R.A.S.*, 198, 265.
Downes, D., and Wilson, T. L. 1974, *Ap. J. (Letters)*, 191, L77.
Elitzur, M. 1985, in *Masers, Molecules and Mass Outflows in Star Forming Regions*, ed. A. D. Haschick (Haystack Observatory), p. 299.
Elitzur, M., and de Jong, T. 1978, *Astr. Ap.*, 67, 323.
Fischer, J., Righini-Cohen, G., Simon, M., Joyce, R. R., and Simon, T. 1980, *Ap. J. (Letters)*, 240, L95.
Forster, J. R., Goss, W. M., Gardner, F. F., and Stewart, R. T. 1985, *M.N.R.A.S.*, 216, 35P.
Forster, J. R., Graham, D., Goss, W. M., and Booth, R. S. 1982, *M.N.R.A.S.*, 201, 7P.
Forster, J. R., Welch, W. J., Wright, M. C. H., and Baudry, A. 1978, *Ap. J.*, 221, 137.
Gardner, F. F., and Martin-Pintado, J. 1983, *Astr. Ap.*, 121, 265.
Gardner, F. F., Whiteoak, J. B., Forster, J. R., Pankonin, V. 1986, *M.N.R.A.S.*, 218, 385.
Genzel, R., and Downes, D. 1976, *Nature*, 262, 564.
Guilloteau, S., and Lucas, R. 1981, *Astr. Ap.*, 101, L19.
Hackwell, J. A., Grasdalen, G. L., and Gehrz, R. D. 1982, *Ap. J.*, 252, 250.
Henkel, C., Wilson, T. L., and Johnston, K. J. 1984, *Ap. J. (Letters)*, 282, L93.
Israel, F. P., Habing, M. J., and de Jong, T. 1973, *Astr. Ap.*, 27, 143.
Madden, S. C., Irvine, W. M., Matthews, H. E., Brown, R. D., and Godfrey, P. D. 1986, *Ap. J. (Letters)*, 300, L79.
Martin, A. M. H. 1973, *M.N.R.A.S.*, 163, 141.
Martin-Pintado, J., Wilson, T. L., Gardner, F. F., and Henkel, C. 1985, *Astr. Ap.*, 142, 131.
Mauersberger, R., Wilson, T. L., and Henkel, C. 1986, *Astr. Ap.*, 160, L13.
Menten, K. M., Reid, M. J., Moran, J. M., Wilson, T. L., Johnston, K. J., and Batrla, W. 1988, *Ap. J. (Letters)*, 333, L83.
Norris, R. P., Booth, R. S., Diamond, P. J., and Porter, N. D. 1982, *M.N.R.A.S.*, 201, 191.
Olnon, F. M. 1975, *Astr. Ap.*, 39, 217.
Palmer, P., Gardner, F. F., and Whiteoak, J. B. 1984, *M.N.R.A.S.*, 211, 41P.
Rots, A. H., Dickel, H. R., Forster, J. R., and Goss, W. M. 1981, *Ap. J. (Letters)*, 245, L15.
Scoville, N. Z., Sargent, A. I., Sanders, D. B., Claussen, M. J., Masson, C. R., Lo, K. Y., and Phillips, T. G. 1986, *Ap. J.*, 303, 416.
Urry, W. L., Thornton, D. D., and Hudson, J. A. 1985, *Pub. A.S.P.*, 97, 745.
Whiteoak, J. B., and Gardner, F. F. 1983, *M.N.R.A.S.*, 205, 27P.
Wilson, T. L., and Snyder, L. E. 1985, *Ap. J. (Letters)*, 290, L63.
Wynn-Williams, C. G., Becklin, E. E., and Neugebauer, G. 1974, *Ap. J.*, 187, 473.

WOLFGANG BATRLA, PREETHI PRATAP, and L. E. SNYDER: Astronomy Department, University of Illinois, 349 Astronomy Building, 1011 W. Springfield Avenue, Urbana, IL 61801

APPENDIX C

THE ASTROPHYSICAL JOURNAL, 351:530–537, 1990 March 10

HIGH-RESOLUTION MOLECULAR OBSERVATIONS OF NGC 7538 IRS 1

P. PRATAP, W. BATRLA,[1] AND L. E. SNYDER
Astronomy Department, University of Illinois
Received 1989 June 5; accepted 1989 September 11

ABSTRACT

High-resolution observations (3″) of the $J = 1$–0 transitions of HCO^+ and HCN toward NGC 7538 IRS 1 have been made with the Berkeley-Illinois-Maryland Array and the NRAO 12 m telescope. The HCO^+ emission traces the high-velocity outflow which appears to originate about 15″ south of IRS 1, at the center of an elongated structure which is seen at higher velocities. The axis of the outflow is at a position angle of 145° (east of north), and only the blue lobe of the outflow is seen. The direction of the high-density outflow agrees very well with the direction of the CO outflow, although the CO outflow is more extended.

The general structure of the HCN and HCO^+ emission at the quiescent velocity of the source is very similar. Both molecules trace a density enhancement which outlines a cavity, of diameter 0.09 pc, in the cloud around the H II region. The cavity is interpreted as a lack of high-density material which is caused by the expansion of the H II region. The expansion also creates the density enhancement in the material surrounding the cavity, which is clearly traced by the HCN and HCO^+ emission. The high-resolution observations show that this density enhancement is very clumpy. A detailed comparison between individual HCN and HCO^+ emission peaks shows a definite anticorrelation, which is an indication of the different mechanisms which excite the two molecules.

The molecular cloud is also seen to consist of high-density clumps. The distribution of the deconvolved clump sizes shows that the HCO^+ clumps are resolved by the 3″ beam and that the distribution is Gaussian with a peak at a clump size of 0.12 pc (assuming a distance of 3.5 kpc to the source). The HCN clump size distribution peaks at 0.08 pc. The existence of HCN clumps at the limit of the resolution could be an indication of smaller clumps in the cloud.

Subject headings: interstellar: molecules — nebulae: H II regions — nebulae: individual (NGC 7538) — nebulae: internal motions — nebulae: structure

I. INTRODUCTION

Detailed observations with synthesis telescopes have proven invaluable for understanding various aspects of molecular emission in regions of star formation. NGC 7538 is one example of a region of star formation which consists of a group of three infrared sources, all identified as compact H II regions, embedded in the dense molecular material at the interface between the molecular cloud and a visible H II region. A bipolar outflow of the type that seems to be a characteristic phenomenon in young star-forming regions was detected toward NGC 7538 IRS 1 in the $J = 1$–0 transition of CO (Campbell and Thompson 1984) and was studied further by Fischer *et al.* (1985) and Scoville *et al.* (1986). These studies concluded that the outflow was associated with the ultracompact H II region IRS 1. Batrla, Pratap, and Snyder (1988; hereafter Paper I) studied the source in the $J = 1$–0 transition of HCO^+. Strong blueshifted line wings were detected, and it was found that the direction of the HCO^+ outflow was in perfect alignment with the direction of the CO outflow. Since HCO^+ is indicative of H_2 densities which are about two orders of magnitude higher than those traced by CO, and since HCO^+ has been found to be a good tracer of high-velocity material, it can be assumed that the HCO^+ emission traces the structure of the high-density, high-velocity material closer to the outflow source than that traced by CO. These HCO^+ maps strongly suggest that the source of the large-scale outflow, observed in CO and HCO^+, is not the ultracompact H II region, IRS 1, but instead another source about 15″ south of IRS 1. This interpretation is supported by the detection of an elongated structure in the HCO^+ emission (Paper I), which is perpendicular to the direction of the outflow and centered at the origin of the outflow. A similar extended feature was also observed in the HCN ($J = 1$–0) emission (Pratap, Batrla, and Snyder 1989, hereafter Paper II). If the large-scale outflow actually does originate 15″ south of IRS 1, it is not causally connected to the ionized outflow from IRS I, seen at small scales in Campbell's (1984*a*) 2 cm continuum map. If the two outflows are indeed spatially separated, it is no longer necessary to assume an apparent direction change between the small (Campbell 1984*a*) and large-scale motions of the gas, as has been proposed by Kameya *et al.* (1989).

Although NGC 7538 IRS 1 appears to be a typical star-forming region, it is indeed unusual because the formaldehyde (H_2CO) maser has been observed only here and in Sgr B2. The molecular cloud associated with NGC 7538 IRS 1 has two H_2CO maser spots, which are situated in front of an ultracompact H II region (Rots *et al.* 1981; Dickel *et al.* 1982; Campbell 1984*a*) and which appear to be amplifying the continuum emission from IRS 1. IRS 1 is also the site of maser emission from OH, H_2O, CH_3OH, NH_3, and $^{15}NH_3$, which are discussed in Paper II. The density conditions required by the Boland and de Jong (1981) model for the H_2CO maser excitation were examined in Paper II via maps of the $J = 1$–0 transition of HCN. These maps show a hole in the emission around IRS 1 which is consistent with the maser excitation requirements of the model, because it suggests that $n(H_2) < 10^6$ cm^{-3}.

This paper presents new, higher resolution (~3″) HCN and HCO^+ results which were made with both the Hat Creek

[1] Currently at the National Radio Astronomy Observatory, Green Bank.

Millimeter Array and the NRAO[2] 12 m telescope. The increased angular resolution confirms the clumpy nature of the molecular cloud which was suggested by the HCN line widths in Paper II. The 12 m observations were used to fill in the short spacings in the u, v plane and thus measure the flux from the extended structure of the molecular cloud. These improved maps allow a better comparison of the HCN and HCO^+ emission structures which will be useful in studying the differences in their chemistry and their excitation mechanisms.

II. OBSERVATIONS

Interferometric observations tracking the position $\alpha(1950) = 23^h11^m37^s$, $\delta(1950) = 61°11'50''$, which is near the IRS 1 position, were performed with the Hat Creek Millimeter Array during the period from 1985 October to 1988 May. The correlator configuration used for the HCN $J = 1$–0 line observations has been described in Paper II. The correlator configuration for the HCO^+ observations also contained lines of $H^{13}CN$, SO, SO_2, SiO, and ^{29}SiS. The upper and lower sidebands were each divided into four spectral segments of 64 channels. The frequency resolution of 0.16 MHz resulted in a velocity resolution of 0.5 km s^{-1}. The HCO^+ ($J = 1$–0) line at 89.18852 GHz was contained in one of the spectral segments of the upper sideband. The instrumental phase was calibrated against the quasar BL Lac at approximately 35 minute intervals. The RF passband shape and the flux density scale were calibrated using observations of the quasar 3C 84.

Short spacing u, v data were derived from single-dish measurements made with the NRAO 12 m telescope at Kitt Peak in 1988 March. The full width at half-maximum (FWHM) of the 12 m telescope beam was 70″. The HCN and HCO^+ observations consisted of a 7 × 7 grid of measurements centered on $\alpha(1950) = 23^h11^m37^s$, $\delta(1950) = 61°11'50''$. The points were separated by 30″, and the frequency resolution was 100 kHz per channel. After a baseline was subtracted from the single-dish spectra, the data were transformed into the interferometer format using the RALINT data reduction package. The first step was to convert the Kitt Peak antenna temperature, T_R^*, into flux density. Next, the single-dish beam, which was assumed to be a symmetric Gaussian of 60″ × 60″, was deconvolved from the data giving an estimate of the true sky brightness distribution. This brightness distribution was then convolved with the primary beam of the interferometer antennae (FWHM ~ 2′.1), and model u, v visibilities were calculated. The model visibilities corresponded to u, v spacings ranging from 0.09 to 1.3 kλ. The derived u, v data retained the frequency resolution of the original single-dish spectra. Model and interferometer u, v data were then concatenated into one data set.

The combined sets of visibility data for each line were gridded, convolved, and Fourier transformed to obtain a cube of 256 × 256 × 45 maps with a pixel size of 1″ and a velocity resolution of 0.5 km s^{-1}. The visibilities were first weighted uniformly (which weights the data by the density of points within each grid cell in the u, v plane) and then by the square of the system temperature. The full width at half-maximum of the resulting synthesized beam was 3″.9 × 2″.7 for the HCO^+ maps and 3″.0 × 2″.8 for the HCN map. The maps were then CLEANed, resulting in an rms noise level in a single channel map of about 0.25 Jy $beam^{-1}$ for the HCN and 0.20 Jy $beam^{-1}$ for the HCO^+ maps.

[2] The National Radio Astronomy Observatory is operated by Associated Universities, Inc., under cooperative agreement with the National Science Foundation.

III. RESULTS AND DISCUSSION

a) HCO^+ Results

Figure 1 presents a set of channel maps across the $J = 1$–0 transition of HCO^+. The detailed velocity structure of the emission can be seen in these maps which are centered at $\alpha(1950) = 23^h11^m37^s$, $\delta(1950) = 61°11'35''$. The three solid triangles indicate the positions of IRS 1, IRS 2, and IRS 3. The panel corresponding to a velocity of −57.5 km s^{-1} contains the FWHM of the synthesized beams associated with the two sets of contours in the maps. The bold contours represent the maps which have been made by convolving the high-resolution maps to a beam of 8″.5 × 6″.7, which is the resolution of the maps presented in Paper I.

The maps corresponding to velocities of −57.5 and −58.0 km s^{-1} show the elongated structure reported in Paper I, which is centered about 15″ south of IRS 1 and extends from the northeast to the southwest. However, the smooth elongated feature of the low-resolution data (which is seen in the bold contours) is now resolved into a large number of small clumps. In the map corresponding to a velocity of −57.5 km s^{-1}, the clumps appear to be distributed preferentially in the elongated structure. The elongated structure does not appear to be rotating, because there is no appreciable velocity gradient along the major axis. The channel map at a velocity of −57.5 km s^{-1} shows that most of the stronger clumps are situated at the edges of the elongated structure. At a velocity of −58.5 km s^{-1}, the clumps seem to have moved to the center of the structure. This position shift implies that the clumps near the center of the structure have lower velocities than the clumps at the edges. Such a velocity shift could be caused by radial motions (or an expansion) in the disk. At velocities of −58.0 and −58.5 km s^{-1}, the strongest emission peaks appear most prominently to the southeast and south of the H II region. At lower velocities, starting at a velocity of −59.0 km s^{-1}, the clumps separate into two groups on the northwest and southeast of IRS 1. A group of clumps in a direction perpendicular to the elongated structure can be seen in the maps corresponding to −59.5 and −60.0 km s^{-1}. It is this group of clumps that shows up in the low-resolution maps as a blue component of the outflow.

The presence of the outflow can be clearly seen in Figure 2, which shows a raster of HCO^+ spectra. The velocity and intensity scales are shown in the lower left-hand corner. The spectra trace the elongated structure which was seen in the channel maps, while to the northwest, the blue outflow lobe becomes very pronounced. The presence of the outflow can be seen clearly in the shift of the line peak toward more negative velocities. The structure of the emission at the lower velocities indicates the presence of an outflow. There is no clear evidence for a red component of the outflow. The maps agree very well with the results presented in Paper I.

The outflow in this source has been studied in the $J = 1$–0 transition of CO by several authors. Fischer *et al.* (1985) showed that the outflow was oriented at a position angle of 145° with a separation between the red and blue lobes of about 44″. This was confirmed by Scoville *et al.* (1986), whose CO observations had a resolution of 7″. The continuum map at 15 GHz, made by Campbell (1984*a*) with a resolution of 0″.1, showed evidence for an ionized outflow in the north-south

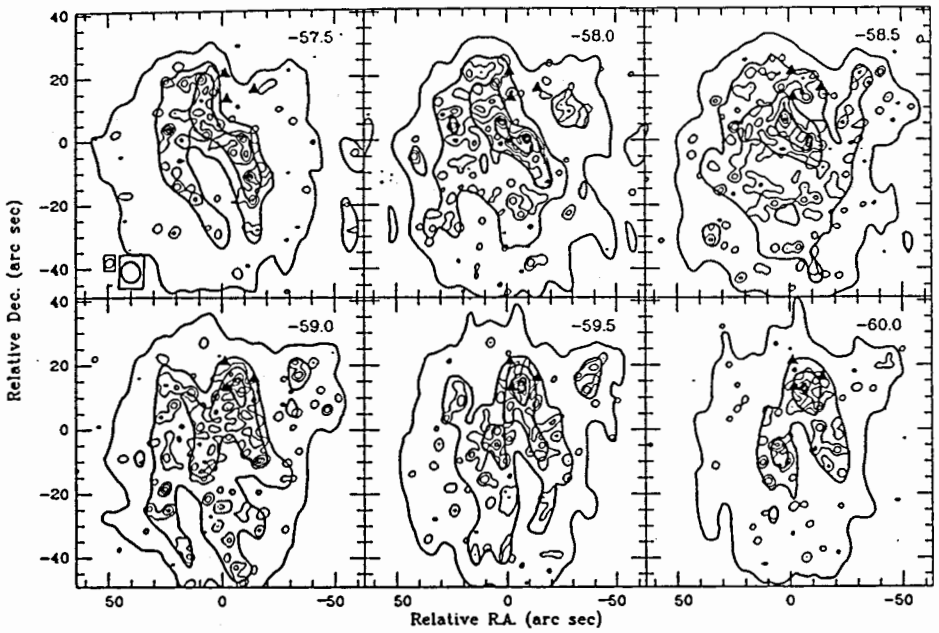

FIG. 1.—Channel maps across the $J = 1$–0 transition of HCO^+. The high-resolution contours are at intervals of 1.0, 1.5, 2.0, 2.25, 2.5, 2.75, 3.0, 3.25, and 3.5 Jy beam^{-1}. The contours correspond to a resolution of 3.9 × 2.7. The bold contours are maps which have been made by convolving the high resolution data to a beam of 8.5 × 6.7. The contours are at intervals of 0.5, 0.8, 1.1, 1.4, and 1.6 Jy beam^{-1}. The panel corresponding to a velocity of −57.5 km s^{-1} contains the FWHM of the synthesized beams associated with of the two sets of contours. The (0, 0) pixel position of each map is at $\alpha(1950) = 23^h11^m37^s$, $\delta(1950) = 61°11'35''$. The three solid triangles correspond to the positions of IRS 1, IRS 2, and IRS 3 [IRS 1: $\alpha(1950) = 23^h11^m36^s.7 \pm 0.2$, $\delta(1950) = 61°11'48'' \pm 1$; IRS 2: $\alpha(1950) = 23^h11^m36^s.8 \pm 0.2$, $\delta(1950) = 61°11'56'' \pm 1$; IRS 3: $\alpha(1950) = 23^h11^m35^s.0 \pm 0.2$; $\delta(1950) = 61°11'51'' \pm 1$; Hackwell, Grasdalen, and Gehrz 1982].

direction. The difference in the orientation of the outflow from small scales to the large scales was explained by Kameya *et al.* (1989) by invoking density enhancements to the northeast and southwest of IRS 1. HCO^+ traces densities that are about two orders of magnitude higher than CO, and it has been found to be a good tracer of high-velocity material, so the HCO^+ emission probes the high-velocity material closer to the source of the outflow and thus provides a better position for the origin of the outflow. The channel maps presented here in Figure 1 show that the orientation of the HCO^+ outflow is at the same position angle as the CO outflow. However, the origin of the outflow is definitely to the south of IRS 1, which can be seen in the maps corresponding to velocities of −59.0, −59.5, and −60.0 km s^{-1}. In addition, the direction of the outflow is perpendicular to the elongated structure which is seen in HCO^+ at −57.5 km s^{-1}. The evidence presented by the HCO^+ results points to the presence of another source as the origin of the outflow, but no such source has been observed in the infrared. However, the low-resolution maps across the $J = 1$–0 transition of HCN, presented in Paper II, show a peak of emission to the south of IRS 1 which is situated at the center of the elongated HCO^+ structure. This peak of emission can also be seen in the high-resolution HCN maps corresponding to velocities of −57.0, −57.5, −58.0, and −58.5 km s^{-1} in Figure 3. Both the HCO^+ and the HCN results point to the presence of high-density clumps in the vicinity of the outflow source. So the source of the outflow is either of very low luminosity or it is a young source undergoing a considerable amount of extinction.

b) HCN *Results*

Figure 3 presents a set of contour maps across the HCN $J = 1$–0 line, which are centered at $\alpha(1950) = 23^h11^m37^s$; $\delta(1950) = 61°11'50''$. The FWHM of the synthesized beam can be seen in the upper left-hand corner of the map corresponding to a velocity of −57.0 km s^{-1}. The maps demonstrate the clumpy nature of the molecular cloud. The strongest peaks are situated to the south and east of IRS 1. The distribution of these peaks is consistent with the emission structure of the maps in Paper II. In the map corresponding to velocities of −57.5 and −58.0 km s^{-1}, the clumps are strung around the H II regions. The cavity in the emission, which was discussed in Paper II, is defined clearly in these maps.

The discussion of the emission in the $J = 1$–0 transition of HCN in Paper II was done with reference to the maser emission (in particular, the unusual formaldehyde maser) associated with IRS 1. The paper described the various masers that have been observed toward IRS 1 and how they appear to be situated at the interface between the expanding H II region and the molecular cloud. This interface is outlined by the density enhancement which was seen in the HCN emission. When the

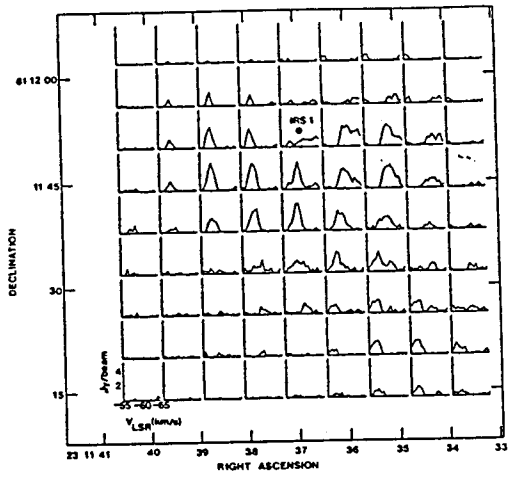

FIG. 2.—A raster of HCO^+ spectra showing the elongated emission structure stretching from the northeast to the southwest and the blueshifted outflow toward the northwest. The approximate position of IRS 1 is marked by the filled circle. The spectrum in the lower left-hand corner shows the velocity and intensity scales. It is evident that the peak of the spectra along the elongated structure is greater than -60.0 km s^{-1}, while the position of the peak to the northwest (at about $\alpha = 23^h11^m35^s$ and $\delta = 61°11'45''$) is shifted to more negative velocities.

expansion takes place in a molecular cloud with a clumpy structure, the density enhancement around the H II region retains the uneven density structure. This provides the different densities required for the inversion of the various maser transitions. The presence of the cavity, indicated by a lack of HCN emission, is interpreted as a lack of high-density material around IRS 1 which, in turn, provides an upper bound for the density in the cavity. In the high-resolution maps (Fig. 3), the cavity is more pronounced, and the molecular material defines a sharp edge to the southeast of IRS 1, which is most clearly seen in the maps corresponding to -57.5 and -58.0 km s^{-1}. The cavity in the HCN emission and the density enhancement surrounding the H II region are clearly defined with the 3″ beam; assuming a distance of 3.5 kpc to the source, the cavity has a diameter of 0.09 pc ($\sim 2 \times 10^{17}$ cm) and extends to the south of IRS 1.

Figure 4 presents a map of the emission in the $J = 1$–0 transition of HCN (integrated over the velocity interval -58.0 to -57.0 km s^{-1}) overlaid on a gray-scale image of the optical emission around the infrared sources. The optical image is taken from the red plate of the Palomar Observatory Sky Survey (Klinglesmith and Hollis 1987). The figure shows the anticorrelation between the optical emission and the high-density molecular cloud which is indicated by the HCN emission. The optical emission appears to reach into the cavity in the high-density material around IRS 1 and IRS 2. This supports the conclusion that the cavity is indeed caused by lack of high-density material in the region immediately surrounding the H II regions.

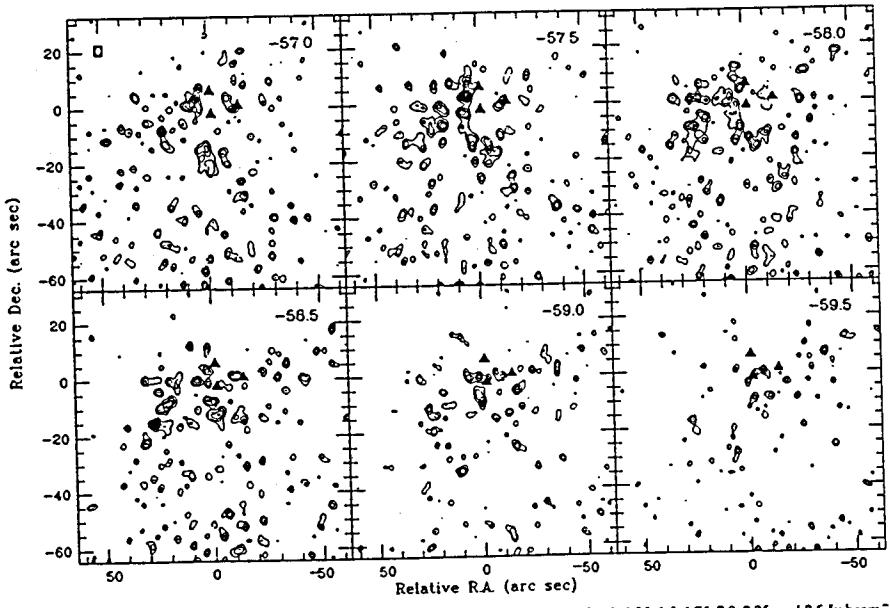

FIG. 3.—Channel maps across the $J = 1$–0 transition of HCN. The contours are at intervals of 0.75, 1.0, 1.25, 1.5, 1.75, 2.0, 2.25, and 2.5 Jy beam^{-1}. The FWHM of the beam is indicated in the upper left-hand corner of the map, corresponding to a velocity of -57.0 km s^{-1}. The three solid triangles correspond to the positions of IRS 1, IRS 2, and IRS 3. The (0, 0) pixel position of each map is at $\alpha(1950) = 23^h11^m37^s$, $\delta(1950) = 61°11'50''$.

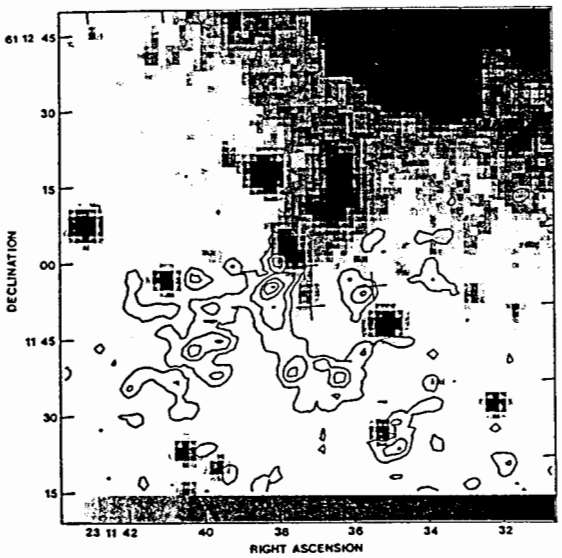

FIG. 4.—An overlay of HCN contours on an optical image taken from the red plate of the Palomar Observatory Sky Survey. The gray scale ranges from 65 (*light grey*) to 300 (*dark grey*) flux units. The HCN contours have been summed over a velocity interval between −57.0 and −58.0 km s^{-1}. The contour levels are at 1.875, 2.625, 3.375, 4.125, and 4.875 Jy beam^{-1}. The positions of IRS 1, IRS 2, and IRS 3 are indicated by the three crosses.

c) *A Comparison Between* HCN *and* HCO^+ *Emission*

Figure 5 is a comparison of the HCO^+ and HCN emission around IRS 1. The gray scale is the HCO^+ and the contours correspond to the HCN emission. Both maps are sums integrated over the velocity interval -58.0 km s^{-1} $< V_{LSR} <$ -57.0 km s^{-1}. The HCO^+ emission, which has a peak value of 6.5 Jy beam^{-1}, is not significantly stronger (within calibration errors) than the HCN emission which has a peak value of 5 Jy beam^{-1}. However, the strongest HCN peak is situated to the northeast of IRS 1, while the strongest HCO^+ peak is to the southwest of IRS 1. Both molecules show the clumps around IRS 1 and IRS 2 which clearly outline the cavity in the molecular cloud. The fact that the cavity is seen in both the HCN and HCO^+ emission provides strong evidence for the interpretation that the lack of emission is due to a lack of high-density material. The HCO^+ emission follows the HCN emission rather closely in the general structure of the emission. Since both molecules trace the high-density material in the cloud, the emission could correspond to the density enhancement caused by the expansion of the compact H II regions into the molecular cloud.

A detailed comparison of the positions of the individual peaks of the HCN and the HCO^+ emission shows no correlation (Fig. 5). Such an anticorrelation has been seen before in Orion, by Vogel *et al.* (1984). The beam size in their maps is about 18″, but since Orion is about 6 times closer than NGC 7538, their absolute scale is roughly the same as the scale of the maps presented here. The explanation offered by Vogel *et al.* (1984) for the observed difference is that the HCO^+ and the HCN emission arise from different but adjacent parts of the molecular cloud. In the case of NGC 7538 IRS 1, a possible explanation could be that a shock front or an ionization front from the H II region is expanding into the clumpy molecular cloud. This, in turn, could cause high ionization levels in the clumps it hits first, ultimately resulting in the HCO^+ emission. The neutral clumps would then show the HCN emission. Such an explanation assumes that both HCN and HCO^+ are optically thin. This explanation is further supported by the fact that the HCN clumps are, in general, smaller than the HCO^+ clumps (as discussed in § IV*d*) and thus could be a probe of the dense cores of the clumps. There is also no evidence for HCN emission in the outflow region (which is to the northwest of IRS 1). Since HCN and HCO^+ trace similar densities, this implies that the HCO^+ emission in the outflow region is due to an abundance enhancement of HCO^+ relative to HCN rather than a density variation. Such abundance enhancements are consistent with the results for a similar emission structure in Orion seen by Vogel *et al.* (1984).

Figures 6*a* and 6*b* show the HCN and HCO^+ spectra around the position $\alpha(1950) = 23^h11^m37^s.6$, $\delta(1950) = 61°11'52''.5$. This position corresponds to the strongest peak in the HCN emission (Fig. 6*a*). The spectra are spaced at 1 pixel intervals. The narrow line widths of the lines ($\sim$1.5 km s^{-1}) can be compared to the line width in Figure 3 of Paper II ($\sim$2.5 km s^{-1}). The presence of clumps in the high-resolution maps clearly indicates that the wider line width was caused by clumping in the 9″ beam. The width of the spectrum at the position of the strongest peak ($\sim$1.0 km s^{-1}, which may be underresolved at a resolution of 0.5 km s^{-1}), combined with the pointlike nature of the clump and the apparent non-LTE intensity ratio of the HCN hyperfine components, provide an indication of the possible nonthermal excitation in this line.

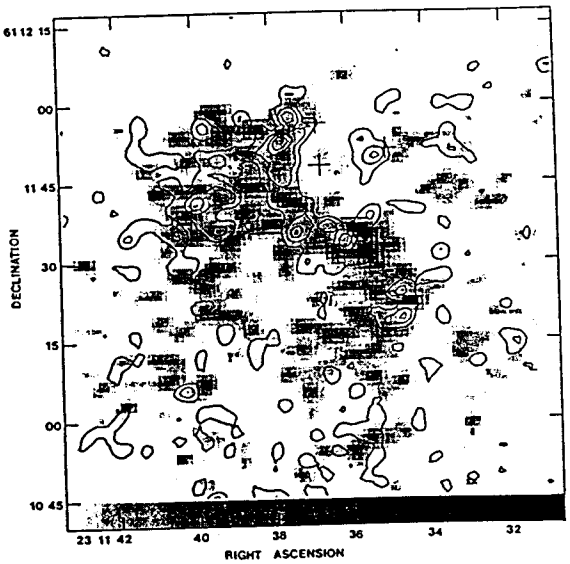

FIG. 5.—Integrated HCN contours overlaid on an integrated gray-scale map of HCO^+ emission. Both the maps are sums integrated over the velocity interval $-58.0\ km\ s^{-1} < V_{LSR} < -57.0\ km\ s^{-1}$. The gray scale covers a flux range from 1.875 Jy beam^{-1} (*light grey*) to 6.5 Jy beam^{-1} (*dark grey*). The HCN contours are at intervals of 1.875, 2.625, 3.375, 4.125, and 4.875 Jy beam^{-1}. The three crosses indicate the positions of IRS 1, IRS 2, and IRS 3.

The HCO^+ spectra in the same region also appear to show the same narrow line widths at the position of the HCN peak. In addition, the HCO^+ spectra also have extended line wings, which indicates gas motion in the cloud.

d) Small-Scale Clumps

The channel maps across the HCO^+ and the HCN lines indicate that the molecular cloud surrounding IRS 1 is very clumpy. With the large number of clumps seen in these maps, it is possible to study the statistical behavior of some of the clump parameters. The clumps were selected from peaks in single-channel maps. The criterion for the selection was that the peak value was at least 6 σ ($\sim$1.2 Jy beam^{-1}). The adjacent velocity channels were then examined and only those clumps that were seen over at least two velocity channels ($\sim$1.0 km

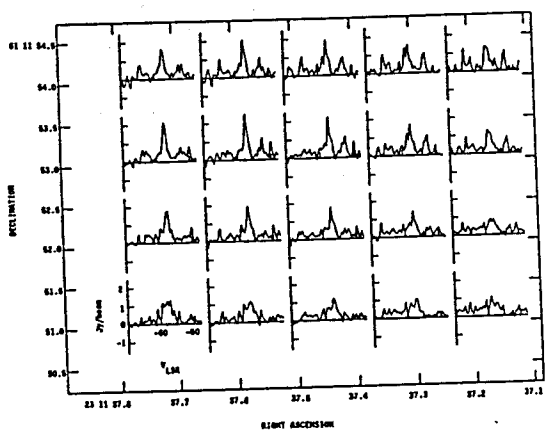

FIG. 6a

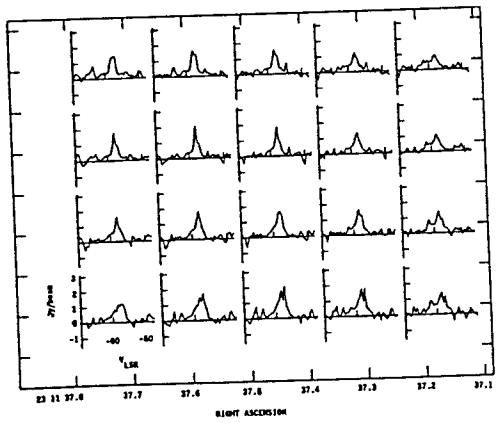

FIG. 6b

FIG. 6.—(*a*) A raster of HCN spectra around the position $\alpha(1950) = 23^h11^m37^s.8$, $\delta(1950) = 61°11'52''.5$, which corresponds to the strongest peak in the HCN emission. The increment along the abcissa is 0.1, and the increment along the ordinate is 1". IRS 1 is off the scale of the plots, to the southwest. (*b*) A raster of HCO^+ spectra around the HCN peak. The spectra have been plotted at the same positions as the HCN spectra in (*a*).

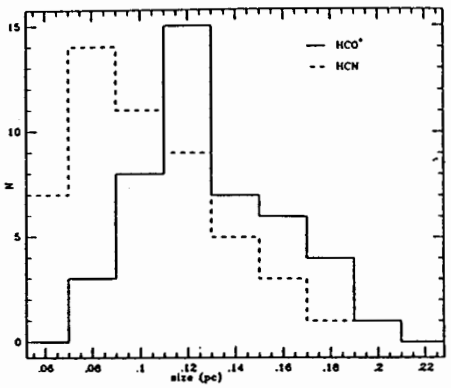

FIG. 7.—Histograms of the HCO^+ clump sizes (*solid line*) and HCN clump sizes (*dashed line*). Sizes are in parsecs, assuming a distance of 3.5 kpc to the source.

s^{-1}) were taken. These selection criteria led to 44 clumps from the HCO^+ maps and 53 clumps from the HCN maps. The sizes of the clumps were measured by fitting a two-dimensional Gaussian to the channel of the peak emission in order to determine the deconvolved width. The clump size used in the statistical analysis was an average of the major axis and minor axis of the fitted Gaussian. The V_{LSR} and deconvolved line width of each clump were measured by fitting Gaussians to the spectra at the peak position of each clump. Figure 7 shows histograms of the sizes of the clumps measured in HCN (*dashed line*) and HCO^+ (*solid line*). The clump sizes are in parsecs (assuming a distance of 3.5 kpc to the source). The HCO^+ clump sizes follow a near-Gaussian distribution with a mean of 0.124 pc and a standard deviation of 0.028. The 95% confidence interval for the mean is between 0.115 pc and 0.133 pc. The fact that there are no HCO^+ clumps at the size of the beam (which defines the left edge of the plot) demonstrates that the HCO^+ clumps are resolved by the 3″ beam. The HCN distribution does not appear Gaussian, and the presence of HCN clumps at the beam size indicates that there are clumps which are still unresolved. The separation between the peaks of the two distributions indicates that the HCN samples the molecular condensations which are smaller than those sampled by HCO^+. This is understandable, because HCN probes densities an order of magnitude higher than the densities probed by HCO^+.

The main uncertainty in the absolute values for the clump sizes lies in the uncertainty in the distance to NGC 7538. Distance estimates to the source vary from 2.8 kpc (Crampton, Georgelin, and Georgelin 1978; Campbell 1984*b*) to 3.5 kpc (Israel, Habing, and de Jong 1973). The upper limit on the HCN clump sizes in the cloud thus ranges from 1.4×10^{17} to 1.7×10^{17} cm, depending on the distance assumed for the source. Although this would cause an uncertainty in the value of the mean of the distribution, the shape of the distribution would remain unchanged.

Estimates for the masses of these dense cores can be derived from the clump sizes by assuming spheres with constant density. The density was taken to be the critical number density of hydrogen molecules at which the transition thermalized, which is 3×10^6 cm^{-3} for the HCN $J = 1$–0 line and 2×10^5 cm^{-3} for the HCO^+ transition. The masses of the HCN clumps ranged from about 7 to 350 $M_\odot$ (assuming a distance of 3.5 kpc to the source), although most of the clumps had masses between 10 and 50 $M_\odot$. The HCO^+ clumps ranged from about 2 to 40 $M_\odot$, with most of the clumps having masses between 2 and 15 $M_\odot$. The uncertainty in the distance to the source can introduce large changes in the mass estimates. For example, they are reduced by a factor of 0.6 if the smaller distance is assumed for the source. Therefore, these numbers must be taken as upper limits to the clump masses in the cloud. Nevertheless, the derived masses show that the interaction of the compact H II regions with the parent molecular cloud could lead to the formation of a cluster of low- and medium-mass stars.

The statistical analysis was extended to examine the data for correlations between the line width and the clump size. Several previous studies (Larson 1981); Leung, Kutner, and Mead 1982; Myers 1983) have found that a power-law correlation exists between the line widths and the clump size. The data presented here do not show any evidence for such a correlation. In fact, the clump sizes are consistently smaller than those predicted by Larson for a given line width. Such a deviation has also been found by Martin-Pintado *et al.* (1985) from observations of H_2CO in several molecular clouds. There are several possible explanations for this lack of correlation. One possibility is that the correlation between clump size and line width breaks down at small clump sizes. It is also possible that the lack of correlation is caused by the proximity of the clumps to the H II region, because the ambient pressure around H II regions is higher than in the general molecular cloud material. Also, an inherent assumption in all the models predicting the correlation is that the column density is constant across the cloud. Therefore, a variation of the column density from clump to clump could also be responsible for the lack of correlation, because the virial relationship (i.e., $GM \sim 2\Delta v^2 L$) together with the constancy of column density are equivalent to the proportionality of Δv to L^n, with $0.38 \leq n \leq 0.6$ (Wilson and Walmsley 1989, and references therein). Some of these possibilities can be examined by mapping the source in a molecule which traces lower densities and hence would be a measure of the bigger clumps in the cloud. Detection of a wider range of clump sizes would be useful in understanding the behavior of such clumps around H II regions.

IV. CONCLUSIONS

The clumpy nature of the molecular cloud which was suggested by the HCN line widths in Paper II is confirmed by the high-resolution maps toward NGC 7538 IRS 1 reported in this paper. The $J = 1$–0 transition of HCO^+ shows an elongated structure extending from the northeast to the southwest. Maps made with a 3″ beam have shown that the emission from both molecules is very clumpy. The wings of the HCO^+ line show the blue lobe of an outflow which is in the same direction as the CO outflow in the source. There is no evidence of a red lobe for the outflow. The origin of the outflow is situated about 15″ south of IRS 1, at the center of the elongated structure. Although no infrared source has been detected at this position, the HCN maps show a high-density clump at this position. It is possible that the outflow source is highly obscured. The HCN maps (Fig. 3) show that the emission clearly outlines the cavity in the molecular cloud around IRS 1, as was postulated in Paper II. The cavity has a diameter of 0.09 pc ($\sim 2 \times 10^{17}$ cm).

A comparison of the HCN and HCO^+ emission shows that both the molecules trace the density enhancement at the southeast edge of the cavity created by the expansion of the H II region into the surrounding molecular cloud. The molecular emission shows a series of clumps strung in an arc to the southeast of the H II region. On a small scale, the emission peaks of the two molecules do not coincide. This is an indication of the different mechanisms which excite the two molecules. The lower limit on the clump sizes, which is between 1.4×10^{17} and 1.7×10^{17} cm (corresponding to distance estimates to the source of 2.8 to 3.5 kpc), is determined by the resolution. The HCO^+ clumps are generally larger than the HCN clumps and appear to be resolved by the 3" beam. The distribution of the HCN clumps suggests the existence of even smaller clumps in the cloud. An estimate of the clump masses shows that most of the HCO^+ clumps have masses between 2 and 15 $M_\odot$ (assuming a distance of 3.5 kpc to the source), while most of the HCN clumps have masses between 10 and 50 $M_\odot$.

In the context of the maser emission that has been observed in the source, the clumps around the H II region can provide the different conditions required for the excitation of different molecular masers. The lack of emission around the H II region is seen in both HCN and HCO^+, which indicates that the material in the cavity is of a lower density than the surrounding molecular cloud. This conclusion is further supported by the fact that optical emission is seen in the cavity. Thus, the HCN and HCO^+ results provide an upper bound for the density of the material in the cavity and provides support for the density requirements of the Boland and de Jong model for the H_2CO maser. Deguchi and Watson (1989) have proposed a maser beaming model which requires small-scale clumps which have linear dimensions of the order of $\sim 10^{15}$ cm. Although the scale of the clumps presented in this paper is $\sim 10^{17}$, the existence of clumps whose dimensions are at the limit of the resolution suggests the presence of the small-scale clumps which are required by their model. Observations of a molecular species that traces lower densities than HCN and HCO^+ could give a lower bound on the densities in the cavity.

This work has been supported by the Laboratory for Astronomical Imaging, with funds provided for by the Berkeley-Illinois -Maryland-Array project by the University of Illinois. We would like to acknowledge the cooperation of all the astronomers at the Radio Astronomy Laboratory at the University of California, Berkeley, who made remote observing with the Hat Creek Array possible. We would also like to thank R. Loushin, who was responsible for obtaining the data from the NRAO 12 m telescope, and Belva G. Campbell, for helpful suggestions.

REFERENCES

Batrla, W., Pratap, P., and Snyder, L. E. 1988, *Ap. J. (Letters)*, 330, L67.
Boland, W., and de Jong, T. 1981, *Astr. Ap.*, 98, 149.
Campbell, B. 1984*a*, *Ap. J. (Letters)*, 282, L27.
———. 1984*b*, Ph.D. thesis, University of Arizona.
Campbell, B., and Thompson, R. I. 1984, *Ap. J.*, 279, 650.
Crampton, D., Georgelin, Y. M., and Georgelin, Y. P. 1978, *Astr. Ap.*, 66, 1.
Deguchi, S., and Watson, W. D. 1989, *Ap. J. (Letters)*, 340, L17.
Dickel, H. R., Rots, A. H., Goss, W. M., and Forster, J. R. 1982, *M.N.R.A.S.*, 198, 265.
Fischer, J., Sanders, D. B., Simon, M., and Solomon, P. M. 1985, *Ap. J.*, 293, 508.
Hackwell, J. A., Grasdalen, G. L., and Gehrz, R. D. 1982, *Ap. J.*, 252, 250.
Israel, F. P., Habing, M. J., and de Jong, T. 1973, *Astr. Ap.*, 27, 143.
Kameya, O., Hasegawa, T. I., Hirano, N., Takakubo, K., and Seki, M. 1989, *Ap. J.*, 339, 222.
Kliglesmith, D. A., and Hollis, J. M. 1987, *Ap. J. Suppl.*, 64, 127.
Larson, R. B. 1981, *M.N.R.A.S.*, 194, 809.
Leung, C. M., Kutner, M. L., and Mead, K. N. 1982, *Ap. J.*, 262, 583.
Martin-Pintado, J., Wilson, T. L., Johnston, K. J., and Henkel, C. 1985, *Ap. J.*, 299, 386.
Myers, P. C. 1983, *Ap. J.*, 270, 105.
Pratap, P., Batrla, W., and Snyder, L. E. 1989, *Ap. J.*, 341, 832.
Rots, A. H., Dickel, H. R., Forster, J. R., and Goss, W. M. 1981, *Ap. J. (Letters)*, 245, L15.
Scoville, N. Z., Sargent, A. I., Sanders, D. B., Claussen, M. J., Masson, C. R., Lo, K. Y., and Phillips, T. G. 1986, *Ap. J.*, 303, 416.
Vogel, S. N., Wright, M. C. H., Plambeck, R. L., and Welch, W. J. 1984, *Ap. J.*, 283, 655.
Wilson, T. L., and Walmsley, C. M. 1989, *Astr. Ap. Rev.*, 1, 141.

WOLFGANG BATRLA: Fachhochschule Coburg, Abteilung Muenchberg, Kulmbacher Str.76, D-8660 Muenchberg, Federal Republic of Germany

PREETHI PRATAP and LEWIS E. SNYDER: Astronomy Department, University of Illinois, 349 Astronomy Building, 1011 W. Springfield Avenue, Urbana, IL 61801

REFERENCES

Baan, W. A., Gusten, R., and Haschick, A. D. 1986, Ap. J., 305, 830.

Batrla, W., Matthews, H. E., Menten, K. M., and Walmsley, C. M. 1987, Nature, 326, 49.

Batrla, W., and Menten, K. M. 1988, preprint.

Batrla, W., Pratap, P., and Snyder, L. E. 1988, Ap. J. (Letters), 330, L67.

Benson, J. M., and Johnston, K. L. 1984, Ap. J., 277, 181.

Boland, W., and de Jong, T. 1981, Astr. Ap., 98, 149.

Botschwina, P. 1989 in Ion and Cluster Ion Spectroscopy and Structure, ed. J. P. Maier (Elsevier), p. 59.

Broten, N. W., Macleod, J. M., Oka, T., Avery, L. W., Brooks, J. W., McGee, R. X., Newton, L. M. 1976, Ap. J. (Letters), 209, L143.

Burke, B. F., Papa, D. C., Papadopoulos, G. D., Schwartz, P. R., Knowles, S. H., Sullivan, W. T., Meeks, M. L., and Moran, J. M. 1970, Ap. J. (Letters), 160, L63.

Campbell, B. 1984a, Ap. J. (Letters), 282, L27.

Campbell, B. 1984b, Ph.D. thesis, University of Arizona.

Campbell, B., and Thompson, R. I. 1984, Ap. J., 279, 650.

Campbell, B. 1985 in Masers, Molecules and Mass Outflows in Star Forming Regions, ed. A. D. Haschick (Haystack Observatory), p101.

Campbell, B., and Persson, S. E. 1988, Astron. J., 95, 1185.

Carlstrom, J. E., and Vogel, S. N. 1989, Ap. J., 337, 408.

Chini, R., Krugel, E., and Kreysa, E. 1986, Astr. Ap., 167, 315.

Churchwell, E., and Bieging, J. H. 1982, Ap. J., 258, 515.

Crampton, D., Georgelin, Y. M., and Georgelin, Y. P. 1978, Astr. Ap., 66, 1.

de Jong, T. 1973, Astr. Ap., 26, 297.

de Jong, T., Chu, S. I., and Dalgarno, A. 1975, Ap. J., 199, 69.

Dickel, H. R., Dickel, J. R., and Wilson, T. L. 1981, Ap. J. (Letters), 250, L43.

Dickel, H. R., Rots, A. H., Goss, W. M., and Forster, J. R. 1982, M.N.R.A.S., 198, 265.

Downes, D., and Wilson, T. L. 1974, Ap. J. (Letters), 191, L77.

Elitzur, M. 1985 in Masers, Molecules and Mass Outflows in Star Forming Regions, ed. A. D. Haschick (Haystack Observatory), p. 299.

Elitzur, M. 1979, Astr. Ap., 73, 322.

Elitzur, M., and de Jong, T. 1978, Astr. Ap., 67, 323.

Elitzur, M., Goldreich, P., Scoville, N. 1976, Ap. J., 205, 384.

Elsasser, H., Birkle, K., Eiroa, C., and Lenzen, R. 1982, Astr. Ap., 108, 274.

Fischer, J., Sanders, D. B., Simon, M., and Solomon, P. M. 1985, Ap. J., 293, 508.

Fischer, J. Righini-Cohen, G., Simon, M., Joyce, R. R., and Simon, T. 1980, Ap. J. (Letters), 240, L95.

Forster, J. R., Goss, W.M., Gardner, F. F., and Stewart, R. T. 1985, M.N.R.A.S., 216, 35P.

Forster, J. R., Graham, D., Goss, W. M., Booth, R. S. 1982,

M.N.R.A.S., 201, 7P.

Forster, J. R., Welch, W. J., Wright, M. C. H., and Baudry, A. 1978, Ap. J., 221, 137.

Forster, J. R., Welch, W. J., and Wright, M. C. H. 1977, Ap. J. (Letters), 215, L121.

Gardner, F. F., Whiteoak, J. B., Forster, J. R., and Pankonin, V. 1986, M.N.R.A.S., 218, 385.

Gardner, F. F., and Martin-Pintado, J. 1983, Astr. Ap., 121, 265.

Garrison, B. J., Lester, W. A., Miller, W. H., and Green, S. 1975, Ap. J. (Letters), 200, L175.

Gaume et al. 1990, in preparation.

Genzel, R., Downes, D., Moran, J. M., Johnston, K. J., Spencer, J. H., Matveyenko, L. I., Kogan, L. R., Kostenko, V. I., Ronnang, B., Haschick, A. D., Reid, M. J., Walker, R. C., Giuffrida, T. S., Burke, B. F., and Moiseev, I. G. 1979, Astr. Ap., 78, 239.

Genzel, R., and Downes, D. 1976, Nature, 262, 564.

Goldreich, P., and Kwan, J. 1974, Ap. J., 191, 93.

Gottlieb, C. A., Ball, J. A., Gottlieb, E. W., and Dickinson, D. F. 1979, Ap. J., 227, 422.

Gottlieb, C. A., Gottlieb, E. W., Litvak, M. M., Ball, J. A., and Penfield, H. 1978, Ap. J., 219, 77.

Green, S. 1974, Physica, 76, 609.

Green, S. 1975, Ap. J., 201, 366.

Green, S., and Chapman, S. 1978, Ap. J. Suppl., 37, 169.

Green, S., and Monchick, L. 1975, J. Chem. Phys., 63, 4198.

Green, S., and Thaddeus, P. 1974, Ap. J., 201,

Green, S., and Thaddeus, P. 1976, Ap. J., 205,

Guilloteau, S, Wilson, T. L., Martin, R. N., Batrla, W., and Pauls, T. A. 1983, Astr. Ap., 124, 322.

Guilloteau, S., and Lucas, R. 1981, Astr. Ap., 101, L19.

Habing, H. J., Goss, W. M., Matthews, H. E., and Winnberg, A. 1974, Astr. Ap., 35, 1.

Hackwell, J. A., Grasdalen, G. L., and Gehrz, R. D. 1982, Ap. J., 252, 250.

Harris, S., and Scott, P. F. 1976, M.N.R.A.S., 175, 371.

Harvey, P. M., Bechis, K. P., Wilson, W. J., and Ball, J. A. 1974, Ap. J. Suppl., 27, 331.

Haschick, A. D., Reid, M. J., Burke, B. F., Moran, J. M., and Miller, G. 1981, Ap. J., 244, 76.

Henkel, C., Wilson, T. L., and Johnston, K. J. 1984, Ap. J. (Letters), 282, L93.

Ho, P. T. P., Martin, R. N., and Barrett, A. H. 1981, Ap. J., 246, 761.

Hollis, J. M., Snyder, L. E., Buhl, D., and Giguere, P. T. 1975, Ap. J., 200, 584.

Israel, F. P. 1977, Astr. Ap., 59, 27.

Israel, F. P., Habing, M. J., and de Jong, T. 1973, Astr. Ap., 27, 143.

Johnston, I. D. 1967, Ap. J., 150, 33.

Johnston, K. J., Knowles, S. H., Sullivan, W. T., Moran, J. M., Burke, B. F., Lo, K. Y., Papa, D. C., Papadopoulos, G. D., Schwartz, P. R., Knight, C. A., Shapiro, I. I., and Welch, W. J. 1971, Ap. J. (Letters), 166, L21.

Kameya, O., Hasegawa, T. I., Hirano, N., Takakubo, K., and Seki, M. 1989, Ap. J., 339, 222.

Larson, R. B. 1981, M.N.R.A.S., 194, 809.

Leung, C. M., Kutner, M. L., and Mead, K. N. 1982, Ap. J., 262, 583.

Lo, K. Y., Walker, R. C., Burke, B. F., Moran, J. M., Johnston, K. J., and Ewing, M. S. 1975, Ap. J., 202, 650.

Lynds, B. T., and O'Neil, E. J. 1986, Ap. J., 306, 532.

Madden, S. C., Irvine, W. M., Matthews, H. E., Brown, R. D., and Godfrey, P. D. 1986, Ap. J., 300, L79.

Mader, G. L., Johnston, K. J., and Moran, J. M. 1978, Ap. J., 224, 115.

Martin, A. H. M. 1973, M.N.R.A.S., 163, 141.

Martin-Pintado, J., Wilson, T. L., Gardner, F. F., and Henkel, C. 1985, Astr. Ap., 142, 131.

Matsakis, D. N., Cheung, A. C., Wright, M. C. H., Askne, J. I. H., Townes, C. H., and Welch, W. J. 1980, Ap. J., 236, 481.

Mauersberger, R., Wilson, T. L., and Henkel, C. 1986, Astr. Ap., 160, L13.

Menten, K. M., Reid, M. J., Moran, J. M., Wilson, T. L., Johnston, K. J., and Batrla, W. 1988, Ap. J. (Letters), 333, L83.

Menten, K. M., Walmsley, C. M., Henkel, C., and Wilson, T. L. 1986,

Astr. Ap., 157, 318.

Mezger, P. G., and Henderson, A. P. 1967, Ap. J., 147, 471.

Monteiro, T. S. 1984, M. N. R. A. S., 211, 257.

Monteiro, T. S. 1985, M. N. R. A. S., 211,

Moran, J. M., Reid, M. J., Lada, C. J., Yen, J. L., Johnston, K. J., and Spencer, J. H. 1978, Ap. J. (Letters), 224, L67.

Morimoto, M., Ohishi, M., and Kanzawa, T. 1985, Ap. J. (Letters), 288, L11.

Morris, M., Palmer, P., Turner, B. E., and Zuckerman, B. 1976, Ap. J., 205, 82.

Morris, M., Palmer, P., Turner, B. E., and Zuckerman, B. 1974, Ap. J., 191, 349.

Myers, P. C. 1983, Ap. J., 270, 105.

Norris, R. P., and Booth, R. S. 1981, M.N.R.A.S., 195, 213.

Norris, R. P., Booth, R. S., Diamond, P. J., and Porter, M. D., 1982, M.N.R.A.S., 201, 191.

Olnon, F. M. 1975, Astr. Ap., 39, 217.

Oster, L. 1961, Rev. Mod. Phys., 33, 525.

Palmer, P., Zuckerman, B., Buhl, D., and Snyder, L. E. 1969, Ap. J. (Letters), 156, L147.

Palmer, P., Gardner, F. F., and Whiteoak, J. B. 1984, M.N.R.A.S., 211, 41P.

Pratap, P., Batrla, W., and Snyder, L. E. 1989, Ap. J., 341, 832.

Pratap, P., Batrla, W., and Snyder, L. E. 1990, Ap. J., 351, 530.

Reid, M. J., and Moran, J. M. 1981, Ann. Rev. Astr. Ap., 19, 231.

Reid, M. J., Haschick, A. D., Burke, B. F., Moran, J. M., Johnston, K. J., and Swenson, G. W. 1980, Ap. J., 239, 89.

Rots, A. H., Dickel, H. R., Forster, J. R., and Goss, W. M. 1981, Ap. J. (Letters), 245, L15.

Rydbeck, O. E., H., Kolberg, E., Hjalmarson, A., Sume, A., Ellder, J., and Irvine, W. M. 1976, Ap. J. Suppl., 31, 333.

Schwartz, P. R., Cheung, A. C., Bologna, J. M., Chui, M. F., Waak, J. A., and Matsakis, D. 1977, Ap. J., 218, 671.

Scoville, N. Z., Sargent, A. I., Sanders, D. B., Claussen, M. J., Masson, C. R. Lo, K. Y., and Phillips, T. G. 1986, Ap. J., 303, 416.

Snell, R. L., and Wootten, A. 1979, Ap. J., 228, 748.

Snyder, L. E., Hollis, J. M., Lovas, F. J., and Ulich, B. L. 1976, Ap. J., 209, 67.

Snyder, L. E., and Buhl, D. 1974, Ap. J. (Letters), 189, L31.

Spitzer, L. 1978, Physical Processes in the Interstellar Medium (Wiley, New York).

Tarter, J. C., and Welch, W. J. 1979, Bull. Am. Astron. Soc., 11, 689.

Thaddeus, P., Kutner, M. L., Penzias, A. A., Wilson, R. W., and Jefferts, K. B. 1972, Ap. J. (Letters), 176, L73.

Thronson, A. H., and Harper, D. A. 1979, Ap. J., 230, 133.

Townes, C. H., and Cheung, A. C. 1969, Ap. J. (Letters), 157, L103.

Townes, C. H., and Schawlow, A. L. 1956, Microwave Spectroscopy (McGraw-Hill, New York).

Tucker, K. D., Kutner, M. L., and Thaddeus, P. 1974, Ap. J. (Letters),

193, L115.

Turner, B. E., and Thaddeus, P. 1977, Ap. J., 211, 755.

Turner, B. E., and Zuckerman, B. 1974, Ap. J. (Letters), 191, L77.

Urry, L., Thornton, D. D., and Hudson, J, 1985, P.A.S.P., 97, 745.

Vogel, S. N., Wright, M. C. H., Plambeck, R. L., and Welch, W. J. 1984, Ap. J., 283, 655.

Walmsley, C. M.,Churchwell, E., Nash, A., and Fitzpatrick, E. 1982, Ap. J. (Letters), 258, L75.

Werner, M. W., Becklin, E. E., Gatley, I., Matthews, K., Neugebauer, G., and Wynn-Williams, C. G. 1979, M.N.R.A.S., 188, 463.

Whiteoak, J. B., and Gardner, F. F. 1983, M.N.R.A.S., 205, 27P.

Wilson, T. L., and Walmsley, C. M. 1989, Astr. Ap. Rev., 1,

Wilson, T. L., Walmsley, C. M., Menten, K. M., and Hermsen, W. 1985, Astr. Ap., 147, L19.

Wilson, T. L., Walmsley, C. M., Snyder, L. E., and Jewell, P. R. 1984, Astr. Ap., 134, L7.

Wilson, T. L., Batrla, W., and Pauls, T. A. 1982, Astr. Ap., 110, L20.

Willner, S. P. 1976, Ap. J., 206, 728.

Wink J. E., and Altenhoff W. J. 1975, Astr. Ap., 38, 109.

Woody, D. P., Scott, S. L., Scoville, N. Z., Mundy, L. G., Sargent, A. I., Padin, S., Tinney, C. G., and Wilson, C. D. 1989, Ap. J. (Letters), 337, L4.

Wynn-Williams, C. G. Becklin, E. E., and Neugebauer, G. 1974, Ap. J., 187, 473.

VITA

Preethi Pratap

Birth Place and date:

Born January 13, 1961 in Trichur, India.

Education:

B.Sc. (Physics), Gujarat University, 1981.

M.Sc. (Physics), Indian Institute of Technology, Bombay, 1983.

M.S. (Astronomy), Univ. of Illinois, 1985.

Employment and Technical Experience:

Teaching Assistant, Astronomy Dept., Univ. of Illinois (1983-1985).

Research Assistant, Astronomy Dept., Univ. of Illinois (1985-1990).

Scholastic Honors and Scholarships:

Govt. of India National Merit Scholarship (1981-1983).

Invited Lectures:

"Molecular Observations of NGC 7538 IRS 1" at the Max Planck Institut Fur Radioastronomie, Bonn, W.Germany, May 1988.

"Molecular Observations of NGC 7538 IRS 1" at the Radio Astronomy Group, Tata Institute of Fundamental Research, Bangalore, India, June 1988.

"Maser Excitation in Astronomical Sources" at the Physics Dept., Cochin University of Science and Technology, Cochin, India, June 1988.

Professional Organizations:

American Astronomical Society.

Publications:

(1) "Spectrophotometry of the compact planetary nebulae NGC 6879 and NGC 6881" J. B. Kaler, P. Pratap, and K. B. Kwitter 1987, P.A.S.P., 99, 952.

(2) "Interferometric Observations of the 1-0 transition of HCO^+ toward NGC 7538 IRS 1" W. Batrla, P. Pratap, and L. E. Snyder 1988, Ap. J. (Letters), 330, L67.

(3) "Masers and Molecules near the Unusual Formaldehyde Maser NGC 7538 IRS 1" P. Pratap, W. Batrla, and L. E. Snyder 1989, Ap. J., 341, 832.

(4) "High Resolution Observations of NGC 7538 IRS 1" P. Pratap, W. Batrla, and L. E. Snyder 1989, to appear in the Proceedings of the A.S.P symposium on "The Evolution of the Interstellar Medium".

(5) "High Resolution Molecular Observations of NGC 7538 IRS 1" P. Pratap, W. Batrla, and L. E. Snyder 1990, Ap. J., 351, 530.